Escola de Camins
Escola Tècnica Superior d'Enginyeria de Camins, Canals i Ports
UPC BARCELONATECH

TREBALL FINAL DE MÀSTER

Automation of processes for the determination of material law parameters in the automotive industry

Treball realitzat per:
Lluís Martorell Pons

Dirigit per:
Lucia Gratiela Barbu
Eduardo Martin Santos

Màster en:
Enginyeria Civil

Barcelona, Septembre/2019

Departament d'Enginyeria Civil i Ambiental

MASTER THESIS

AUTOMATION OF PROCESSES FOR THE DETERMINATION OF MATERIAL LAW PARAMETERS IN THE AUTOMOTIVE INDUSTRY

Author of the work:

Martorell Pons, Lluís

Supervised by:

Associate prof. **Barbu, Lucia Gratiela**

External tutor **Martin Santos, Eduardo**

Master in Civil Engineering

Escola Tècnica Superior d'Enginyers de Camins, Canals i Ports de Barcelona

Universitat Politècnica de Catalunya (UPC)

September 2019

Abstract

Manufacturing techniques and involved materials in design of automotive vehicles is a continuous evolving process. The growing trend in the industry is the use of Advanced High Strength Steels in order to decrease the vehicle weight while still maintaining or even improving the crashworthiness performance. This leads to the consideration of some aspects in simulation that were not required in the past for the design of steels.

In classical automotive design, fracture was difficult to be observed in structural materials, since the capability of energy dissipation due to plastic deformation in the materials was enough to accomplish the required performance levels in component design. The inclusion of new materials (i.e. AHSS) and regulations (i.e. Small overlap), caused the consideration of material fracture to become relevant in this framework. This makes of vital importance that the damage and fracture behaviour of the AHSS is accurately introduced in the simulations related.

The main target of this work is to create a model oriented to productive projects in order to reduce the cost and the time consumption of performing the generation of the material card for steel related simulations, considering damage and strain-rate related effects. This new methodology is based in previous studies done by IDIADA. The methodology is applied in component-related simulations as a 3PBT, dynamic bending and axial crushing, obtaining levels of correlation enough accurate for component design.

Acknowledgements

The end of a journey started 9 years ago, by a teenager who had just landed in Barcelona, has come with the presentation of this work. It has been a long way, where much effort has been necessary and I have become a better person than yesterday. There are many happy memories of living through it with many new friends.

I would like to thank the people from the Body Development department of Applus+ IDIADA for the opportunity they gave me. I specially would like to thank Eduardo Martin for the efforts done in helping me and also thank all the Material Engineering team for being so awesome and crazy.

And above all, I would like to thank Ane for her invaluable support and all her love and patience that she has shown since we met. Now a new journey begins and I hope we go through it together.

Contents

List of Figures

List of Tables

1. Introduction and objectives

In this work, the industrial process for the generation of material cards for steel related simulations is mean to be improved. For this, the inclusion of automation and optimization methods is proposed. The target of the project is to create a model oriented to productive projects, in order to reduce the cost and the time consumption that represents nowadays the tasks of performing manually the material parameter characterisation. Methodologies in this work will be developed for their application in the commercial solver LS-DYNA, and the development will be focused in the Advanced High Strength Steels framework.

This work has been developed during a one-year internship at Applus+ IDIADA. Applus+ IDIADA is an engineering company providing design, testing, engineering and homologation services to the automotive industry. The work was done in the CAE department, more precisely in the Materials Engineering team. This project comes from an IDEADA, which is a program of internal projects at IDIADA, promoting the innovation.

The purpose of this first chapter is to briefly review the evolution in the application of numerical methods used for crash simulations in the automotive industry, highlighting its growing importance and its undeniable utility nowadays. Next, the motivations on which this thesis is based, as well as the main objectives to be achieved are exposed. Finally, a summary of the subsequent chapters into which this work has been divided is presented.

1.1. Background

Design and manufacturing of automotive vehicles has been evolving since the beginning of its existence. Manufacturing techniques and involved materials have been in a continuous process of change and improvement during the decades. In consequence, development of new vehicles and components has grown in complexity, in order to accomplish with the environmental regulations and to enhance the safety performance.

Nowadays, due to the progress accomplished in the field of numerical methods and the computational evolution in terms of power and efficiency, the component design and development process in the automotive industry has changed to numerical simulation design. In fact, there are some regulations for homologation that can be surpassed only with simulation without the need of experimental testing or correlation, more than simple component tests in critical zones.

Some decades ago, large series of prototypes were built at each of the development phases of a vehicle. These prototypes were built barely considering numerical methods, which at that moment had a secondary role in the industry. Therefore, design and development of a new vehicle were extremely costly. Nowadays all car manufacturer companies have integrated numerical software for the development of their products. In this framework, crash-related simulations are solved for structural and occupant protection development. For this, the Finite Element Method (FEM) is

used. Development requires both testing and simulation at different levels: Coupon, Component, Subsystem and Full-vehicle. In order to achieve level of correlation enough for development, simulations need to be accurate and reliable, representing the real behaviour of the materials involved.

Due to the global trend to reduce CO_2 emissions, during the last decade the focus has been pointed at decreasing the weight of the vehicles. Steel is one of the most relevant materials in the automotive framework, representing roughly 60% of the weight in an average vehicle. Therefore, a demanding issue is to decrease the vehicle weight while still maintaining or even improving the crashworthiness performance.

Nowadays, one of the most current trends in the market for weight reduction is the application of Advanced High Strength Steels (AHSS from now on) which have higher yield strength levels and lower density than the conventional steels [7].

Regulations are also evolving every year and the trend is to become more and more restrictive aiming to ensure more safety for the passengers. In classical design, fracture was difficult to be observed in structural materials, and the development was able to be done only accounting with an advanced model of plasticity. The inclusion of new materials (i.e. AHSS) and regulations (i.e. Small overlap [51]), caused the consideration of material fracture to become relevant in component design. This makes of vital importance that the damage and fracture behaviour of the AHSS is accurately measured and reproduced in simulations.

1.2. Motivation

One of the main challenges nowadays in the automotive industry is the accurate prediction of the failure in the structural parts of the vehicle under service conditions. The introduction of the new materials (high-strength steels, aluminium, composites) is aimed at lightening the weight of the structure, seeking to reduce fuel consumption. This is especially critical with the increasing implementation of electric motors; whose power train represents a remarkable increase in the total weight of the vehicle.

In conventional design, the material characterization including damage failure of steel components is usually done at the last iterations of the design and development phase of a vehicle. During the previous iterations, it is also necessary to have a material card to introduce at the numerical solver. However, due the expensive cost of the experimental campaign to capture damage, they are not done until the materials of the vehicle are selected and locked in the design, so it has only to be done once for each material. This point out an important issue of the design phase, the initial iterations are done, normally, simulating the materials without a complete experimental campaign performed. Therefore, companies have to choose between performing expensive testing campaigns of materials that may not be used at the end or to start the design loops with a non-calibrated material or without damage and failure prediction. There is a trade-off situation between costs and accuracy of the simulations.

In last years, IDIADA has been involved in projects regarding the characterization of AHSS steels for crash designs and has developed an innovative approach more cost efficient than the classical methodology used in the industry. IDIADA worked in collaboration with bachelor and master students, as well as different customers and technical centers in the development of new methodologies that could be used to represent more realistically the AHSS behaviour while

reducing experimental and engineering costs. That way, the whole design and development process becomes more efficient from the beginning, as failure prediction on AHSS can be considered.

After more than 2 years of development a new analytical approach was created [55], reducing the testing campaign needed for the classical steel characterisation approach and improving the correlation for the AHSS. Even through the new methodology has a good level of correlation, the optimization of a large number of parameters is needed. Currently it is done manually, implying high time and monetary costs and lower accuracy of the final card obtained.

In the current methodology status, a large amount of engineering hours is necessary to create each material card. However, all the parameters involved in the simulation are well known, so the inclusion of parametric optimization techniques is viable and will reduce the amount of engineering hours needed for this task. In addition, the full automation of the methodology will allow the engineer to work in parallel in other tasks, while the optimization process is running, saving time and cost.

1.3. Objectives

The goal of the thesis is the improvement of the process for the characterization of AHSS by analytical approach, developed by IDIADA, in order to make it more efficient at productive level (industrialization of the method). For this goal, the following targets should be considered:

- The automation of the whole process.
- The implementation of parametric optimization techniques to the current methodology status.
- Increase the correlation of the methodology developed by IDIADA.
- Validation of the model with new experimental data.
- The generated material cards should be usable by any conventional CAE engineer related to design, not requiring specialization on the materials mechanics framework.

The main technical objective is to reduce the engineering hours required for the generation of material cards in AHSS materials for crash simulation in the automotive framework. In this case, this product could be offered in less time and greater efficiency, since the majority of time is spent in computer hours, and the resulting material card will be of higher quality than the current one obtained by manual processes.

1.4. Outline of the thesis

In this section a brief description of the document is presented. The document begins with an introduction to steels and a summary of AHSS as well as a brief explanation of the testing campaign used to determine the steel properties.

The following chapter contains a general and brief explanation of the Finite Element Method (FEM) and the key aspects used in the automotive industry for full vehicle simulations.

In chapter 4, the constitutive models predicting the steel behaviour are described. Also, the different approaches used in the automotive industry for the material modelling is presented, including the one developed at IDIADA.

Next chapter presents the LSDYNA commercial software and its capabilities for material characterization. The models used at this project are described and explained how to use them.

Chapter 6 introduces the automation and optimization processes done in this work and explains the improvements done to the previous methodology.

The following chapter presents the results obtained from the methodology developed in this work and compares it with results from the previous working approach.

Chapter 8 shows different real cases where the methodology developed in this thesis has been applied in projects with success.

Finally, in chapter 9 are presented the conclusions of this work, and future lines of work related to this topic.

1.5. Confidentiality

This thesis was made at the IDIADA installations and under a confidentiality contract. For the protection of the data from clients and IDIADA itself during this thesis some values, material names or correlation factor have been hidden. Some aspects of the methodology itself are not explained in detail intentionally in order to protect IDIADA's industrial knowledge. No data has been hidden that can prevent the understanding of this work or following it.

2. Literature review on steels

The objective of this chapter is to provide the reader with a brief introduction to the steels used currently in the automotive industry including the advanced high strength steels (AHSS). Then, the common experimental tests done during a steel testing campaign are explained. The numerical simulation of the steel behaviour will be explained in following chapters.

2.1. Basic concepts on steels

Nowadays steel, is one of the most largely used materials in a wide range of product making applications, from basic tools to cars and planes, to buildings. This is due to its functionality, strength, adaptability, recyclability and machine-ability.

In cars, at early 1980s the steel weight percentage was around 53-55%. Today it is up to 60% for North American light-vehicles [61]. Therefore, some performances as occupant protection, comfort driving, weldability, etc. greatly rely on the steel characteristics. Regarding emissions, steel has a recycling rate above 90%, which makes it a good election for CO_2 emission reduction in the overall manufacturing process of a vehicle.

In recent years, in order to improve crashworthiness performance and fuel economy, the automotive industry is increasing the application of Advanced High Strength Steel (AHSS) instead of the classically used conventional steels. In Figure 1 the evolution of an average vehicle material distribution by mass weight percentage is shown. The use of mild steels has been shifting to the use of medium and high strength steels in the last decades.

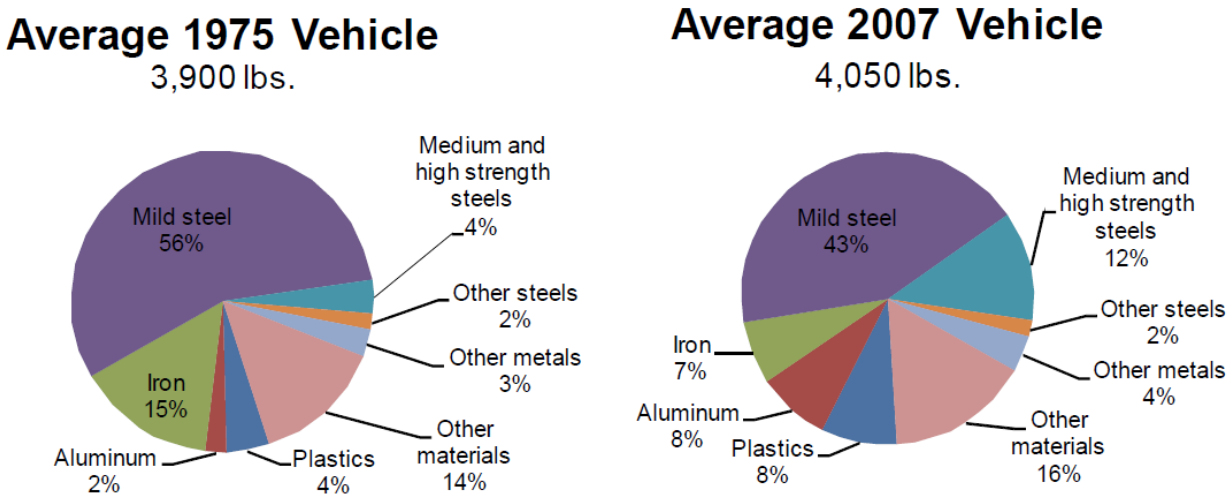

Figure 1 - Evolution of the materials present in an average vehicle by mass for years 1975 and 2007. Source: [64]

The high Ultimate strength, elastic recovery and other properties of steel can be explained from the atomic and microscopic level structure. Iron has the iron atoms equidistantly spaced with the same size voids between the atoms. However, carbon steel has the smaller carbon atoms diffused into the space between the iron atoms as it shown in Figure 2. It makes the carbon steel much stronger and harder than conventional iron. Other elements may also be added to the steel in order to obtain some desired properties. That may include strength, toughness, corrosion resistance, hardness, heat resistance, etc…

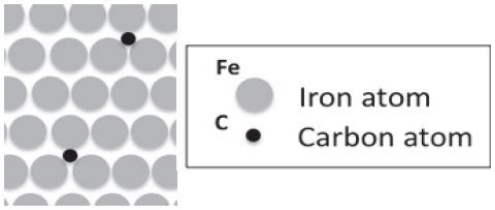

Figure 2 – Schematic representation of carbon atoms in the interstitial space of the iron lattice. Source: [20]

Although alloying can alter the steel properties and behaviour, steels with similar chemical composition can also show very diverse properties, depending on the manufacturing process received. The different processes done to a same basis steel can form different steels, due to variations in the microstructure.

The main processes affecting the final microstructure of the steel are the forming, cooling and post-forming. In Figure 3 and Figure 4 there are the iron-carbide phase binary diagram and the Time-temperature-transformation diagram ("TTT"), also differentiating the continuous cooling diagram ("CCT" curve), respectively. This two figures show the wide variety of microstructures that steels with a similar chemical constitution can show.

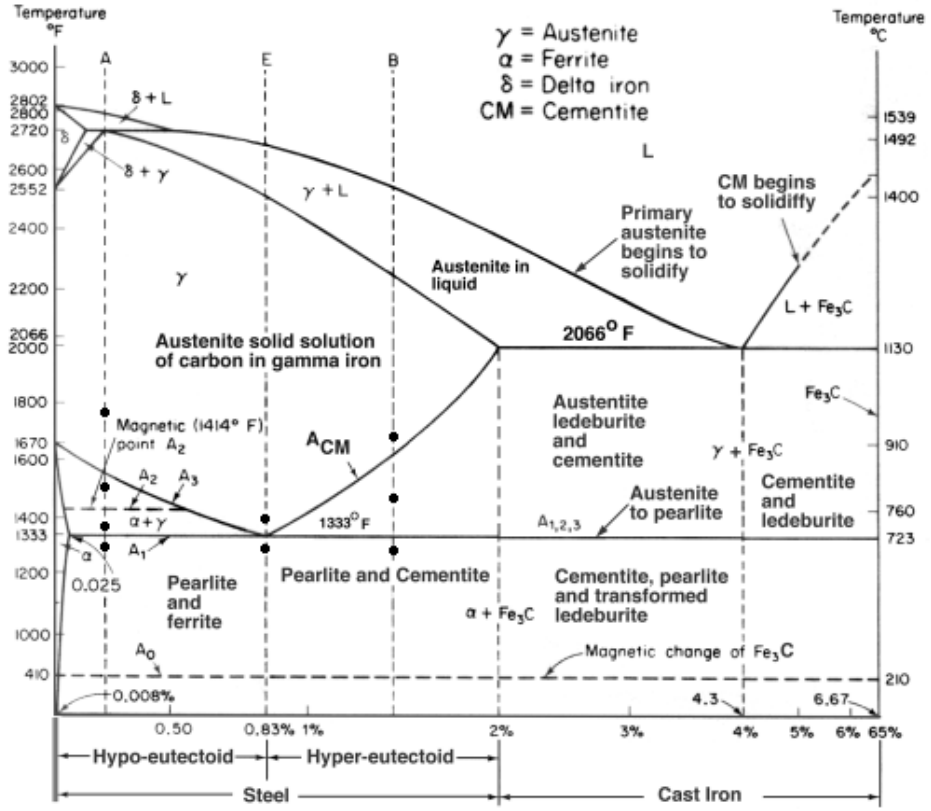

Figure 3 - Phase diagram of the Iron-carbide, with percent content shown at the x-axis. Source: [54]

The Fe-C equilibrium diagrams provide information about the transformation of austenite to other equilibrium structures but it does not provide information about other structures as the martensite which may be found in the microstructure of the steel. This information is found at the TTT and CCT diagrams. The TTT diagram represents the amount of transformation of austenite as function of time for a constant temperature. Operations involving heat treatment are not usually performed by isothermal processes. Therefore, the application of the TTT diagrams is limited. To overcome this TTT curve limitations the CCT diagrams were developed. CCT diagrams represent the transformation as a function of time for a continuous decreasing temperature.

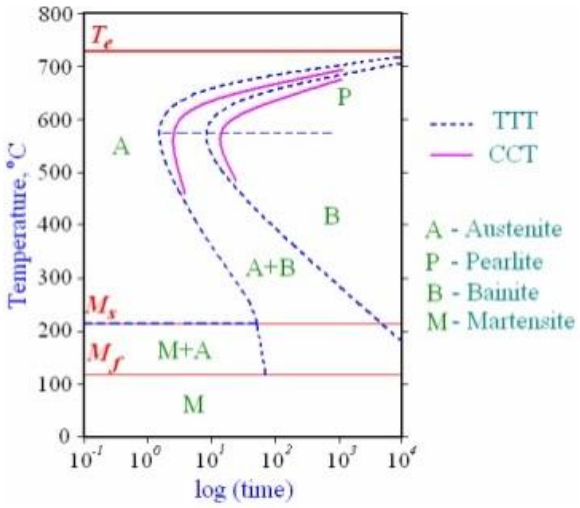

Figure 4 - TTT and CCT curve diagrams for eutectoid carbon steel. Source: [36]

Therefore, the final microstructure obtained can present different phases. This phase distribution, shape, and grain size are what contribute to the strength, ductility and other steel properties. The conventional mild steel has a rather simple ferritic microstructure; it has low carbon content and minimal alloying elements. Conventional mild steel is widely used and produced. It is often used as baseline for comparison of other materials.

As explained, steel can have a wide range of mechanical properties depending on various factors. Therefore, different steel grades can be defined, depending on its behaviour and characteristics. Figure 5 shows steel grades classification depending of the strength and ductility of the steel.

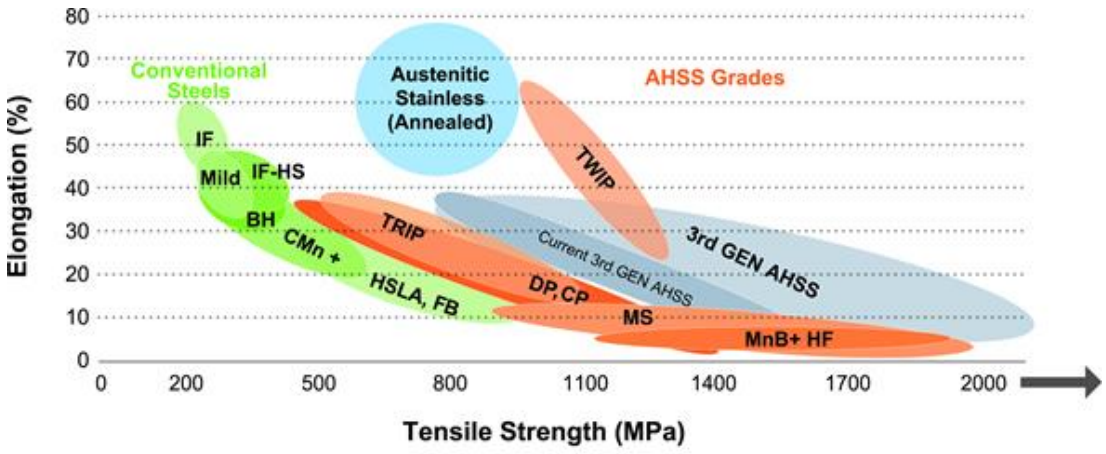

Figure 5 - Classification of steel grades in a strength ductility diagram. Source: [71]

Conventional low to high-strength steels include: Interstitial Free (IF) steel, mild steel, Bake Hardened (BH) steel and High-Strength Low-Alloy (HSLA) steel. These steels generally have less ductility for increasing strength and have yield strengths lower than 550 MPa.

Some of the steel properties are obtained through different methods employed by the metallurgists, such as strengthening or hardening mechanisms to meet the desired requirements for steel. Some of these strengthening mechanisms used are:

- Grain refinement: When increasing the effective area of grain boundaries by decreasing the size of grains (crystals), it makes the strength of the material to increase. When dislocations (crystallographic defect or irregularity within a crystal structure) travel through the material, they trend to pile up at grain boundaries, preventing more plastic deformation. The more grain boundaries there are in the material, more difficult is for the dislocations to move through it and therefore also for the metal to change shape. The result is a stiffer and harder metal.

- Dispersion strengthening or precipitation hardening: The presence of microstructural features (fine particles or lamellar sheets) may enhance the strength and hardness of the steel. When insoluble particles are introduced as a powder compaction (dispersion strengthening) or small particles of a new phase precipitate in a matrix as a solid state reaction (precipitation or age hardening), impediments to dislocation motion are formed and the material hardness increases.

- Solid solution strengthening: The introduction of atoms (the solute element) to the crystalline lattice of another metal (the solvent element), creating a solid solution, improves the strength of the solvent metal. The degree of strength improvement principally depends on the relative difference in size between the two elements involved. At more difference, greater distortion of the crystalline lattice and more impediment of the dislocations movement. Although this method increases the strength and hardenability it may simultaneously decrease the ductility of the material.

- Work hardening (or strain hardening): Intentionally inducing plastic deformation to the metal as a result of cold forming techniques (squeezing, bending, drawing and shearing). It makes the dislocations in steel to become more entangled, which prevents their relative movement. Due to work hardening, typically, the yield stress, ultimate tensile stress and hardness are increased but an adverse effect on ductility and toughness is introduced.

- Transformation strengthening: Having microstructures with significant amounts of hard phases (martensite or bainite) increase the strength of the steel. These transformations occur in operations where steel can cool from high-temperature austenite and transform to these harder phases. This is common in operations like: hot rolling, continuous annealing or hot-dip galvanizing. This mechanism is the main process to develop AHSS.

2.2. Advanced High Strength Steels (AHSS)

AHSS steels are more complex than conventional steels presented previously at Figure 5, particularly through their microstructures that generally are multiphase. The AHSS grade steels provide extremely high-strength (compared to mild steel). Other advantageous properties are high strain-hardening capacity, while maintaining high formability, required for component manufacturing.

The metallurgy and processability of AHSS depends mainly on the transformation mechanism applied for strengthening. AHHS are produced by controlling the cooling rate of the steel microstructure from austenite (or austenite plus ferrite phases). It can be performed on the run-out table of the hot mill (for hot-rolled products) or in the cooling section of the continuous annealing furnace (for continuously annealed or hot-dip coated products). Apart from the transformation strengthening mechanism, other strengthening mechanisms are also employed in order to achieve an expected range of strength, ductility, toughness, and fatigue properties.

AHSS steels include: Transformation-Induced Plasticity (TRIP) steel, Dual Phase (DP) steel, Complex Phase (CP) steel, Martensitic (MS) steel, Ferritic-Bainitic (FB) steel and Twinning-Induced Plasticity (TWIP) steel. Each of this AHSS steels has unique microstructural features, processing requirements, alloying additions, weldability, advantages and challenges associated with its use. In Figure 6, the evolution of the microstructure of some AHSS steels mentioned and the final microstructure is presented.

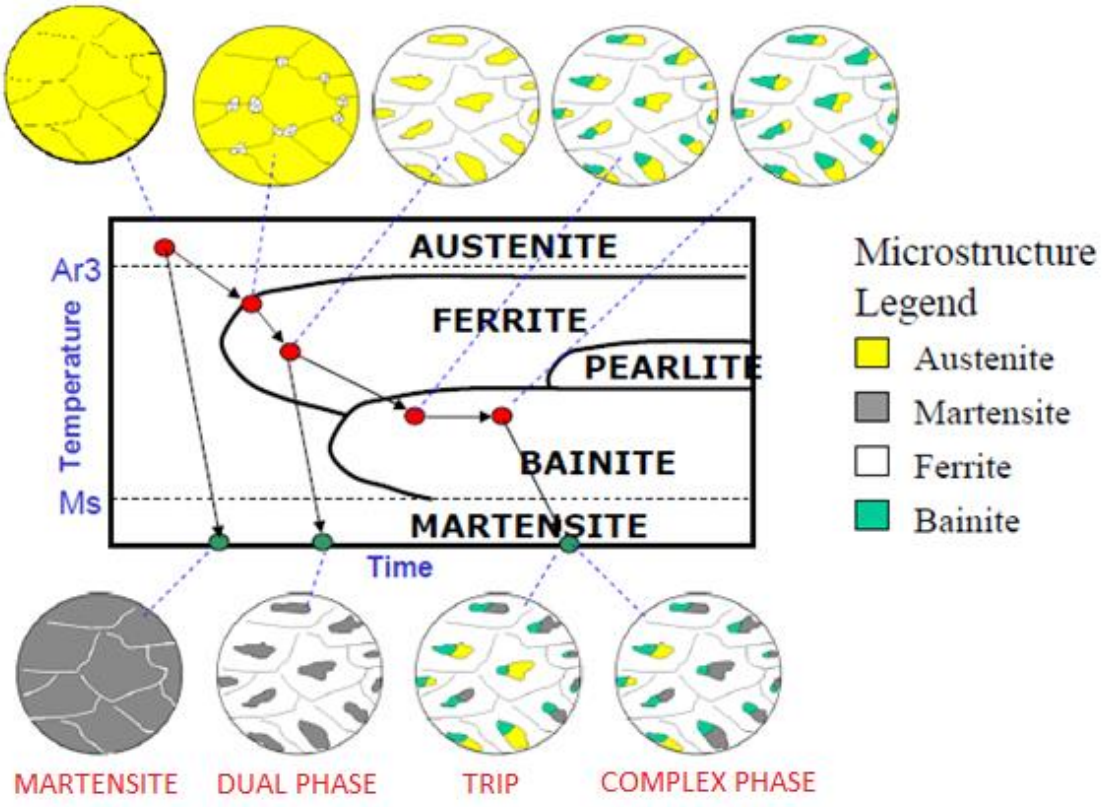

Figure 6 - Evolution of the microstructure of steel during controlled cooling. Source: [54]

Automakers have found different applications for the AHSS grades during the last years. Due to their high energy absorption, DP and TRIP steels are excellent in the crash-related zones of the car. For structural elements of the passenger compartment, extremely high-strength steels, such as

Martensitic steels, result in improved safety performance. One example could be found in the b-pillar of conventional vehicles, where extra high capabilities are required in the involved materials, since they will have an important role over the safety performance for occupant protection under lateral crash.

In response to automotive demands for additional AHSS capabilities, steel industry research continues to develop new types of steel [71]. These steels are designed to reduce density, improve strength, and/or increase elongation. For example, nano-steels are designed to avoid the low values of edge stretch (local elongation) experienced by DP and TRIP steels.

2.3. Experimental testing campaign

For automotive companies like IDIADA, with a strong CAE team that helps automakers to develop their new vehicles, it is of crucial importance to be able to simulate the full vehicle car behaviour. The quality of these simulations is closely related to the material definition in the numerical software. Therefore, the physical properties of the materials need to be translated to the software structure. Often, this numerical software, like ABAQUS, LS-DYNA, PAM-CRASH, NASTRAN, etc… defines the material properties using parameters. In those cases, these parameters need to be calibrated to represent the same behaviour as the real material used. In order to make that calibration, experimental data of the material is needed.

The complexity on the experimental campaign required to characterize a material depends on which behaviours are desired to be considered in simulation, and how precisely will they be reproduced. Therefore, different tests of different complexity will be needed for the measurement of the elasto-plastic regime, fracture onset, damage evolution, and strain rate effects.

For steels, that are one of the most used materials, the majority of tests are standardized and worldwide used. The uniaxial tensile test is always done and it allows the extraction of the data necessary to calibrate the elasto-plastic behaviour. When strain-rate effects are desired to be simulated, uniaxial tests are also performed, but the velocity of load application is adjusted to obtain a desired strain rate in the measurement range. For capturing the damage envelope and simulating it, the experimental data commonly comes from the Nakajima or the Marciniak tests. Finally, the fracture toughness of the material can be measured by means of Compact Tension or by tests over notched specimens and the application of the Essential Work of Fracture.

2.3.1. Uniaxial tension test

If a load is applied in a static regime, or it changes relatively slowly with time (quasi-static regime) and is applied uniformly over a cross section or surface of a member, the mechanical behaviour may be ascertained by a simple stress-strain test, as the uniaxial tensile test.

The tensile test is simple, relatively cheap, and totally standardized. It is probably the fundamental test in all the characterization campaign performed on a material for mechanical-related problems. The tensile test allows the creation of the tension-deformation curve of the material, from which the fundamental properties can be extracted for its simulation in the elasto-plastic regime. Additionally, it can allow the measurement of the Poisson ratio in the material.

In the uniaxial tensile test, the specimen is locked at one end and a predefined load is applied at the other end. The speed of displacement applied is maintained constant. During this process, the behaviour of the specimen in different states is measured. The elongation of the specimen is measured until failure.

The uniaxial tension test is standardized by the ISO 6892-1:2016 norm [32] with an extensometer of 50mm length placed. In Figure 7, a drawing of the INSTRON Series 5580 machine [30] that is used for the tensile axial test is shown.

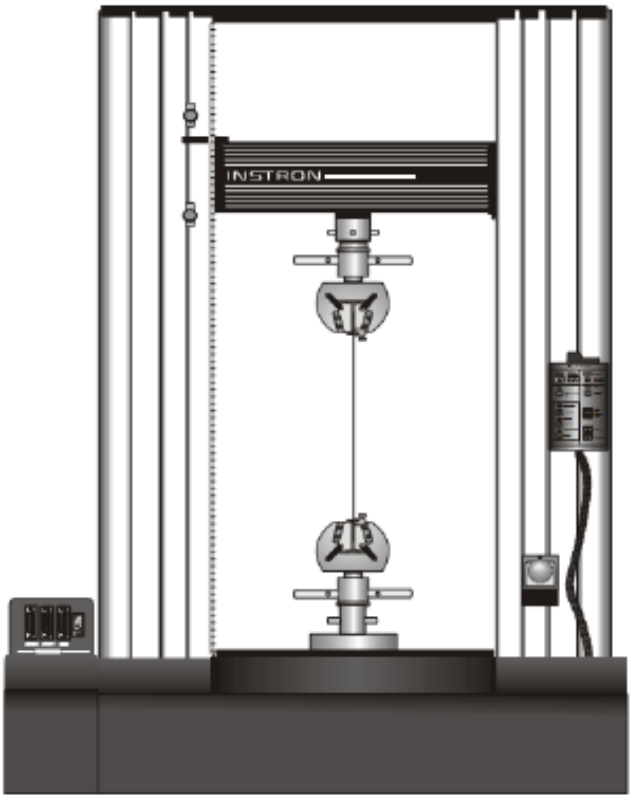

Figure 7 - INSTRON Series 5580. Source: [30]

The geometry of the uniaxial test specimen can be either flat “dog bone” shaped or circular, both with standardized dimensions. In Figure 8 and Table 1, the dimensions of the flat geometry specimen are defined, according to the American Society for Testing and Materials, as an example of a uniaxial tensile test specimen.

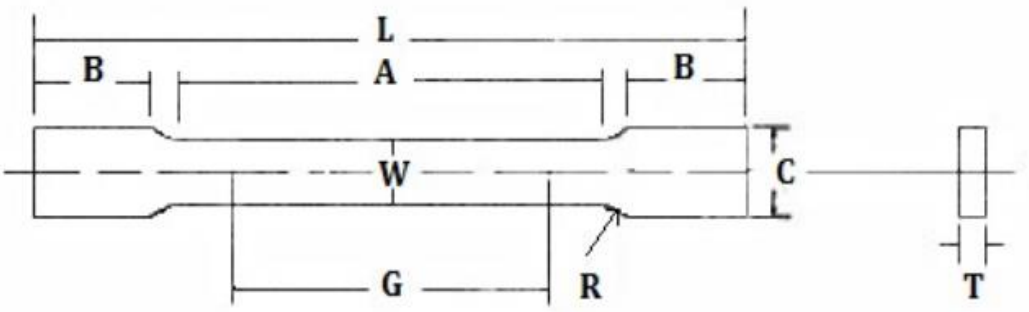

Figure 8 - Flat specimen parameterization for uniaxial test. Source: [4]

Table 1 - Dimensions for the standardized tensile test specimen according to American Society for Testing and Materials [4]

Parameter	Definition	Dimension (mm)
A	Length of reduced section	57.15
B	Length of grip section	50.8
C	Width of grip section	19.05
G	Gage length	50.80±0.13
L	Over-all length	203.2
R	Radius of fillet	12.7
T	Thickness	Thickness of the material
W	Width	12.7±0.25

For reliable results, the recommendation is to test more than one specimen (same geometry) for each material studied. The specimens may have defects or impurities that could lead to some uncertainties, so deviations between the responses of two identical geometrical specimens subjected to the same load can appear.

Figure 9 shows a schematic stress-strain relationship, obtained from a uniaxial tension test.

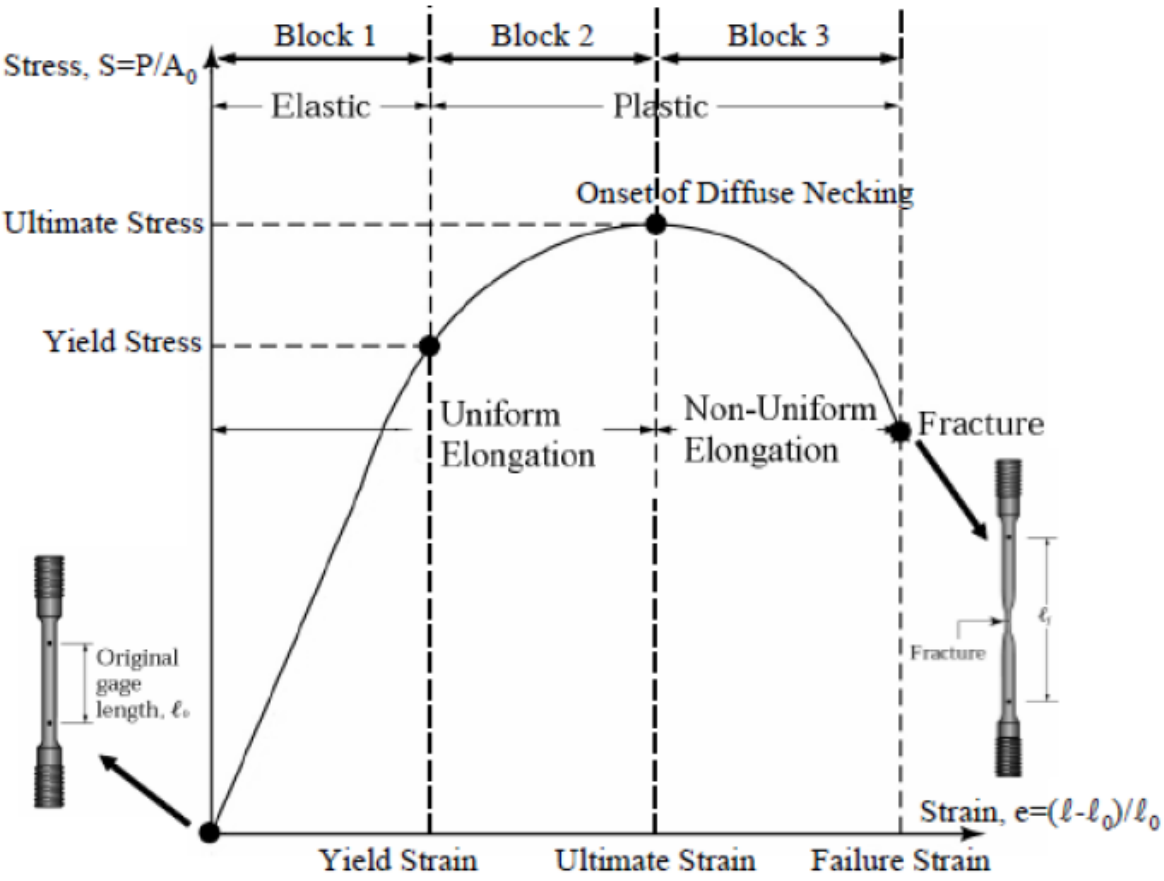

Figure 9 – Typical tension-deformation graph obtained from a uniaxial tensile test done to a steel material. The phases of the behaviour evolution of the test piece are described. Source: [17]

The elastic and the plastic regimes split the material behaviour in two physically different states. Firstly, the material behaves linearly until the yield stress and it is able to recover the

imposed deformations. If the material is further loaded, it experiences permanent deformations that remain after the load is released. When the material is loaded into the plastic region, there is a strain hardening and the yield stress increases with the accumulated plastic strain. Furthermore, at the ultimate strength, the hardening of the material can no longer compensate for the decrease in area. Then, the plastic regime leads to necking and distributed damage (micro-cracks among the metal that can reduce the stiffness of the material). Finally, the crack starts and grows in the material, until the total failure of the specimen. In the process of damage, the material is internally breaking and the damage is irreversible.

The output of such test is recorded generally as load or force versus elongation. Load and elongation are geometrical properties, which depend on the geometry of the specimen. To decouple the geometrical factors from the material's mechanic behaviour, load and elongation are transformed to engineering stress and engineering strain.

Engineering stress σ is defined by the relationship:

$$\sigma_{eng} = \frac{F}{A_0}. \tag{1}$$

Where F is the instantaneous load applied perpendicular to the specimen cross section and A_0 is the original cross-sectional area before any load is applied. Engineering stress has pressure units (Pa if the International System of Units (SI) is used).

Engineering strain ε_{eng} is defined by the next relationship:

$$\varepsilon_{\mathrm{eng}} = \frac{\mathrm{l_i} - l_0}{l_0} = \frac{\Delta l}{l_0}. \tag{2}$$

Where l_i is the instantaneous length and l_0 is the original length of the measurement before any load is applied. Engineering strain is unitless.

Sometimes it is more useful to use the true stress-true strain definitions instead the engineering ones. True stress ($\sigma_{true} \equiv \sigma_T$) is defined by the next relationship:

$$\sigma_{true} = \frac{F}{A_i}. \tag{3}$$

Where A_i is the instantaneous cross-sectional area over which the deformation is happening. True strain ($\varepsilon_{true} \equiv \varepsilon_T$) is defined by the next relationship:

$$\varepsilon_{true} = \ln\left(\frac{l_i}{l_0}\right). \tag{4}$$

In common FE developments, no volume change is considered during deformation, i.e.:

$$A_0 l_0 = A_i l_i, \tag{5}$$

then, engineering and true stress and strain are related, according to:

$$\sigma_T = \sigma_{eng}(1 + \varepsilon_{eng}), \tag{6}$$

$$\varepsilon_T = ln(1 + \varepsilon_{eng}). \tag{7}$$

In Figure 10, the engineering and true strain-stress curves are plot for a typical uniaxial tensile test in metals. Before necking, the specimen is assumed to deform uniformly. The softening that arises after the initiation of diffuse necking is caused by the engineering definition (elongation is no longer uniform beyond this point). A problem with the engineering measures is that they do not consider that dimensions in the specimen change during loading. Note that in the true definition, the stress necessary to sustain an increasing strain continues to rise, after the necking initiation.

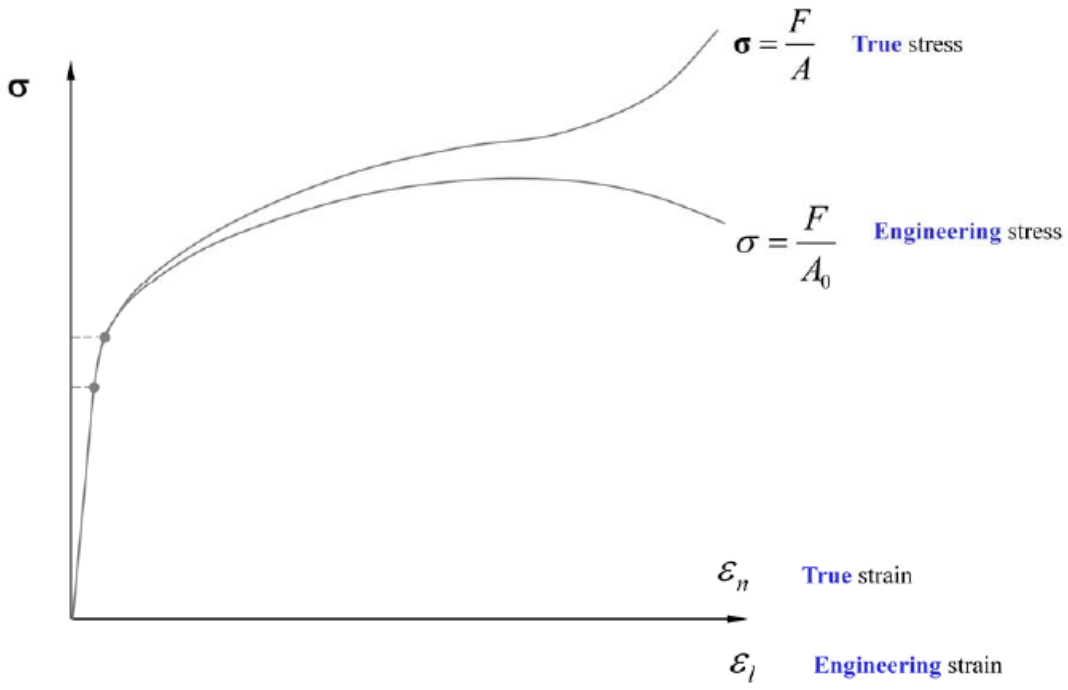

Figure 10 - Stress-strain engineering and true stress curves for a ductile material. Source: [19]

The most fundamental material properties can be obtained from the uniaxial test including most of the parameters of the elasto-plastic constitutive model (explained in detail at chapter 4). After the failure of the specimen, the ultimate strength is determined (the maximum load supported by the specimen divided by its initial section) along with the total elongation in (%) and the narrowing in the area of the break.

3. Overview of the finite element method

The objective of this chapter is to present some basic concepts regarding the finite element analysis. The Finite Element Method (FEM) is a powerful tool used for the analysis of complex problems in a wide range of disciplines, such as solid mechanics, civil engineering, hydrodynamics and geo-mechanics among others. It is useful in different physical processes described by differential equations to obtain an approximate solution of the problem. Its implementation in commercial software has improved the work of design engineers for the analysis of continuous systems with complex geometries subjected to any type of loading. The theory presented here is based on the book *An Introduction to the Finite Element Method* [56] and the subject *Numerical Modelling* from the master degree in Civil Engineering at the Universitat Politècnica de Catalunya (UPC) [40].

In general, the process of resolution of any engineering problem using mathematical tools and computers can be summarized by the flowchart shown in Figure 11.

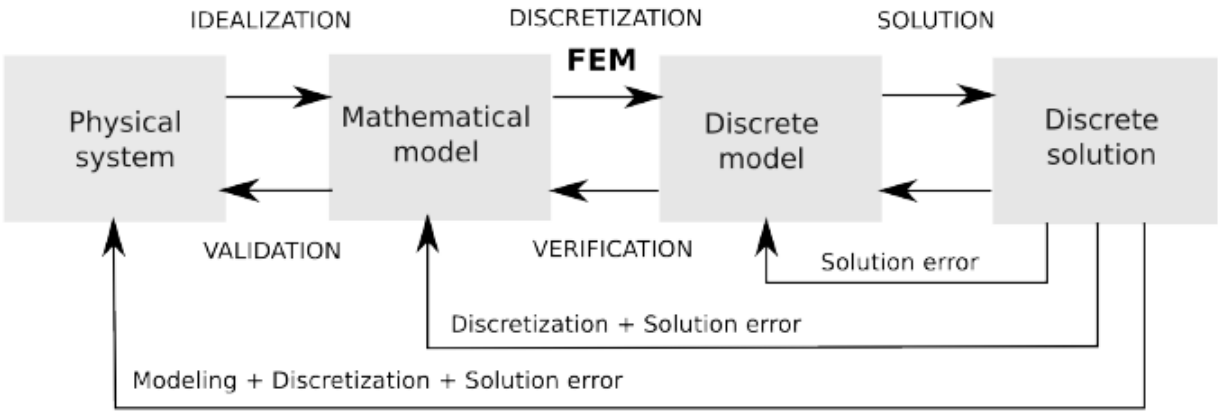

Figure 11 - Flowchart of real complex problems steps to be done to solve it. Source: [59]

Normally, the mathematical relationships that describe the physical behaviour of the system are ordinary and partial differential equations. These equations are generally impossible to be resolved by analytical methods. Therefore, the continuous space (infinite dimensional) needs to be transformed to a discrete space (finite dimensional) so an approximate solution can be calculated at the discrete space. This process is called discretization and the FEM carries it out. The initial domain is split in smaller domains, called finite elements. The points over the domain are called nodes and the unknowns are approximated at these nodes instead the initial whole domain. Therefore, the elements are described by its nodal points.

The FEM solves the problem by the succession of 3 steps:

1. Reformulation of the strong form of the governing equations of the physical system to an equivalent integral form called the weak form.

2. Discretization of the weak form. The approximate solution u^h is represented as a linear combination of polynomial basic functions N_i defined on the given mesh.

3. Solution of the finite element equation obtained in the amount of steps necessary to achieve the final solution of the problem.

The following sections explain in more detail how to obtain the weak form of an equation and the discretization procedure.

3.1. Weak form

The weak form is a method enclosed in the "direct variational methods", which refers to methods that make use of variational principles, such as the principle of virtual work and the principle of minimum potential energy in solids and structural mechanics, to determine approximate solutions of the problem [52]. Nowadays the use of the phrase "variational formulation" refers to the formulation in which the governing equations are translated into equivalent weighted-integral statements that are not necessarily equivalent to a variational principle.

A *weak form* is defined to be a weighted-integral statement of a differential equation in which the differentiation is transferred from the dependent variable to the weight function, such that all natural boundary conditions of the problem are also included in the integral statement.

Consider the problem of solving the differential equation given in the strong form at Equation 8 and graphically represented in Figure 12:

$$\begin{aligned} -\nabla \cdot (\mathbf{A}\nabla \mathrm{u}) &= \mathrm{f} \quad at\ \Omega \\ u &= u_d \quad at\ \Gamma_d \\ (\boldsymbol{A}\nabla u) \cdot \boldsymbol{n} &= g_n \quad at\ \Gamma_n \end{aligned} \tag{8}$$

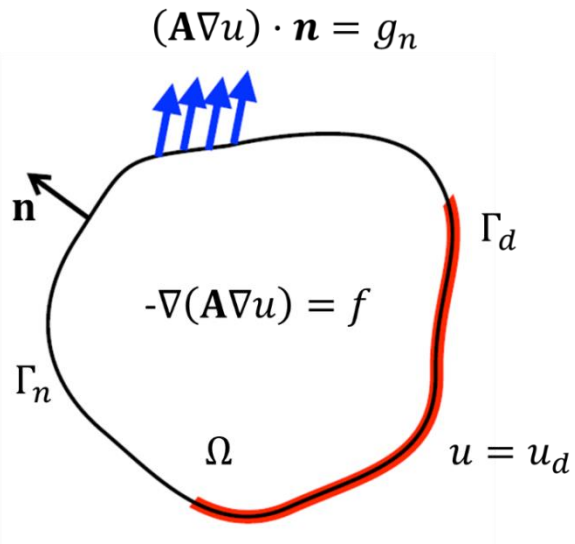

Figure 12 Graphical representation of a differential equation applied to a body . Source: Own

Where $\partial\Omega = \Gamma_d \cup \Gamma_n$ and u_d is the Dirichlet or essential boundary conditions and g_n is the Neumann or natural boundary condition. When the specified values are nonzero ($u_d \neq 0$ or $g_n \neq 0$), the boundary conditions are said to be nonhomogeneous.

First the Weighted-integral statement is defined. Equation 8 is multiplied by a weight function (w), and integrated over the domain Ω of the problem:

$$-\int_{\Omega} w\nabla \cdot (\boldsymbol{A}\nabla u)d\Omega = \int_{\Omega} wfd\Omega. \tag{9}$$

Equation 9 is called the weighted-integral form of the equation. Applying the integration by parts to equation 9 it is obtained:

$$\int_{\Omega} \nabla w \cdot (\boldsymbol{A}\nabla u)d\Omega - \int_{\partial\Omega} w(\boldsymbol{A}\nabla u) \cdot \boldsymbol{n}d\Gamma = \int_{\Omega} wfd\Omega. \tag{10}$$

Remember that integration by parts in different dimensions is done as:

$$\int_{\Omega} \mathrm{g}\nabla \cdot \boldsymbol{f}d\Omega = -\int_{\Omega} \nabla\mathbf{g} \cdot \boldsymbol{f}d\Omega + \int_{\partial\Omega} g\boldsymbol{f} \cdot \boldsymbol{n}d\Gamma, \tag{11}$$

with $g = w$ and $\boldsymbol{f} = \mathbf{A}\nabla\mathrm{u}$.

The weight function selected, w, must satisfy that $w = 0\ on\ \Gamma_d$. Applying the boundary condition of the weight function to equation 10 the weak form is obtained:

$$\int_{\Omega} \nabla w \cdot (\boldsymbol{A}\nabla u)d\Omega = \int_{\Omega} wfd\Omega + \int_{\Gamma_n} wg_n d\Gamma. \tag{12}$$

Then, the variational problem can be stated as one of finding $u \in H^1(\Omega)$ such that $u = u_d$ on $d\Gamma$ and

$$a(w,u) = l(w) \tag{13}$$

for any weight function $w \in H^1(\Omega)$ such that $w = 0$ on $d\Gamma$, where

$$a(w,u) = \int_{\Omega} \nabla w \cdot (\boldsymbol{A}\nabla u)d\Omega, \tag{14}$$

$$l(w) = \int_{\Omega} wfd\Omega + \int_{\Gamma_n} wg_n d\Gamma. \tag{15}$$

It can be proved that the strong and weak forms are equivalent.

Therefore, the weak form of a differential equation is a weighted-integral statement equivalent to the differential equation and the specified natural boundary condition of the problem. The weak form exists for all problems (linear or nonlinear) that are described by second or higher order differential equations.

In summary, there are three steps in the development of a weak form. In the first step, the differential equation is multiplied by a weight function, $w(x)$, and integrated over the domain Ω of the problem. In the second step, integration by parts is used to distribute the differentiation evenly between the dependent variable and the weight function. In the third step, the boundary terms are modified by restricting the weight function to satisfy the homogeneous form of the specified essential boundary conditions.

3.2. Spatial discretization

The approximation to the exact solution using the FEM includes the discretization of the domain Ω in simple subdomains, called finite elements. Each finite element Ω_e is viewed as an independent domain itself over which the equations are solved. Over each one of these finite elements algebraic equations among the quantities of interest are developed using the governing equations of the problem in its weak form (equation 12) or in the weighted-integral form (equation 9). Then the relationships from all elements are assembled (i.e., elements are put back into their original positions of the total domain) using interelement relationships. The collection of finite elements in a domain is called the finite element mesh of the domain.

In the finite element method, an approximate solution to equation 8 is computed over each finite element. Each element Ω_e is composed of k discrete points called nodes, normally located at the element vertices. The polynomial approximation of the solution within the finite element Ω_e typically uses piecewise interpolant splines of the desired degree (linear, quadratic …):

$$u(x) = u^h(x) = \sum_i u_i N_i(x). \tag{16}$$

Where the functions of the spline basis verify: $N_i(x_j) = \delta ij$, see Figure 13.

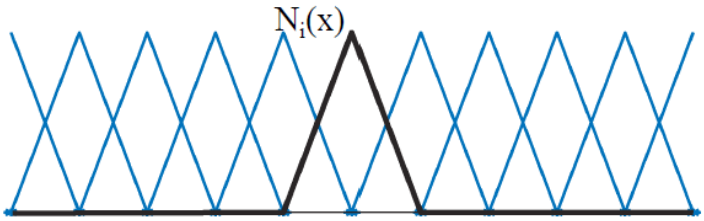

Figure 13 - Spline basis shape used normally as shape function. Source: [40]

In order to take the prescribed values into account, the coefficients corresponding to Dirichlet or essential boundary conditions (known values) are fixed:

$$u_h^e = \sum_{j \notin B} u_j N_j(x) + \sum_{i \in B} u_D(x_i) N_i(x) = \sum_{j \notin B} u_j N_j(x) + \psi(\mathrm{x}). \tag{17}$$

Therefore, $u^h(x)$ verifies (accounting for the interpolation error) the essential boundary condition: $u = u_D$ on Γ_d and $N_i(x) = 0$ on Γ_d for $i \notin B$(weight functions). Other techniques to introduce the prescribed values exist as: Lagrange multipliers, penalty methods, Nitsche's method, etc.

Imposing the weak form for all $w = N_i(x)$ with $i \notin B$ and substituting the discrete (or interpolated) approximation $u^h(x)$ to equation 13:

$$a\left(N_i, \sum_j u_j N_j(x) + \psi\right) = l(N_i). \tag{18}$$

Then, algebraically operating equation 18 we obtain:

$$\sum_j a(N_i, N_j)u_j = l(N_i) - a(N_i, \psi). \tag{19}$$

Equation 19 is a linear system of equations that can be written in matrix formulation:

$$\mathbf{K}u = \boldsymbol{f}, \tag{20}$$

where

$$K_{ij} = a(N_i, N_j) = \int_\Omega \nabla N_i \cdot (\boldsymbol{A}\nabla N_j) d\Omega, \tag{21}$$

and

$$f_i = l(N_i) - a(N_i, \psi) = \int_\Omega N_i f d\Omega + \int_{\Gamma_n} N_i g_n d\Gamma - a(N_i, \psi). \tag{22}$$

The integrals of equation 21 and 22 can be computed using piecewise polynomial functions (a single polynomial in each element):

$$K_{ij} = \sum_e \int_{\Omega_e} \nabla N_i \cdot (\boldsymbol{A}\nabla N_j) d\Omega. \tag{23}$$

In order to compute the global matrices $\mathbf{K}$ and $\boldsymbol{f}$, the elemental (local) matrices are assembled:

$$\mathbf{K} = \mathbf{A}_e \mathbf{K}^e, \quad f = \mathbf{A}_e \mathbf{f}^e. \tag{24}$$

The elemental matrix $\mathbf{K}^e$ contains the contribution of element Ω_e to the global matrix,

$$\begin{aligned} K_{ij}^e &= \int_{\Omega_e} \nabla N_i \cdot (\boldsymbol{A}\nabla N_j) d\Omega, && (i) = 1, \dots, nnode \\ & && (j) = 1, \dots, nnode \\ f_i^e &= \int_{\Omega_e} N_i f d\Omega. && (i) = 1, \dots, nnode \end{aligned} \tag{25}$$

Where e denotes the global element number and $nnode$ is the number of nodes in that element. The connectivity matrix provides the correspondence between the local and the global numbering:

$$\begin{aligned} \mathbf{K}^e_{(i)(j)} &\mapsto \mathbf{K}_{IJ}, \\ \mathbf{f}^e_{(i)} &\mapsto \mathbf{f}_I. \end{aligned}$$

where, (i): local number of node i (in element e) and I: global number of node I (in the FE mesh). The connectivity matrix $\boldsymbol{T}$ defines the relation between local and global numbering. The dimensions of $\boldsymbol{T}$ are the number of elements and number of nodes in each element:

$$\begin{aligned} &\dim(\boldsymbol{T}) = n_{elem} \times n_{node}, \\ &I = T(e,(i)), \qquad (i) = 1, \dots, n_{node} \\ &J = T(e,(j)). \qquad (j) = 1, \dots, n_{node} \end{aligned} \tag{26}$$

Therefore, the geometry discretization, i.e., the finite element mesh needs to define the nodal coordinates, **X**, and the element connectivity matrix, **T**. In Figure 14 there is an example of the definition of the nodal coordinates and the connectivity matrix for a very simple mesh. Then, at each element, equation 25 is solved in order to later assemble the global stiffness matrix from equation 24.

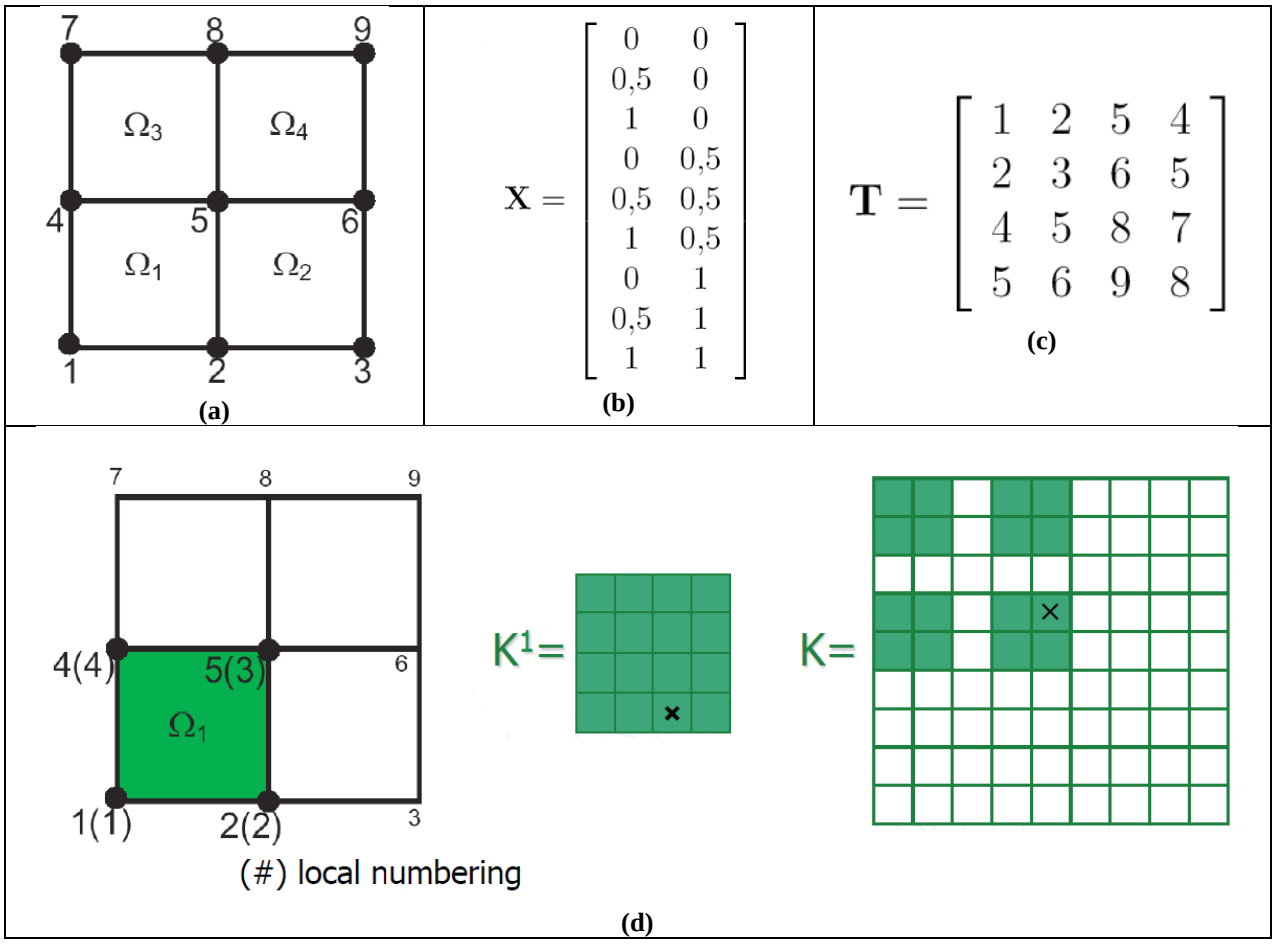

Figure 14 - Connectivity matrix definition example for a simple geometry mesh. (a) – Mesh example; (b) – Nodal coordinates matrix; (c) – Connectivity matrix; (d) – example of assembling using the connectivity matrix for the element 1. Source: [40]

3.3. Automotive steel modelling

The following guidelines for steel modelling in the automotive sector are based on the knowledge obtained working at IDIADA.

In the academic sector, the mesh models are created according to the specific necessities of each project/study and, generally, the element length used may be the smaller one that does not penalize the computational cost too much. In addition, for complex geometries or zones of interest the mesh can be refined. However, in the industry sector the final goal is to simulate at full-vehicle level, which involves all the components and subsystem assembled, becoming huge models. As reference, to run a full-vehicle model using standard clusters CPU, a runtime around 30-50h is common.

Therefore, even for simulations related to component and coupon tests, the modelling guidelines followed are the same ones than for full-vehicle simulations. Otherwise, mesh dependency or element type (i.e. fully integrated elements, reduced integrated elements, etc.) effects may produce a material card that does not capture the material behaviour at the full-vehicle model. For coarse meshes, the behaviour of the model is influenced by the element length (i.e. constitutive models depending on element size, or insufficient mesh refinement for proper geometrical description). These effects need to be taken into account, for a proper result in simulations.

Nowadays, the material models can have mesh independent behaviour for some functionalities. Others, as damage evolution, are dependent on the mesh refinement, and usually are calibrated for a certain element length range, and they should not be used for other mesh refinements. Sometimes the numerical solvers treat internally this issue and other times it is the user that needs to take this into account, as is the case for the methodology presented in this project. One part of the calibration is to ensure that the material card's behaviour is mesh independent. This will be explained in further details in chapters 5 and 6.

In this full-vehicle environment the mesh length for cars is desired to be equal or bigger than 3-4 mm and for buses the minimal desired length mesh is 10mm. In order to achieve those ranges there are certain specifications for the treatment of flange, holes, radius, rivets, etc. The client, according to their internal guidelines, usually defines those specifications. Normally, minimum distance thresholds are defined for flanges, holes, etc. and when the features are smaller than that threshold they are not represented in the FEM model.

In a full vehicle model the majority of elements are shell elements. But other elements are also present as solid elements, cohesive elements, etc… For steel sheets or steel tubes shell elements are normally used. In some particular cases as casted steels, the application of solid elements is necessary and thus, developed methodologies should work in both element types.

Also, due to the large number of elements present at a full-vehicle model, normally reduced integration is used instead of full integration. This is done with the main purpose of reducing the computation cost of running a full vehicle model. However, when damage is also defined in the material, it is recommendable to use reduced integration in order to have one single damage value for each element. Fully-integrated elements may give non-realistic damage values for the element when only some gauss points are damaged and the average is computed.

For this project, the specimens of the material testing have been designed and meshed by IDIADA. The real test conditions are applied by means of imposed boundary conditions for the nodes in the clamping/supported zone. This is done in the software ANSA [12]. The simulation of the tests is performed in LS-DYNA [45], which is a solver widely used to perform finite element calculations in the automotive industry for crash analysis.

4. Constitutive models

The objective of this chapter is to present the material-dependent physical behaviour mathematically described by means of the constitutive equations also known as material models. The balance equation and its discretization by means of the FEM model were presented in the previous chapter. However, depending on the material description used, different stress-strain behaviour will occur in bodies with the same state of stresses and the same geometry.

A brief overview of the elasto-plasticity formulation for steels (ductile material) is presented in this chapter and also some damage and failure formulations are shown. The theory presented here is based on the book *Materials Science and engineering an introduction* [16] and the subject *Numerical models for the civil and structural engineering* from the master degree in Civil Engineering at the UPC [18], [19].

The mechanical behaviour of materials reflects the relationship between its response, or deformation, to an applied load or force. The mechanical properties of materials are ascertained by performing designed laboratory experiments that replicate as nearly as possible the service conditions. The aim of these tests is to allow determine stress and strain distributions within the members that are subjected to a well-defined load. Once this characterization is done, those stress analyses can be used to simulate the material response in order to produce and fabricate materials or structures to meet service requirements. This necessarily involves the understanding of the relationships between microstructure (i.e. internal features) of materials and their mechanical properties.

4.1. Elastic properties

The degree to which a structure deforms or strains depends on the magnitude of an imposed stress. When a metal body is stressed in tension and at relatively low levels, stress and strain are proportional to each other following the Hooke's law:

$$\sigma = E\epsilon. \tag{27}$$

Where the constant of proportionality, E, is the modulus of elasticity, or *Young's modulus*. This modulus may be thought of as stiffness, or a material's resistance to elastic deformation. The greater the modulus, the stiffer the material, i.e. the smaller the elastic strain that results from the application of a given stress.

On an atomic scale, when a steel body is subjected to a force, the bonds between atoms are stretched but not broken at first. Therefore, a macroscopic elastic strain is manifested as small changes in the interatomic spacing and the stretching of interatomic bonds. As a consequence, if the load is removed while the stress is still in the elastic regime the body will recover its original form and no permanent deformations will remain.

Generally, it has been assumed that elastic deformation is time independent, i.e., that an applied stress produces an instantaneous elastic strain that remains constant over the period of time the stress is maintained. If the load is released of the load the strain immediately returns to zero. However, in most engineering materials, there is a time-dependent elastic strain component. This time-dependent elastic behaviour is known as anelasticity, and it is due to time-dependent microscopic and atomistic processes that are attendant to the deformation. But for metals, the anelastic component is normally small and is often neglected.

When a tensile stress is imposed in a specimen, as result of the elastic elongation along the tensile direction (arbitrarily taken the z direction) there will be constrictions in the later directions perpendicular to the applied stress. For isotropic materials and when the applied stress is uniaxial the ratio of the lateral and axial strains is the parameter termed Poisson's ratio:

$$\nu = -\frac{\epsilon_x}{\epsilon_z} = -\frac{\epsilon_y}{\epsilon_z}. \tag{28}$$

The maximum value for ν for which there is no net volume change is 0,5. For metals, values of Poisson's ratio range between [0,25 - 0,35] being 0,33 commonly used for mild and AHSS steels when no data is available.

4.2. Elasto-plastic deformation

The elastic deformation persists until the yield stress σ_y is reached. σ_y is the amount of stress necessary to produce a small amount of non-reversible strain (plastic strain), marking the end of the elastic region (Hooke's law, Equation 27, ceases to be valid when strain is increased beyond this point). In classical theory, it was considered that the yield stress σ_y could be found as the intersection of the strain-stress diagram with the line of slope E and passing through a strain of 0.002. Generally for most metallic materials, elastic deformation persists only to strains of about 0,005. As the material is deformed beyond this point, the stress is no longer proportional to strain and permanent non-recoverable, or plastic deformation, occurs.

Beyond the yield stress, σ_y, from an atomic perspective, plastic deformation corresponds to the movement of dislocations, term coined by G. I. Taylor [63]. Dislocations are crystallographic defects or irregularities within a crystal structure. Dislocation can move when atoms from one of the surrounding planes near the irregularity break their bonds and rebond with the atoms at the irregularity plane. These mobile dislocations are the source of plastic deformations in metals [60]. Askeland [3] describes the dislocation processes that cause the observable plastic behaviour. In Figure 15 there is a schematic representation of the dislocation movement steps due to the application of a shear stress in a crystalline structure.

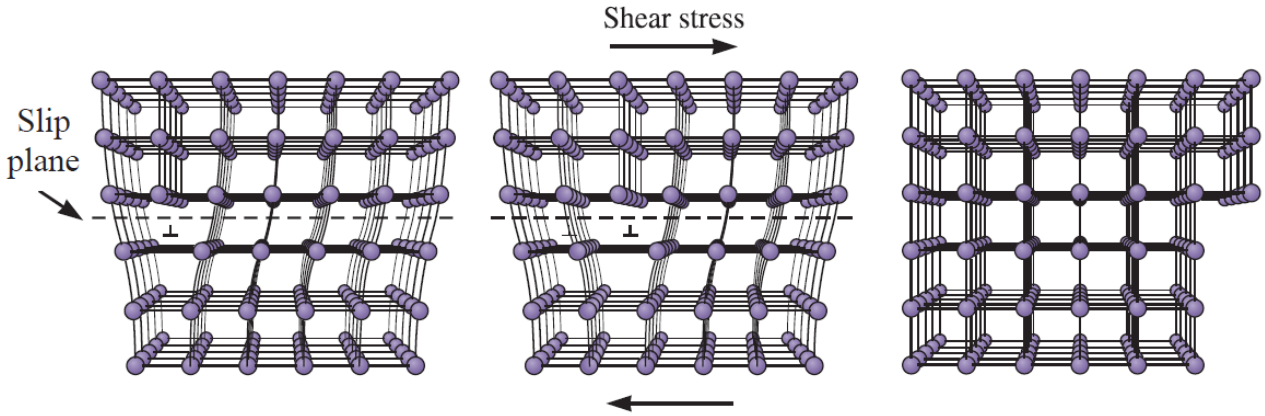

Figure 15 – Schematic representation of an edge dislocation movement in a crystal structure. Source: [3]

If the load is removed in the plastic strain range the body will have some elastic recovery but some permanent deformation caused by the dislocation moving will remain. High strength steels have greater elastic recovery than mild steels at the same total strain level, for example.

After yielding, the stress necessary to continue plastic deformation in metals increases to a maximum and then decreases to the eventual fracture. The ultimate strength is the stress at the maximum on the engineering stress-strain curve as is shown in Figure 16.

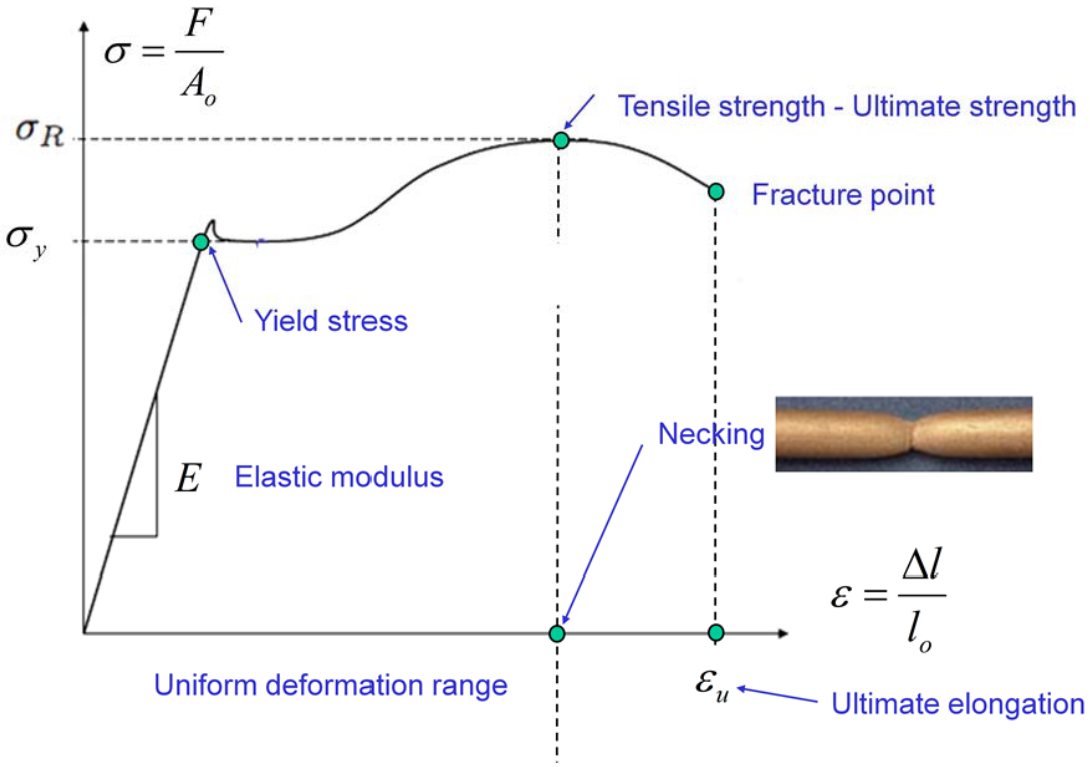

Figure 16 - Typical engineering stress-strain behaviour for loading until fracture. Source: [19]

After a certain amount of stress is applied, necking will appear and the material will begin to move toward fracture; this stress is known as Ultimate strength. Usually, the ultimate strength is the maximum stress on strain-stress diagram. The amount of energy than the steel can absorb before fracture is related to the area under the strain-stress curve through the elastic region, yielding, strain hardening, and necking.

The total elongation in the material during deformation is originated from two sources, elastic and plastic contributions. Therefore, the plastic strain can be evaluated as:

$$\varepsilon_T = \varepsilon_p + \varepsilon_e. \tag{29}$$

Where ε_p is the plastic strain, ε_e is the elastic strain and ε_T is the total true strain. According to the Hook's law equation 29 can be reformulated as:

$$\varepsilon_T = \varepsilon_p + \frac{\sigma}{E}. \tag{30}$$

4.2.1. Yielding criteria

There is a variety of criterion to characterize the material yielding [5], [14], [49]. For ductile materials the definition of a yield surface is a common technique. The state of stresses that are inside the yield surface are in the elastic regime and the stress state that lies on the surface have reached its yielding point and the material enters the plastic regime. Further deformation of the material causes the stress state to remain on the yield surface, even though the shape and size of the surface may change as the plastic deformation evolves. Two of the most often implemented theories are: Tresca theory and von Mises theory.

In order to define the yield surfaces, an equivalent stress is defined that is a scalar value computed as a function of the triaxial stress state to be compared to the yielding value. Figure 17 represent this equivalence.

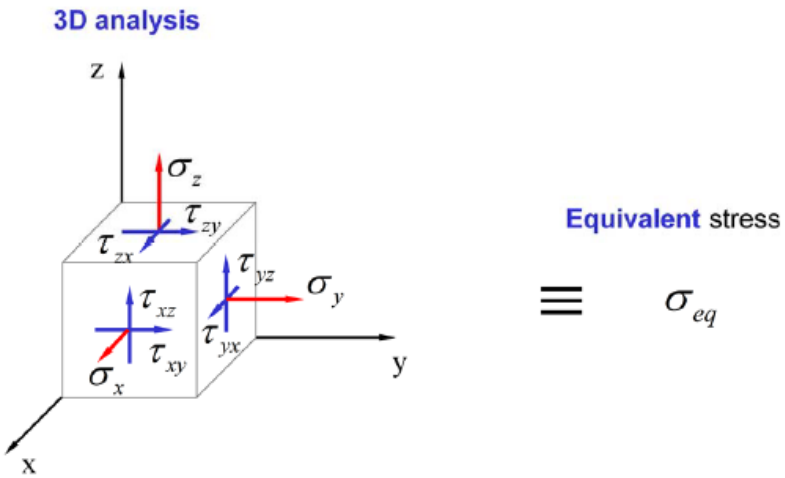

Figure 17 - Representation of the 3D tensional state and the equivalence to an scalar value, the equivalent stress. Source: [19]

The Tresca yield criterion, also known as maximum shear stress theory, is expressed as:

$$\frac{1}{2}\max(|\sigma_1 - \sigma_2|, |\sigma_2 - \sigma_3|, |\sigma_3 - \sigma_1|) = \sigma_{eq_{Tresca}}. \tag{31}$$

Where σ_1, σ_2 and σ_3 are the principal stresses. The Tresca criterion is equivalent to saying that yielding will occur at a critical value of the maximum shear stress, consistent with micromechanical behaviour of crystals, involving slip and dislocation motion.

The von Mises criterion, also known as the maximum distortion energy criterion, defines the beginning of yielding for a ductile material when the second deviatoric invariant J_2 reaches a critical value [28], [66]. The equivalent von Mises stress is expressed in principal stresses as:

$$\sqrt{\frac{1}{2}[(\sigma_1-\sigma_2)^2+(\sigma_2-\sigma_3)^2+(\sigma_3-\sigma_1)^2]}=\sigma_{eq_{Mises}}. \tag{32}$$

In Figure 18 both yield surfaces are compared:

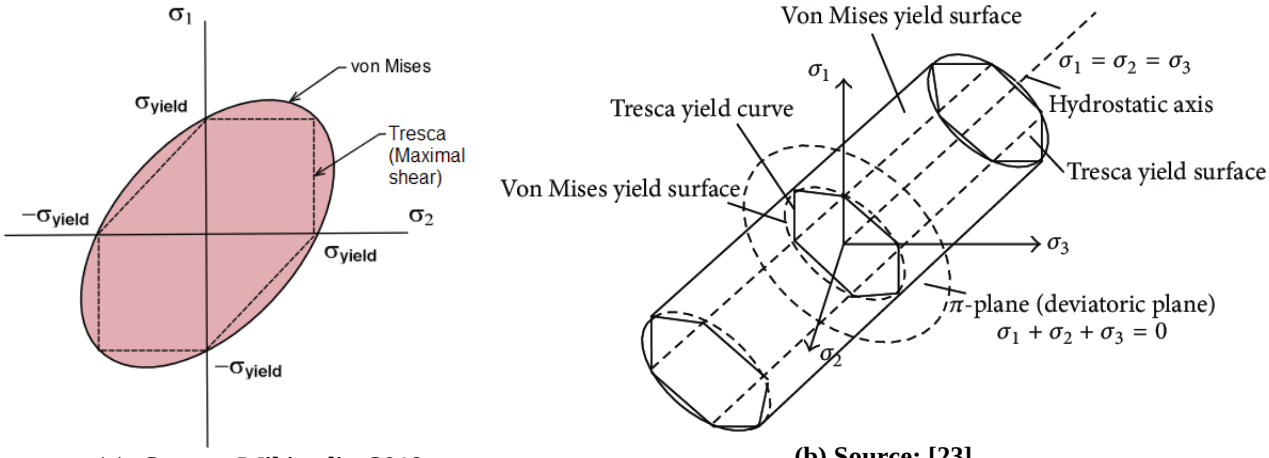

(a) Source: Wikipedia, 2019 **(b) Source: [23]**

Figure 18 - Mathematical representation of Tresca criterion and von Mises criterion yield surfaces. (a) – For 2D (planar) loading conditions ($\sigma_3 = 0$); (b) – For three-dimensional stress states

The yield criterion theory defines the shape of the yield surface. Meanwhile, the size of the yield surface depends on the material yield stress. Initial size and the posterior evolution of the yield surfaces are then, characteristics of each material.

4.2.2. Hardening laws

The yielding surface is defined as:

$$\phi(\sigma,\sigma_0)=\sigma_{eq}(\sigma)-\sigma_0\leq 0. \tag{33}$$

Where σ_0 is the yield stress of the material and σ_{eq} the equivalent stress that should be defined using one yielding theory, for example Tresca or von Mises. The yielding surface defines 3 regions according to classical plasticity theory:

$$\begin{aligned}&\text{Elastic region: } \phi<0,\\ &\text{Plastic region: } \phi=0,\\ &\text{Inadmissible region: } \phi>0.\end{aligned} \tag{34}$$

The perfect plasticity theory states that the yield surface related to stresses does not evolve with the plastic deformation. Materials of application in the automotive industry, but, do not usually show this perfect behaviour. Therefore, more complex plasticity theories have been developed in order to properly capture the hardening effect.

Since plastic deformation is an effect that affects the whole stress tensor, it is usually computed by equivalent stress-strain relationship. After, the different effects that plasticity can show over the different components of the stress and strain tensors are considered by the decomposition of the equivalent stress and strain parameters into the tensor components. From the different methodologies for equivalent stress computation, the Von Misses stress is the most used method in the automotive framework. In order to relate it to an equivalent variable related to strain, the effective plastic strain is defined:

$$\varepsilon_{ps} = \sqrt{\frac{2}{3}\varepsilon^p : \varepsilon^p}. \tag{35}$$

Physically it can be interpreted as the total amount of deformation plastic suffered by the material.

Although hardening modifies the position of the yield point, it is possible to treat both effects separately. The yield point is considered fixed at its first position σ_0 and the hardening effects are added incrementally whenever needed. In Figure 19 different hardening laws applied in numerical solvers are shown.

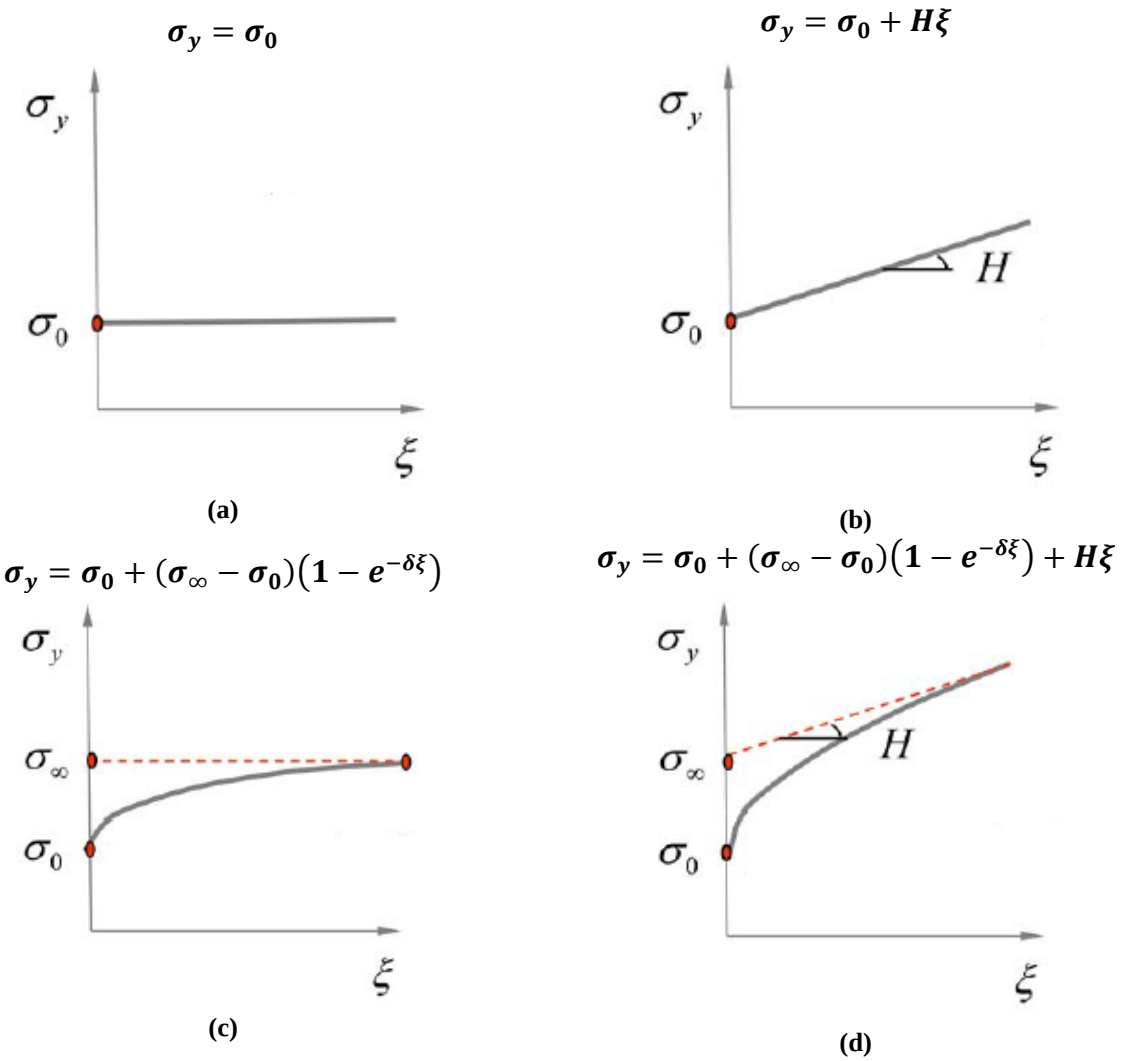

Figure 19 - 4 different hardening laws applicable to numerical solvers. (a) – Perfect plasticity; (b) – Linear hardening; (c) – Saturation law; (d) – Saturation law plus linear hardening. Source: [19]

For isotropic hardening, $\sigma_y = \sigma_y(\varepsilon_{ps})$ the evolution of the yield surface is obtained only scaling the original surface in function of the effective plastic strain ε_{ps}

There are 3 common isotropic hardening laws used:

Linear hardening: $\sigma_y = \sigma_{y0} + K \cdot \varepsilon_{ps}.$ (non-realistic) (36)

Hollomon law: $\sigma_y = K \cdot (\varepsilon_{ps})^n.$ (37)

Ludwik-Nadai law: $\sigma_y = K \cdot (\varepsilon_{ps0} + \varepsilon_{ps})^n.$ (38)

In the Hollomon's expression the n is the strain-hardening exponent and K is the strength coefficient. The strain-hardening exponent measures the ability of a metal to strain-harden, i.e., larger magnitude of the strain-hardening exponent indicates larger degrees of strain hardening.

There are many different complex hardening laws that can be found in literature, such as [10], [11], [48].

Table 2 summarize the necessary elements to define the elasto-plastic constitutive model for uniaxial and multiaxial stress state.

Table 2 – Elasto-plastic constitutive model bases

Elasto-plastic constitutive model		
	Uniaxial stress	**Multiaxial stress**
Strain decomposition	$\varepsilon = \varepsilon_p + \varepsilon_e$	$\boldsymbol{\varepsilon} = \boldsymbol{\varepsilon}_p + \boldsymbol{\varepsilon}_e.$
Hooke's law	$\sigma = E\varepsilon_e$	$\boldsymbol{\sigma} = \boldsymbol{D}_e\boldsymbol{\varepsilon}_e$
Plastic admissibility	$f(\sigma) \leq 0$	$f(\boldsymbol{\sigma}) \leq 0$
Plastic flow rule	$\dot{\varepsilon}_p = \dot{\lambda}\, sgn\sigma$ $\dot{\lambda} \geq 0$	$\dot{\boldsymbol{\varepsilon}}_p = \dot{\lambda}\, f(\boldsymbol{\sigma})$ $\dot{\lambda} \geq 0$
Complementary condition	$\dot{\lambda} f(\sigma) = 0$	$\dot{\lambda} f(\boldsymbol{\sigma}) = 0$

4.3. Fundamentals of Fracture and Damage Mechanics

For engineering materials, two fundamental fracture modes are considered: brittle and ductile. Brittle fracture is when no plastic deformation occurs and ductile materials exhibit substantial plastic deformation prior, and/or during failure. Metals are included in the ductile failure category due to their well-known ductility.

Consequences of damage itself are the reduction on strength and stiffness caused by propagating and interacting defects such as voids, cracks or delamination. Ductile fracture surfaces have some special features that differ from the brittle fracture surfaces, as Figure 20 shows.

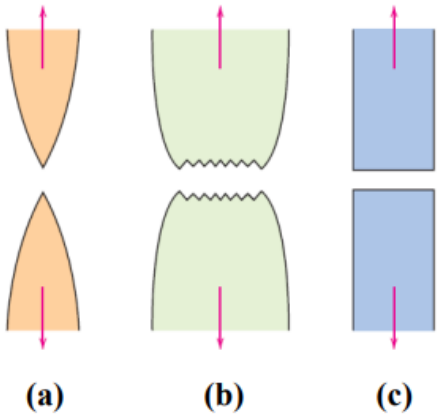

Figure 20 - Types of failure surfaces: (a) – Highly ductile fracture, very narrow necking; (b) – Moderate ductile fracture with some necking appearing; (c) – Brittle fracture without plastic deformation. Source: [16]

At microscopic level, there are three main stages that can be observed in a ductile fracture: nucleation, growth and coalescence of voids as shown in Figure 21. Firstly, micro-voids nucleate at inclusions or second-phase particle when the inter-facial bonds between the particle or inclusion and the matrix are broken by a certain stress [2]. Secondly, the voids grow until the matrix attains to the plastic limit-load state by means of plastic strain and hydro-static stress [65]. Thirdly, the inter-voids matrix happens to plastic limit-load failure across the sheet with strain localization between voids. Then it begins to neck down internally between the adjacent voids [21]. The voids further coalesce and the inter-void matrix cracks with a "knife-edge" fracture surface [65].

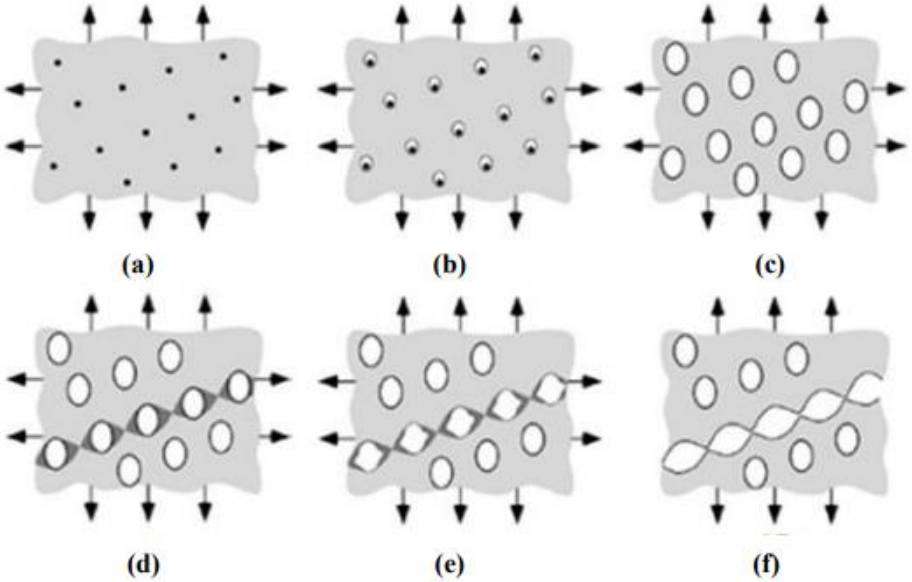

Figure 21 - Principal three stages in a ductile fracture: (a) – inclusions in a ductile matrix; (b) – void nucleation; (c) – void growth; (d) – strain localization between voids; (e) – necking between voids; (f) – void coalescence and fracture. Source: [1]

The classical considerations in Continuum Mechanics cannot consider the formation of voids which means new surfaces in the body mass. Continuum Damage Mechanics (CMD) detects the formation of a macroscopic crack due to the formation and growth of microdefects in the body. These microdefects are generally described at macroscopic level by the definition of a loss of stiffness (degradation) of the material.

The Continuum Damage Theory was firstly introduced by Kachanov [35]. The damage parameter is defined according to Lemaire and Chaboche [42], [43] as the surface density of discontinuities:

$$d = 1 - \frac{A_{eff}}{A} = \frac{A_{defect}}{A}, \tag{39}$$

with:

$d = 0$ undamaged state,
$0 < d < 1$ damaged state,
$d = 1$ totally damaged material.

Where A is the cross section area including the area of voids and A_{eff} is the cross section area excluding the voids area. Figure 22 shows the effective area and the overall section area including the micro-defects.A and A_{eff}.

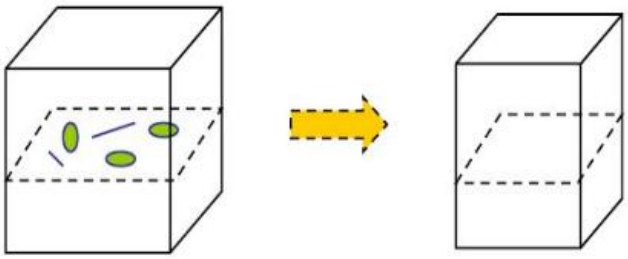

Figure 22 - Current damaged section area and the effective section area. Source: [27]

Due to damage, the reduction of the cross section has an effect on the stress recording the global response. The Lemaitre's formulation is a basic relation to couple the damage to the stress using the definition of true stress σ_{true} (see equation 3) together with equation 39:

$$\sigma_{eff} = \frac{F}{A_{eff}} = \frac{\sigma_{true}}{1 - D} \Rightarrow \sigma_{true} = (1 - D)\sigma_{eff}. \tag{40}$$

Equation 40 is the basic damage theory and is present in most damage models. It is the fundamentals of the different failure models. One of the most important differences between the different damage models is the damage evolution. Currently, one of the more complete ways of describing the damage envelope is the Johnson Cook model [33], with some modification to consider tensile test. After, damage evolution can follow different laws, as example:

$$\dot{D} = \frac{\dot{\epsilon_p}}{\dot{\epsilon_f}}. \tag{41}$$

Where $\dot{\epsilon_p}$ is the equivalent plastic strain rate and $\dot{\epsilon_f}$ is the equivalent plastic strain at failure. There are other damage evolution laws that are also used, like the evolution law used in GISSMO explained in Chapter 5.

Material failure is dependent of the stress state as shown by Bridgman [15] who observed that the ductility of a material is highly sensitive to pressure. Later, McClintock [46] and Rice and

Tracey [57] inferred an expression of the relationship between the stress triaxiality and the strain to fracture by analysis of the void growth. To define the stress state is widely used the definition of the triaxiality parameter [6]:

$$\eta = \frac{I_1}{\sigma_{eq}}. \tag{42}$$

Where σ_{eq} is the von Mises stress (see equation 32) and I_1 is the first stress invariant

$$I_1 = \frac{\sigma_1 + \sigma_2 + \sigma_3}{3} \tag{43}$$

where σ_1, σ_2 and σ_3 are the principal stresses.

For modern ductile Fracture Mechanics, the criterion for fracture initiation is proved by means of stress triaxiality by void growth mechanics modelling [41], [62]. Instead, for Continuum Damage Mechanics the criteria for fracture initiation is based on the initiation and propagation-toughness-mechanics [29], [39]. There is also damage model that depends in the hydrostatic pressure and the Lode angle [72].

Additionally, more specific relationships between the stress triaxiality and the strain to fracture for different materials have been studied from large number of experimental tests. Hancock and Mackenzie [26] studied tensile test with pre-notched round specimens. This fracture model was extended by Johnson and Cook [33] combining the effect of temperature and strain rate.

In a larger range of triaxiality, the fracture locus describing different relationships of the stress triaxiality with a strain to fracture was studied experimentally in aluminium by Bao [8], [9]. In Figure 23 is shown the fracture locus obtained by Bao [9].

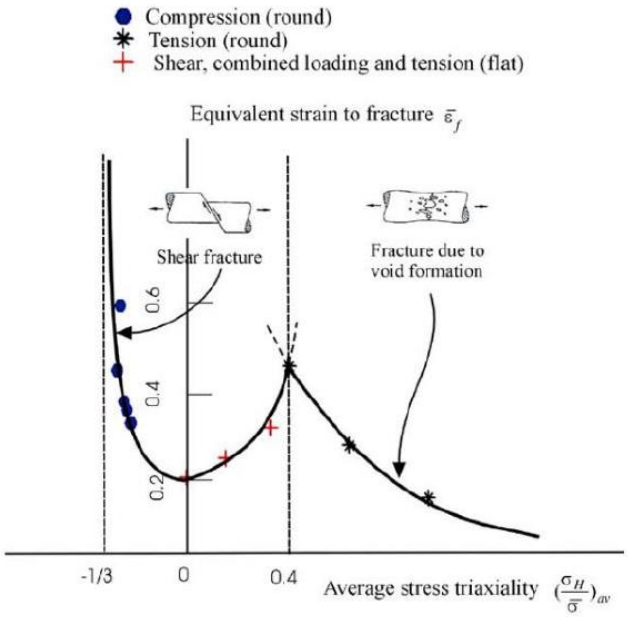

Figure 23 - Stress triaxiality versus equivalent strain to fracture dependence for 2024-T352 aluminium alloy. Source: [68]

The equations describing the 3 different branches are:

$$\overline{\varepsilon_f} = 0.1225 \times \left(\eta + \frac{1}{3}\right)^{-0.46}, \quad \text{for } -\frac{1}{3} < \eta < 0, \tag{44}$$

$$\overline{\varepsilon_f} = 1.9\eta^2 - 0.18\eta + 0.21, \quad \text{for } 0 < \eta < 0{,}4, \tag{45}$$

$$\overline{\varepsilon_f} = 0.1\eta^{-1}, \quad \text{for } 0{,}4 < \eta < 0{,}95. \tag{46}$$

The equation 44 is based in the study done by Wierzbicki and Werner [69] and the equations 45 and 46 where obtained by parabolic fitting with the experimental data.

4.4. Strain-rate effects

Most engineering materials are strain rate dependent materials. This means the response of the material is dependent of the loading rate, i.e., the strain rate. In Figure 24 it is shown a possible behaviour of a strain rate dependent material.

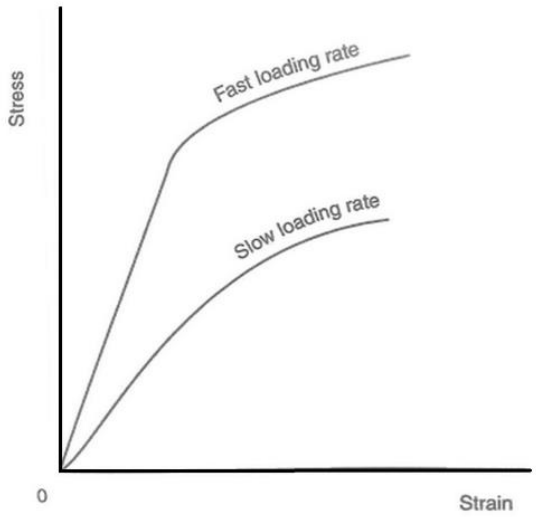

Figure 24 - Influence of the strain rate dependence of a material represented in the true stress – true strain graph. Source: [58]

In the case of steels, the strain rate effect at the elastic behaviour is very small. But in cases of crash events where the failure is present the strain rate in steels may have more relevance in the response of the material. Therefore, it should be important to include in the material model definition the strain rate influence.

Johnson and Cook [33], [34] studied the effects of the temperature and the strain rate on ductile fracture based on the experiments done by Hancock and Mackenzie [26] and developed an experimental relationship that states the influences of strain, temperature and strain rate on Von Misses stress:

$$\bar{\sigma} = \left(A + B\varepsilon_p^n\right)\left[1 + Cln\left(\frac{\dot{\varepsilon}}{\dot{\varepsilon}_0}\right)\right][1 - (T^*)^m\,]. \tag{47}$$

Where A, B, C, n, m are five material constants to be obtained from experimental data, ε_p is the effective plastic strain (see equation 35), $\dot{\varepsilon}$ and $\dot{\varepsilon}_0$are the current and reference strain rates and T^* is the homologous temperature defined as:

$$T^* = \frac{T - T_R}{T_m - T}. \tag{48}$$

Where T_R is the room temperature and T_m is the material melting temperature. The first term of equation 47 states the relation between quasi-static stress and strain at room temperature (note that is very similar to Hollomon hardening law equation 37). The second term states the effect of strain rate. The last term states the effect of temperature.

4.5. Characterization approaches at the automotive industry

Most commercial numerical software allows the definition of plastic behaviour by means of material curves. Therefore, the parameters of the hardening laws do not need to be calibrated. Hardening is directly considered in the input curve. There are some material models that can be defined by an equation, but the industry trend is to always use strain-stress curves as inputs for the material models for steels.

4.5.1. Classical approach

It uses an elasto-plastic constitutive model based on von Mises yield criteria (MAT 24 from LS-DYNA, which is explained in more detail in chapter 5) and the 50mm gauge extensometer data to define the material card.

The main limitation of this model is that the 50mm gauge data is only trustable until necking. After this point, the strain-stress data from the gauge is not representative of the real behavior of the material due to the non-linear stress distribution caused due to the non-uniform change of the cross-section of the specimen.

Classical approach does not generally consider damage definition. At most, direct elimination of elements is defined at certain threshold strain.

4.5.2. Extended approach

In order to solve the limitations of the classical approach, academia and industry developed a new technology in order to be able to register the exact stress-strain values in the whole specimen during all the duration of the test: Digital Image Correlation (DIC). This technology allows calculating the exact stresses in the necking zone [53].

The extended approach, use the data from a uniaxial tensile test recorded using the DIC technique to extend the elasto-plastic curve beyond the necking point using the correct values of true stress and true strain. Figure 25 shows an extended elasto-plastic curve used in a simulation.

However, the DIC technique is costly, making the cheap uniaxial test become expensive. This may be a drawback in the early stages of the design and development of a vehicle, where steels are usually tested to uniaxial test in order to obtain simple material models to simulate them but could be discarded in future stages of the development.

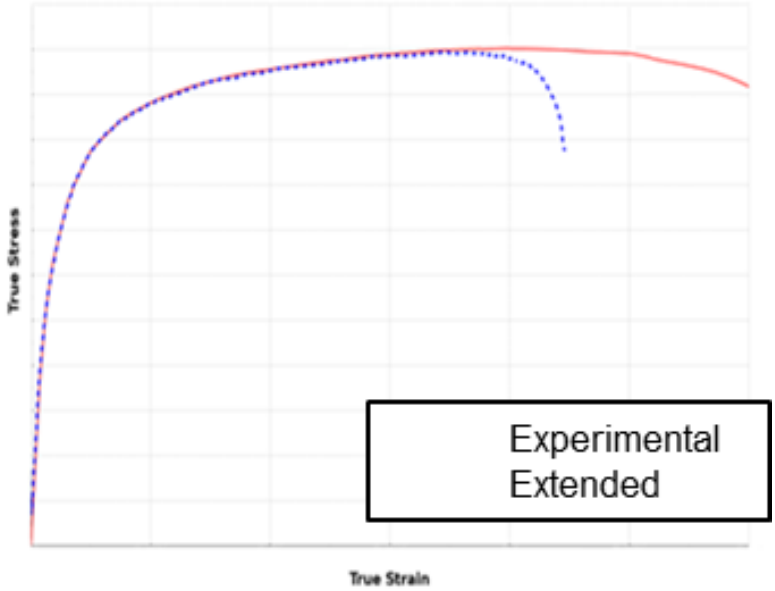

Figure 25. Simulation done using an extended elasto-plastic curve for a tensile test. Source: IDIADA

For the complete characterization methodology, Nackajima or Marciniack tests are mean to be done, in order to measure a precise failure envelope. The costs associated to testing and the complexity of measuring data and introduce it in simulation, usually leads to a similar definition of damage than in classical approach: not considering damage even when the extended approach is performed for the elasto-plastic law. At most, direct elimination of elements is defined at certain threshold strain.

4.5.3. IDIADA approach

IDIADA developed in 2018 a methodology to use the data obtained from a uniaxial tensile test using a 50mm gauge as equipment and extend the strain-stress curve generated in the classical approach to fit with the data obtained from the DIC technique [55]. This allows to keep using the cheap uniaxial tensile test using 50mm gauges and to obtain detailed data comparable to the DIC technique, reducing costs and time.

The data from the 50mm gauge is processed by an analytical formula where one parameter needs to be calibrated for each material studied. This parameter, defined as w parameter (in Chapter 6 is mentioned again), is a weighing parameter between a lineal and an exponential law.

With the calibration of the w parameter, the elasto-plastic extended curve is obtained by analytical methods. Additionally, IDIADA also developed a damage definition that can be calibrated from the same uniaxial tensile data using the GISSMO damage model from LS-DYNA, which is explained in detail in Chapter 5. For more precise measurements while maintaining low cost, an experimental campaign based on modified tensile tests is being developed.

IDIADA analytical approach allows obtaining a complete material model including damage definition from a cheap test as the uniaxial tensile test. However, there are limitations, being the main one, that the damage definition in the material model only predicts damage failure correctly when the tensional state is similar to the one in the uniaxial tensile test. Nevertheless, bending phenomenon creates this similar tensional state and is one of the most common causes of damage failure appearance in the automotive tests.

5. Material model description

In this chapter, the commercial solver used at IDIADA for the methodology developed is presented, along with its capabilities for material simulation. The capabilities of LS-Dyna® are many and include dynamic and static computations, material failure analysis and crack propagation, to name a few. In the automotive industry, LS-Dyna's explicit solving technique is widely used, excelling in the prediction of the car's behaviour and effect upon the occupants during collision.

LS-DYNA needs a "key" file to run a simulation. The "key" file is a text file that contains a series of keywords. These keywords inform the solver about how the simulation is supposed to be performed, such as which geometry, material model, boundary conditions, time step, etc. are wanted

In order to represent the steel behaviour, the LS-DYNA material 024 is used, *MAT_PIECEWISE_LINEAR_PLASTICITY (keyword), which models the elasto-plastic behaviour, and *MAT_ADD_EROSION (keyword), which model material failure. After a keyword is used the cards are defined. Each card is one line with values, flags, etc. and every keyword has associated a certain number of cards.

Furthermore, the model supports more complex material behaviour where the material is strain rate dependent. Instead of implementing one hardening curve, a table defining different strain rates which are connected to a certain hardening curve has to be implemented to capture the behaviour.

A detailed description of the LS-DYNA capabilities is found at the LS-DYNA User's Manual [45]. Following sections highlight the characteristics of the elasto-plastic model and the GISSMO model [22, 50] that is helpful in understanding the methodology developed at IDIADA for the AHSS characterization.

5.1. MAT_024 *MAT_PIECEWISE_LINEAR_PLASTICITY

MAT024 or * MAT_PIECEWISE_LINEAR_PLASTICITY is an elasto-plastic constitutive model based on von Mises yield criteria which is used to model the material behaviour until the point where instability occur. The model has an arbitrary stress versus strain curve and arbitrary strain rate dependency. Therefore, the stress versus strain behaviour can be introduced by curve instead of using parameters from an equation.

MAT024 is not able to represent the material behaviour beyond the point of uniform expansion, i.e. beyond necking the behaviour is not represented correctly. Adding the damage with *MAT_ADD_EROSION allows to represent correctly the behaviour until failure.

The input parameters implemented in the MAT024 card are primarily Young's modulus, the mass density, Poisson's ratio and the hardening of the material. The hardening curve shall cover the loading path until failure. Since most of damage models are referred to plastic strain, the plastic strain definition should be extrapolated until the final failure of the material. At section 5.3 of this chapter the parameters used in the IDIADA methodology are listed and explained.

The *MAT_PIECEWISE_LINEAR_PLASTICITY model can be applied to nonlinear elements formulations including 3D solid elements, 3D SPH particles, 3D shell elements, and thick shell elements.

5.2. *MAT_ADD_EROSION

Not all the constitutive models in LS-DYNA allow the material failure. As advanced before, the MAT_024 of LS-DYNA does not have any damage definition included. Adding the *MAT_ADD_EROSION keyword a damage model can be coupled with the elasto-plastic description of MAT_024 to add the damage properties to the model [22].

According to the LS-DYNA User's Manual Volume II [103], for the non-damage options, each of the failure criteria defined at the *MAT_ADD_EROSION cards are applied independently, and once a sufficient number of those criteria are satisfied according to the parameter NCS, defined by the user, the element is deleted from the calculation. In addition to erosion, the "generalized incremental stress-state dependent damage model" (GISSMO) or the alternative "damage initiation and evolution models" (DIEM) are available to represent the damage behaviour.

The *MAT_ADD_EROSION option can be applied to nonlinear elements formulations including 2D continuum elements, 2D particles, 3D solid elements, 3D SPH particles, 3D shell elements, and thick shell elements.

5.2.1. GISSMO

The Generalized Incremental Stress-State dependent damage Model (a.k.a. GISSMO) is a phenomenological formulation that allows for an incremental description of damage accumulation, including softening and failure. I.e. it lowers the loading capacity of the elements continuously in proportion to a damage parameter coupling the damage to the true stress.

This damage accumulation rule is given by:

$$\dot{D} = \frac{n}{\epsilon_f} D^{1-\frac{1}{n}} \dot{\epsilon_p}. \tag{49}$$

Where n is a damage exponent (DMGEXP in the card), ε_f is the equivalent plastic stain determined from the LCSDG curve (input by the user) as a function of the current triaxiality value η (if at LCSDG a curve is used as input), D is the current value of damage and $\Delta\varepsilon_p$ is the equivalent plastic strain increment.

When GISSMO is active, equation 49 is evaluated at every time step in LS-DYNA. The damage evolution of GISSMO has similarities with the Johnson-Cook damage model. The

GISSMO model describes the evolution of damage as an exponential function instead of a linear expression as stated at the Johnson and Cook damage model. GISSMO is a non-path dependent failure model.

A useful property implemented in GISSMO is the accumulation of a measure of instability, F. If a load curve defining the critical plastic strain vs. triaxiality is used as input at ECRIT parameter, the instability measure F is accumulated using the following equation:

$$\Delta F = \frac{n}{\varepsilon_{p,loc}} F^{1-\frac{1}{n}} \Delta\varepsilon_p. \tag{50}$$

Where F is the instability measure ($0 \leq F \leq 1$), $\varepsilon_{p,loc}$ is the equivalent plastic strain to instability determined from ECRIT, n is a damage exponent (DMGEXP in the card) and $\Delta\varepsilon_p$is the equivalent plastic strain increment. This offers the possibility to use a transformed Forming Limit Diagram as an input for the expected onset of softening and localization.

Also, GISSMO includes a way to compensate the mesh effects when strain localization appears (necking) at coarse mesh ($L_e > 0.5mm$) GISSMO allows the definition of element size-dependent factors which adjust the fracture curve to each element size. These are the FADEXP which is an exponent for damage-related stress fadeout and the LCREGD which is a regulation factors for equivalent plastic strain to failure.

5.3. Required parameters

At figure Figure 26, an example of an empty *MAT_PIECEWISE_LINEAR_PLASTICITY and *MAT_ADD_EROSION cards as it is used in the IDIADA methodology is shown.

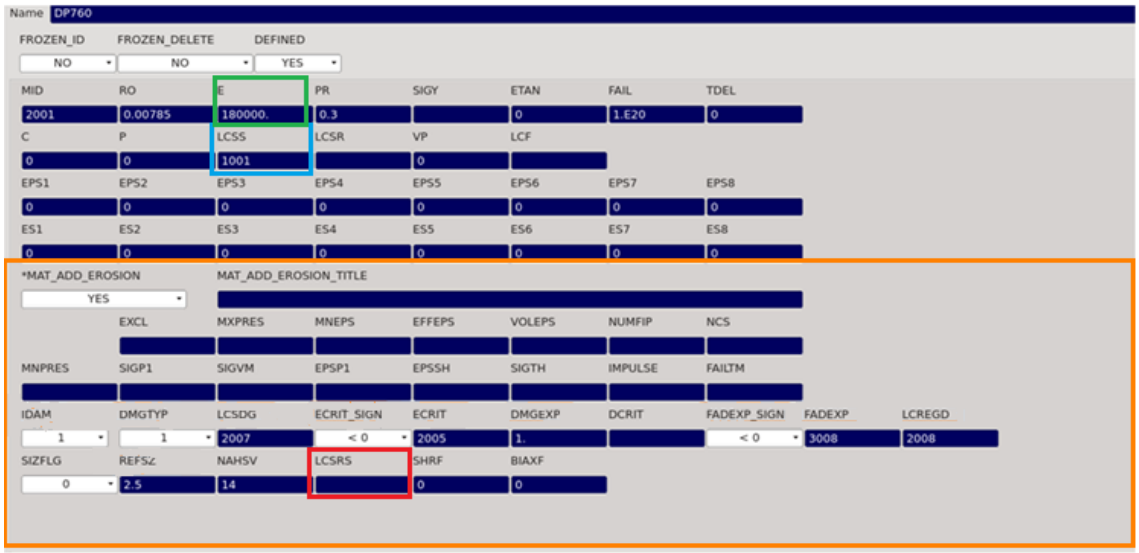

Figure 26 - Materials cards of the MAT024 and *MAT_ADD_EROSION with standard values. Source: Own

For the MAT_024 definitions only the two first cards are used and the last two cards in this methodology are ignored. The last two cards can be used to define up to 8 points of the effective plastic strain and yield stress values as an alternative to the definition of the strain rate effects. In the methodology presented in this thesis the elasto-plastic behaviour is introduced by means of a

curve and the strain rate effects by means of a table which calls different curves depending the strain-rate state of the element. The parameters SIGY, ETAN, C, P, VP, LCF of the MAT_024 first two cards are not used.

At Table 3, a list of the parameters from the * PIECEWISE_LINEAR_PLASTICITY card that are calibrated with the experimental data or are defined by the IDIADA methodology are listed.

Table 3 - Inputs of the *MAT_024 cards

Variable name	Description	Comes from
MID	LSDYNA internal material identification	The user
RO	Mass density	Directly from experimental data
E	Young's modulus	Exact measurement from experimental data
PR	Poisson's ratio	Used 0.3 for all the steels
LCSS	Effective stress versus effective plastic strain curve	Generated at the LS-OPT optimization phase of the methodology

For the *MAT_ADD_EROSION the two first cards are not used and the cards 3 and 4 contains all the information for the damage behaviour. For using the GISSMO considering failure, the parameter IDAM must be set to 1 and the parameter DMGTYP must be set to 1 also. DCRIT parameter is not used as ECRIT is defined (ECRIT is defined as a curve).

At Table 4, a list of the important parameters from the *MAT_ADD_EROSION card that are calibrated with the experimental data or are defined by the IDIADA methodology are listed.

Table 4 – Main parameters of the GISSMO model described and identified in the IDIADA methodology

Variable name	Description	Defined at
LCSDG	Load curve defining the relationship between triaxiality and equivalent plastic strain	Using an own normalized curve from data recollected by IDIADA
ECRIT	Load curve defining the relationship between triaxiality and critical equivalent plastic strain	Using an own normalized curve from IDIADA experience
DMGEXP	Exponent for nonlinear coupling damage	Equal to 1 (further studies will be done between 1 and 2 as best exponent)
FADEXP	Exponent for damage related stress fadeout	Parameter optimized using LS-OPT for the different meshes
LCREGD	Load curve defining the relationship between the element size and scalars. Makes the model mesh independent	Parameter optimized using LS-OPT for the different meshes
REFSZ	Reference element size (necessary to transfer damage to different mesh sizes)	2.5 mm is the reference size mesh
LCSRS	Load curve defining failure strain scaling factor for LCSDG vs. strain rate	Created using the experimental data to obtain the Jonhson Cook parameters for strain rate and then using IDIADA methodology to obtain the curves

The current LCSDG and ECRIT curves being used at this methodology where developed in IDIADA. At Figure 27 the ECRIT and LCSDG envelopes are represented graphically comparing them with the Von Mises envelope and the Johnson-Cook envelope.

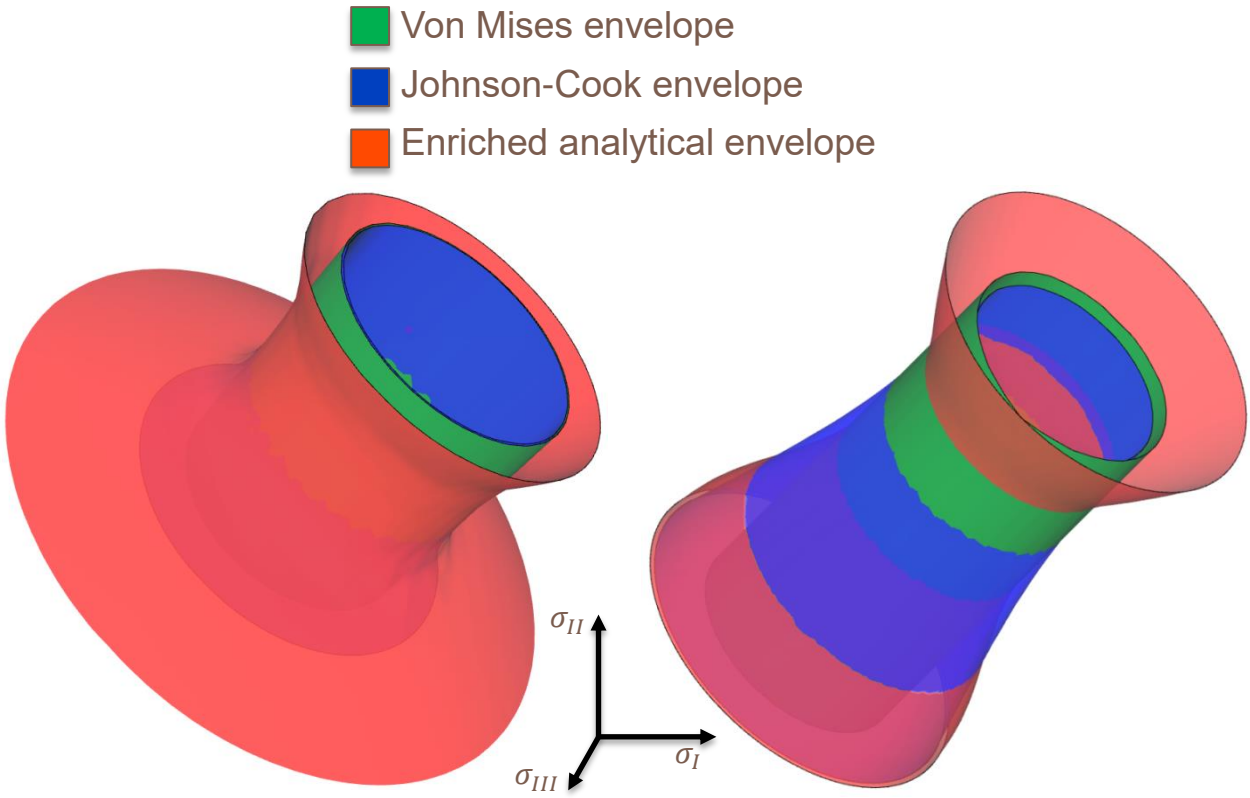

(a) **(b)**

Figure 27 – ECRIT and LSDG envelopes represented in the principal stress space. (a) – ECRIT; (b) – LCSDG curve. Source: IDIADA

6. Process automation

In this chapter the models used to calibrate the parameters are presented and a general explanation of the elements present in the methodology is given.

This project will use the software called LS-OPT [44] to perform the parameter calibration (optimization). The comparison will be done with two different complex load cases. LS-OPT looks for minimizing the difference between these with a chosen optimization method. One commonly used method is the Mean Square Error technique, MSE, which measures the differences of the two function values. The method that is used to do the optimizations in this thesis is called Partial Curve Matching, PCM. The PCM method evaluates the area between the curves, instead of just the vertical distance. This method is used since it works better than others when the curve has a steep slope, which most of the material tests have. Witowski, Feucht and Stander [70] describe the optimization method in further detail.

This project will use the software called META [13] from BETACae Systems to perform the post-process of the results obtained from the numerical solver LS-DYNA. META allows the user the creation of so called sessions that are a list of META commands in a file to reproduce the action automatically when executed. This allows the automation of the post-process present in the LS-OPT model.

The methodology has been split in two models: the quasi-static model and the strain-rate model. The quasi-static model is a stand-alone model that gives as output the material card including the damage definition by means of GISSMO. On the other hand, the strain-rate model needs the outputs from the quasi-static model to start. This has been done in order to be able to create material cards without strain-rate and when is wanted the other model is also used. This way, depending on the client request one or both models are used.

Both models need as input an excel file developed at the previous methodology [55]. That excel has been improved in order to contain all inputs necessary for the LS-OPT model and the scripts involved, so the user only need to introduce all data in one single file.

6.1. Quasi-static model definition

The quasi-static model reads the inputs from the excel file. Then generates all the files needed in the model that depends of the inputs. A first calibration of the elastoplastic curve is done: w calibration. The w parameter optimization is done at the 1mm mesh model.

The main file of the quasi-static model is the *AHSS_OPCOM_main_model_CM.lsopt*. The “CM” refers to curve mapping since a curve mapping technique is used for the error measures between the curves for the curve matching.

For a new steel characterization only the Excel file of the methodology needs to be changed. All the other files of the model are copied directly to a new working folder. While running there is a series of scripts that will generate new files or modify the existing ones.

6.1.1. Model structure

The model consists in a large quantity of files (scripts, LSOPT files, META sessions, LSDYNA files, etc...) and the main lsopt file calls the other lsopt files which perform the different optimization steps. In Table 5 and Table 6 there is a brief summary of all the files involved in the model including a description of what they are and what they do.

In Figure 28, the stage structure defined at LS-OPT for the main lsopt file *AHSS_OPCOM_main_model_CM.lsopt* can be seen. A total of 15 stages are defined in the main model: 9 of them are user-defined stages that launch octave scripts and the other 6 are lsopt stages that launch other lsopt files. This means that in total 6 optimization processes are done with this methodology.

In Table 7 there is a list of the files that are used as input for each stage and the Extra input files needed. There is also a column for the files that are transferred to each stage from stages above them. For the case of an lsopt stage to work, all the files that the inner level will use need to be added at the extra input files section of the stage.

Table 5 - List of files of the quasi-static model

Nº	File name	Type	Description
1	*AHSS_OPCOM_main_model_CM.lsopt*	LSOPT	Main lsopt file which is opened with LSOPT
2	*2_5_mm_w_shell.lsopt*	LSOPT	Lsopt file that defines the w optimization step
3	*1_mm_FADEXP_RegFactor_CM.lsopt*	LSOPT	Lsopt file that defines the 1 mm mesh optimization step
4	*2_5_mm_FADEXP_RegFactor_CM.lsopt*	LSOPT	Lsopt file that defines the 2.5 mm mesh optimization step
5	*4_mm_FADEXP_RegFactor_CM.lsopt*	LSOPT	Lsopt file that defines the 4 mm mesh optimization step
6	*6_mm_FADEXP_RegFactor_CM.lsopt*	LSOPT	Lsopt file that defines the 6 mm mesh optimization step
7	*10_mm_FADEXP_RegFactor_CM.lsopt*	LSOPT	Lsopt file that defines the 10 mm mesh optimization step
8	*Tensile_Test_1.key*	LSDYNA	Main Ls-dyna file for the 1 mm mesh. Contains the heading, nodes, elements, sets, cross section and boundaries It has 2 includes: *Material.k* and *properties.k*
9	*Tensile_Test_2_5.key*	LSDYNA	Main Ls-dyna file for the 2.5 mm mesh. Contains the heading, nodes, elements, sets, cross-section and boundaries It has 2 includes: *Material.k* and *properties.k*
10	*Tensile_Test_4.key*	LSDYNA	Main Ls-dyna file for the 4 mm mesh. Contains the heading, nodes, elements, sets, cross section and boundaries It has 2 includes: *Material.k* and *properties.k*
11	*Tensile_Test_6.key*	LSDYNA	Main Ls-dyna file for the 6 mm mesh. Contains the heading, nodes, elements, sets, cross-section and boundaries It has 2 includes: *Material.k* and *properties.k*
12	*Tensile_Test_10.key*	LSDYNA	Main Ls-dyna file for the 10 mm mesh. Contains the heading, nodes, elements, sets, cross section and boundaries It has 2 includes: *Material.k* and *properties.k*
13	*properties.k*	LSDYNA	Ls-dyna include that contains the part and section shell of the elements (thickness of the shell is defined here)
14	*Session_tensile_OPCOM_w_shell_local.ses*	META	Main Meta session for the post process for the results of the w optimization stage. Includes the annotations that will be read by the Optimizer Setup
15	*OPCOM_w_shell.ses*	META	Meta session with the Optimizer Setup of META configuration for the

			w optimization step. It calls the session *Session_tensile_OPCOM_w_shell_local.ses* It defines 2 responses (from 2 annotations made on the post-process) named “max_exp_to_exp” and “max_exp_to_sim”
16	*OPCOM_w_shell.ses.results*	META	Meta file with the format needed by the Optimizer Setup that will store the results configured at the file *OPCOM_w_shell.ses*
17	*Session_tensile_OPCOM_FADEXP_RegFactor_local_CM.ses*	META	Main Meta session for the post process of the results for the mesh optimization stages. Includes the annotations that will be read by the Optimizer Setup
18	*OPCOM_FADEXP_RegFactor_CM.ses*	META	Meta session with the Optimizer Setup of META configuration for the mesh optimization steps. It calls the session *Session_tensile_OPCOM_ FADEXP_RegFactor_CM.ses* It defines 1 history named “Simulation_all”
19	*OPCOM_FADEXP_RegFactor_CM.ses.results*	META	Meta file with the format needed by the Optimizer Setup that will store the results configured at the file *OPCOM_FADEXP_RegFactor_CM.ses*
20	*load_save_curve.ses*	META	Meta session used to load the file *simulation_truncated* generated by the script *simulation_end_lsdyna.m* and save it with the Optimizer Setup of Meta It defines 1 history named “Simulation_truncated”
21	*load_save_curve.ses.results*	META	Meta file with the format needed by the Optimizer Setup that will store the results configured at the file *load_save_curve.ses*
22	*Methodology_input_process.xlsx*	EXCEL	Excel file with all the inputs (Defined by the user and generated by the AHSS methodology of IDIADA) used for some of the scripts to read there their inputs
23	*data_generation.m*	OCTAVE	Octave script that loads the data from the *Methodology_input_process.xlsx* file and generates the following files: *Material.k, True_stress_strain_gauges_de_A, linear.k, power.k, tstrain.k*
24	*Inputs_rewrite.m*	OCTAVE	Octave script that loads the data from the *Methodology_input_process.xlsx* file and rewrites the Young modulus value at the files *Card_transform_E_ini.m* and

			w_shell_update_2_5mm.m and the thickness value at the files *properties.k*, *Session_tensile_OPCOM_w_shell_local.ses* and *Session_tensile_OPCOM_FADEXP_RegFactor_local_CM.ses*
25	*w_shell_update_2_5mm.m*	OCTAVE	Octave script that loads data from the files: *tstrain.k*, *linear.k*, *power.k* and updates the elasto-plastic curve for the new w value given by LSOPT at the *Material.k* file
26	*Card_transform_E_ini.m*	OCTAVE	Octave script that loads the data from the experimental curve of the file *True_stress_strain_gauges_de_A* to obtain the point of begginig of damage then copies from the optimal folder of the w_shell_OPCOM optimization stage the file *Material*.k and adds to it the LSDYNA cards used in the IDIADA methodology for the mesh optimization (e.g. *MAT_ADD_EROSION)
27	*mat_update_1mm.m*	OCTAVE	Octave script that updates the FADEXP and regulation factor for the mesh of 1mm for the values given by LSOPT at the *Material.k* file
28	*mat_update_2_5mm.m*	OCTAVE	Octave script that updates the FADEXP and regulation factor for the mesh of 2.5mm for the values given by LSOPT at the *Material.k* file
29	*mat_update_4mm.m*	OCTAVE	Octave script that updates the FADEXP and regulation factor for the mesh of 4mm for the values given by LSOPT at the *Material.k* file
30	*mat_update_6mm.m*	OCTAVE	Octave script that updates the FADEXP and regulation factor for the mesh of 6mm for the values given by LSOPT at the *Material.k* file
31	*mat_update_10mm.m*	OCTAVE	Octave script that load the value of FADEXP and Regulation factor generated by LSOPT and update the *Material.k* file for the 10mm mesh factor values and an estimation for the 20mm mesh factor values.
32	*simulation_end_lsdyna.m*	OCTAVE	Octave script that loads the history stored at the file *OPCOM_FADEXP_RegFactor_CM.ses.results*, truncates it to coincide with the experimental last strain value of the *True_stress_strain_gauges_de_A* file and save it as a csv file named *simulation_truncated*. If the experimental curve max strain value is larger than the simulation curve max strain value it saves all the simulation curve without truncating it
33	*mesh_results_1.m*	OCTAVE	Octave script that search at the 1mm_OPCOM stage of the main file the optimal folder and copies 4 files: *Material.k*, *nodout*, *secforc*,

			Session_tensile_OPCOM_FADEXP_RegFactor_local_CM.ses to the folder where it's launched
34	*mesh_results_2_5.m*	OCTAVE	Octave script that search at the 2.5mm_OPCOM stage of the main file the optimal folder and copies 4 files: *Material.k*, *nodout*, *secforc*, *Session_tensile_OPCOM_FADEXP_RegFactor_local_CM.ses* to the folder where it's launched
35	*mesh_results_4.m*	OCTAVE	Octave script that search at the 4mm_OPCOM stage of the main file the optimal folder and copies 4 files: *Material.k*, *nodout*, *secforc*, *Session_tensile_OPCOM_FADEXP_RegFactor_local_CM.ses* to the folder where it's launched
36	*mesh_results_6.m*	OCTAVE	Octave script that search at the 6mm_OPCOM stage of the main file the optimal folder and copies 4 files: *Material.k*, *nodout*, *secforc*, *Session_tensile_OPCOM_FADEXP_RegFactor_local_CM.ses* to the folder where it's launched
37	*mesh_results_10.m*	OCTAVE	Octave script that search at the 10mm_OPCOM stage of the main file the optimal folder and copies 4 files: *Material.k*, *nodout*, *secforc*, *Session_tensile_OPCOM_FADEXP_RegFactor_local_CM.ses* to the folder where it's launched
38	*Final_result_folder.m*	OCTAVE	Octave script that loads data from the *Methodology_input_process.xlsx* file and creates a new folder named as <<date_material name>> and saves there 3 files: *Material.k* (optimal card), *properties.k* and *Tensile_Test_4.key*

Table 6 - List of files generated by scripts present at the quasi-static model

Nº	File name	Type	Description
1	*Material.k*	LSDYNA	Ls-dyna include that contains the material information which changes through the different stages being it modified by different scripts of the methodology generated by the script *data_generation.m*
2	*True_stress_strain_gauges_de_A*	CSV	Comma separated values file that contains the information of the experimental curve used as comparative in the AHSS methodology generated by the script *data_generation.m*
3	*simulation_truncated*	CSV	Comma separated values file that contains the truncated simulation curve generated by the script *simulation_end_lsdyna.m*
4	*linear.k*	TEXT	Text file saved by the *data_generation.m* in column format that contains the range of cells AE15:AE45 of the excel *Methodology_input_process.xlsx* corresponding to the linear law
5	*power.k*	TEXT	Text file saved by the *data_generation.m* in column format that contains the range of cells AG15:AG45 of the excel *Methodology_input_process.xlsx* corresponding to the power law
6	*tstrain.k*	TEXT	Text file saved by the *data_generation.m* in column format that contains the range of cells AD15:AD45 of the excel *Methodology_input_process.xlsx* corresponding to the true strain values

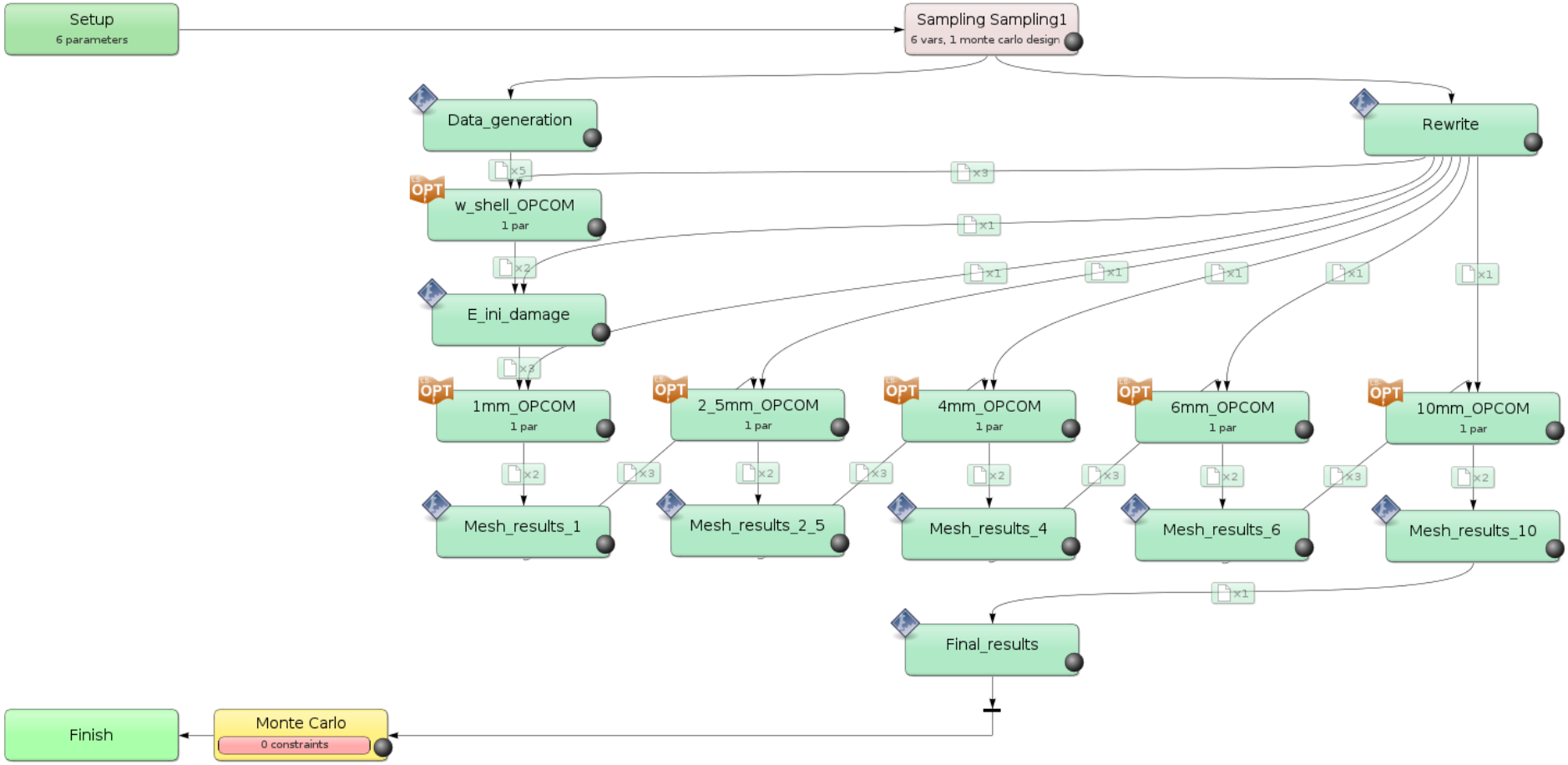

Figure 28 - Flowchart of LS-OPT main quasi-static model (FADEXP and Regulation Factor parameters). Source: Own

Table 7 - List of the inputs files, the files at the extra input files section and files from the File Transfer for each stage of the main quasi-static model

Nº	Stage	Input file	Extra input files	File transfer from stages above
1	Rewrite	*Inputs_rewrite.m*	*Methodology_input_process.xlsx* *properties.k* *w_shell_update_2_5mm.m* *Card_transform_E_ini.m* *Session_tensile_OPCOM_w_shell_local.ses* *Session_tensile_OPCOM_FADEXP_RegFactor_local_CM.ses*	-
2	Data_generation	*data_generation.m*	*Methodology_input_process.xlsx*	-
3	W_shell_OPCOM	*2_5_mm_w_shell.lsopt*	*Tensile_Test_2_5.key* *OPCOM_w_shell.ses* *OPCOM_w_shell.ses.results*	*linear.k* *power.k* *tstrain.k* *Material.k* *True_stress_strain_gauges_de_A* *properties.k* *Session_tensile_OPCOM_w_shell_local.ses* *w_shell_update_2_5mm.m*
4	E_ini_damage	*Card_transform_E_ini.m*	-	*properties.k* *True_stress_strain_gauges_de_A*
5	1mm_OPCOM	*1_mm_FADEXP_RegFactor_CM.lsopt*	*Tensile_Test_1.key* *mat_update_1mm.m* *OPCOM_FADEXP_RegFactor_CM.ses* *OPCOM_FADEXP_RegFactor_CM.ses.results* *simulation_end_lsdyna.m* *load_save_curve.ses* *load_save_curve.ses.results*	*properties.k* *True_stress_strain_gauges_de_A* *Material.k* *Session_tensile_OPCOM_FADEXP_RegFactor_local_CM.ses*
6	Mesh_results_1	*mesh_results_1.m*	*Tensile_Test_1.key*	*properties.k* *True_stress_strain_gauges_de_A*
7	2_5mm_OPCOM	*2_5_mm_FADEXP_RegFa*	*Tensile_Test_2_5.key*	*properties.k*

		ctor_CM.lsopt	*mat_update_2_5mm.m* *OPCOM_FADEXP_RegFactor_CM.ses* *OPCOM_FADEXP_RegFactor_CM.ses.results* *simulation_end_lsdyna.m* *load_save_curve.ses* *load_save_curve.ses.results*	*Material.k* *True_stress_strain_gauges_de_A* *Session_tensile_OPCOM_FADEXP_RegFactor_local_CM.ses*
8	Mesh_results_2_5	*mesh_results_2_5.m*	*Tensile_Test_2_5.key*	*properties.k* *True_stress_strain_gauges_de_A*
9	4mm_OPCOM	*4_mm_FADEXP_RegFactor_CM.lsopt*	*Tensile_Test_4.key* *mat_update_4mm.m* *OPCOM_FADEXP_RegFactor_CM.ses* *OPCOM_FADEXP_RegFactor_CM.ses.results* *simulation_end_lsdyna.m* *load_save_curve.ses* *load_save_curve.ses.results*	*properties.k* *Material.k* *True_stress_strain_gauges_de_A* *Session_tensile_OPCOM_FADEXP_RegFactor_local_CM.ses*
10	Mesh_results_4	*mesh_results_4.m*	*Tensile_Test_4.key*	*properties.k* *True_stress_strain_gauges_de_A*
11	6mm_OPCOM	*6_mm_FADEXP_RegFactor_CM.lsopt*	*Tensile_Test_6.key* *mat_update_6mm.m* *OPCOM_FADEXP_RegFactor_CM.ses* *OPCOM_FADEXP_RegFactor_CM.ses.results* *simulation_end_lsdyna.m* *load_save_curve.ses* *load_save_curve.ses.results*	*properties.k* *Material.k* *True_stress_strain_gauges_de_A* *Session_tensile_OPCOM_FADEXP_RegFactor_local_CM.ses*
12	Mesh_results_6	*mesh_results_6.m*	*Tensile_Test_6.key*	*properties.k* *True_stress_strain_gauges_de_A*
13	10mm_OPCOM	*10_mm_FADEXP_RegFactor_CM.lsopt*	*Tensile_Test_10.key* *mat_update_10mm.m* *OPCOM_FADEXP_RegFactor_CM.ses* *OPCOM_FADEXP_RegFactor_CM.ses.results* *simulation_end_lsdyna.m* *load_save_curve.ses*	*properties.k* *Material.k* *True_stress_strain_gauges_de_A* *Session_tensile_OPCOM_FADEXP_RegFactor_local_CM.ses*

			load_save_curve.ses.results	
14	Mesh_results_10	*mesh_results_10.m*	*Tensile_Test_10.key*	*properties.k* *True_stress_strain_gauges_de_A*
15	Final_results	*Final_result_folder.m*	*Methodology_input_process.xlsx* *Tensile_Test_4.key*	*properties.k*

6.1.2. Optimization stages

There is a total of 6 optimization stages (the lsopt type stages) which call other lsopt models when the main programme is running. Those secondary lsopt models gather the w parameter optimization and then all the mesh size parameters optimization, mesh by mesh.

All the optimization stages have the same internal structure less the post-process that is different in the first optimization stage, w parameter, than the others. The variables and the objective function changes between the optimizations.

Following sections explain the 4 main processes that happen at the optimization stages. For all the optimizations, at the set up stage the variables of that optimization are defined. In all cases the same sampling method is used: A polynomial meta-model of linear order with D-Optimal as the point selection algorithm.

For the 2_5_mm_w_shell_update there is only 1 variable to optimize: the w parameter that weights the linear and potential law. For the optimization of the different meshes, there are 2 optimization variables: the FADEXP and the RegFactor. In Figure 29 the w parameter optimization and the mesh parameters optimization secondary models are shown.

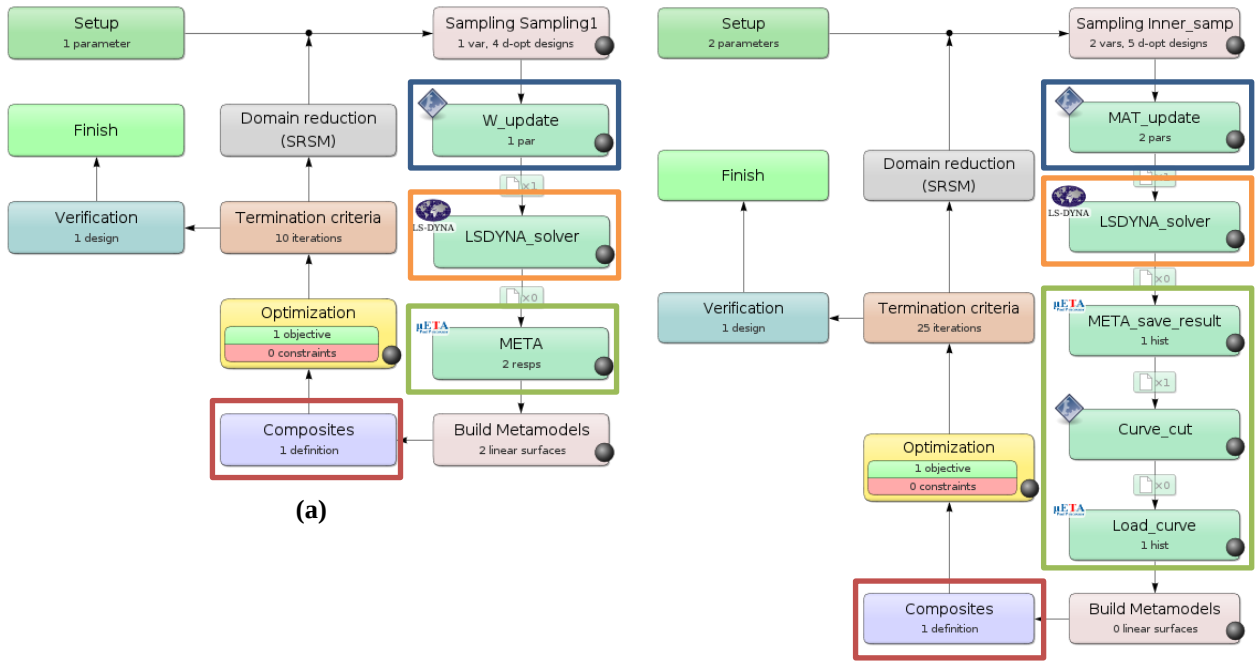

Figure 29 - At left side the lsopt file for the w parameter optimization and at the right size the lsopt file for the meshes optimization. In blue the Material update stage, in orange the Solver stage, in green the Post-Process stages and in red the composite stage for the w optimization and the meshes optimization. Source: Own

The optimization algorithm used in both cases is the hybrid adaptive simulated annealing (Hybrid ASA) which starts with the ASA algorithm to find an approximate global optimum after which leap-frog optimizer (LFOP) is used to sharpen the solution. The parameters used for the algorithms are the default by LS-OPT.

6.1.2.1. *Material update stage*

The material update stages are User-Defined stage of LS-OPT that call an Octave script that loads the parameter values generated by LS-OPT and rewrite the *Material.k* file with the new values.

The w optimization update script loads the data of the text files *tstrain.k*, *linear.k* and *power.k* and generates the true strain- true stress curve with the new w weight loaded from the LS-OPT sampling. Then the script rewrites the *Material.k* file.

The mesh update scripts rewrite the *Material.k* file changing the Fadexp factors and Regulation Factor of the *DEFINE_CURVE for their mesh and the higher ones. The optimized factors already obtained are left untouched. In Figure 30 the material update stage window for updating the variables at the mesh parameter secondary models is shown.

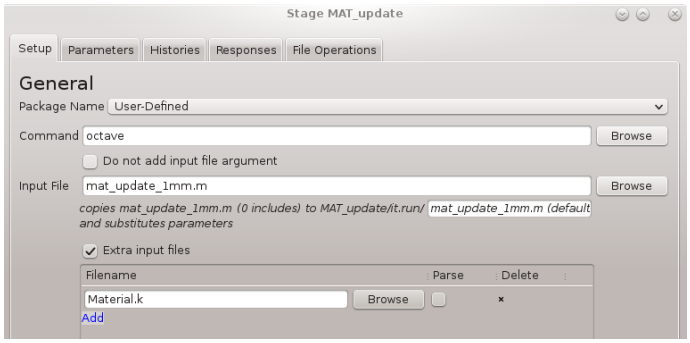

Figure 30 - Material update stage window used for the mesh optimizations (1mm mesh example). Source: Own

6.1.2.2. *Solver stage*

The solver stages are LS-DYNA stages of LS-OPT that run the input file of the LS-DYNA model. They also load at the working folder generated by LS-OPT the files needed by the META stage to perform the post-process there. Figure 31 shows the solver stage window filled.

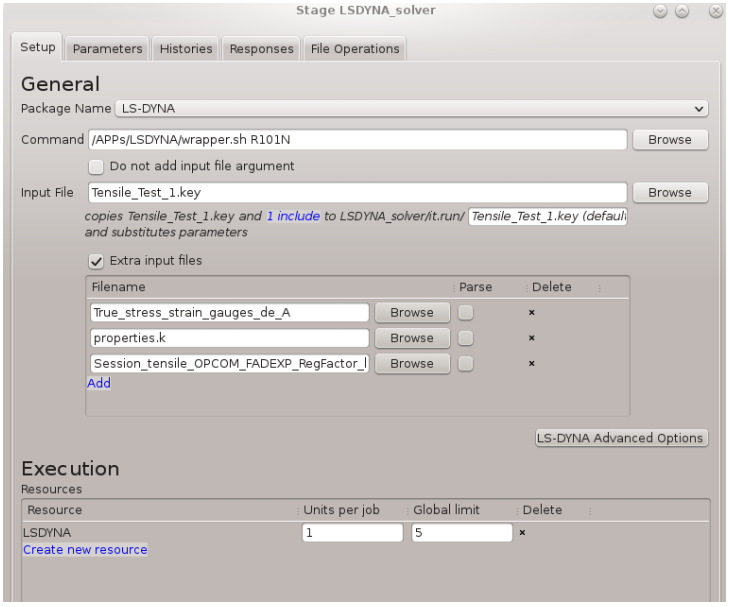

Figure 31 - Solver stage window used for the mesh optimizations (1mm mesh example). Source: Own

The calculations of LS-DYNA are made locally. The current version of the methodology uses the version R10.1 SMP (shared memory parallel) of LS-DYNA. With this version, all the sampling calculations at one iteration can be calculated simultaneously.

6.1.2.3. Post-process stages

The post-process stages are the ones differing more between the w parameter optimization and the Fadexp and RegFactor parameters optimizations.

For the w parameter optimization only one META stage of LS-OPT is used to call the *OPCOM_w_shell.ses* session that is run at the solver stage folder generated by LS-OPT. This session calls at the same time the *Session_tensile_OPCOM_w_shell_local.ses* which creates 2 annotations (one for the experimental curve and another for the simulated curve) at the strain where there is the maximum true stress in the experimental curve. These annotations are later used by the Composite stage to create the objective function of the optimization. Figure 32 shows the post-process stage window for the w optimization parameter.

For the mesh optimizations, the post-process is done with 3 stages: 1 META stage of LS-OPT that saves the results of the simulation; a User-defined stage of LS-OPT that execute the script to cut the simulation curve to not exceed the experimental last strain; and another META stage of LS-OPT to load the truncated curve created by the previous script to the LS-OPT variables (a history in this case) to use it at the composite stage.

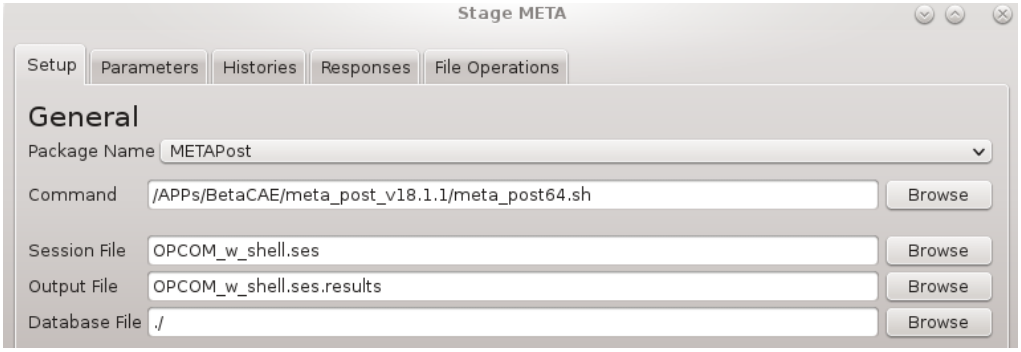

Figure 32 - Post-process stage window used for the w optimization parameter. Source: Own

6.1.2.4. Composite stage

The composite stage of LS-OPT is used to create environmental variables from the already created environmental variables (responses, variables to optimize, etc…) or to operate histories with the curve matching techniques of LS-OPT.

The optimization stage for the w parameter defines an expression at the composite stage. The expression is the absolute value of the rest between the responses of the experimental curve and the simulated curve. Figure 33 shows the composite stage window.

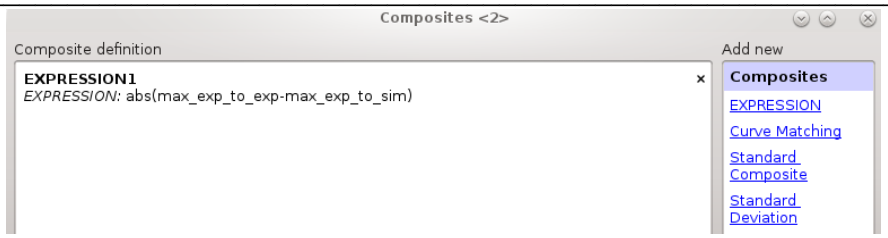

Figure 33 - Composite stage window for the w optimization stage. Source: Own

The mesh optimization stage uses the curve mapping (size of area between curves) as a curve matching technique between the history generated on the simulation truncated with the script and the experimental curve. The regression points are defined as 200 fixed equidistant points. Figure 34 shows the curve matching composite stage used.

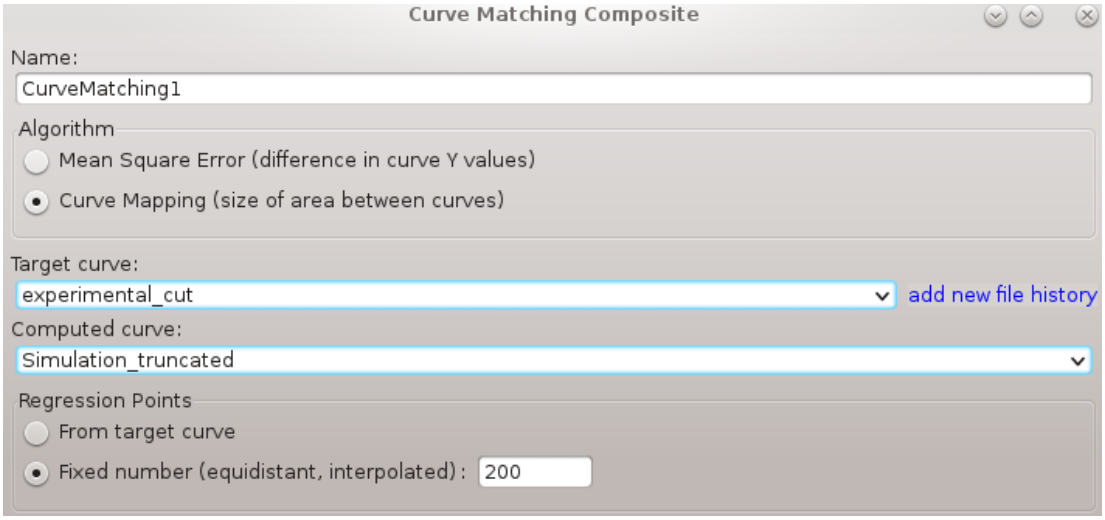

Figure 34 - Composite stage window for the meshes optimization. Source: Own

6.1.3. Automation of processes

In order to provide a methodology where the user needs to make as fewer changes as possible, 4 processes have been automatized by scripts in Octave. The user will change the excel file of the methodology introducing there all the inputs needed and then the lsopt main file will be calling the scripts in the different stages to the proper make modifications and changes to link the different optimization stages of the whole model. Figure 35 shows the structure of the main model with the automations done highlighted.

The following sections explain the processes automation to link the different optimization stages. First processes are the generation of new data used along the running of the main file of lsopt and the rewriting of values at the scripts to use depending of the material itself (thickness, Young modulus, etc…). Then the adaptation of the material card used to obtain the w optimum parameter to the material card used in the mesh optimizations. Finally, after each mesh optimization one script to transfer the material card to the next optimization with the optimum values of the previous optimization.

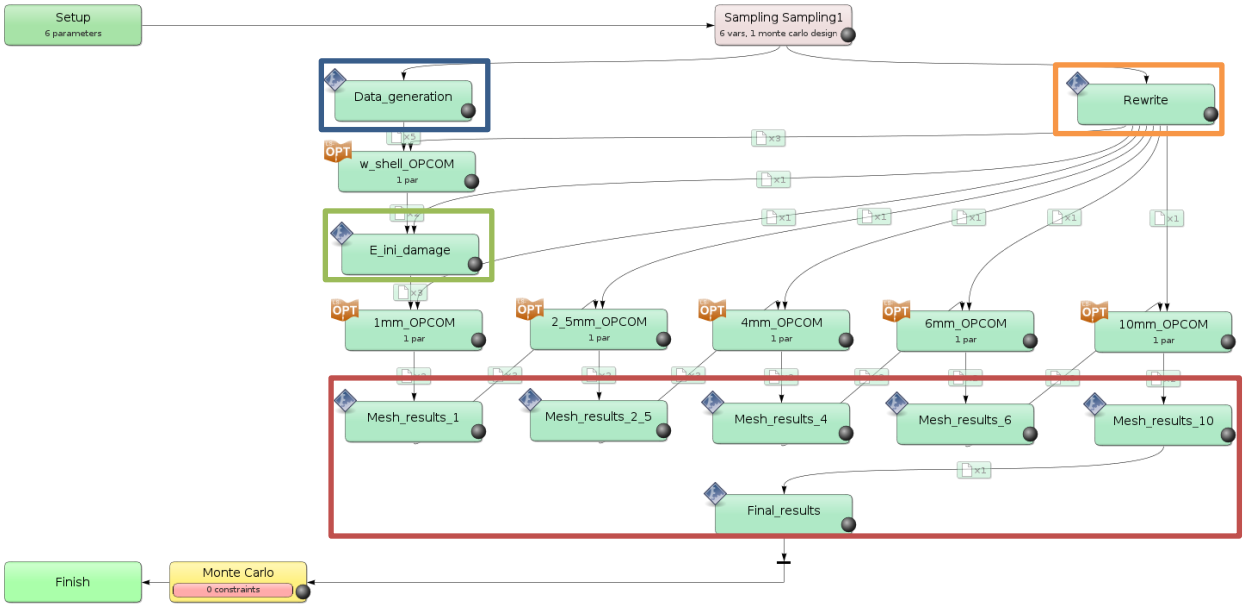

Figure 35 - In blue the Data generation process, in orange the rewrite process, in green the adaptation of the material card from the w optimization to the meshes optimization and in red the transfer of results from the meshes optimizations. Source: Own

6.1.3.1. Data generation process

The data generation process automation consists in the creation of the files used at the following stages that are dependant of the inputs. The inputs are all introduced in the excel file of the methodology and then read by the script *data_generation.m*. This script creates different text files necessaries for the subsequent stages.

After preparing the excel file, the *data_generation.m* script extracts from the excel file the information about the:

- True strain used at the linear and power laws
- Stresses of the linear law
- Stresses of the power law
- Young modulus
- Material name
- Density value
- Poisson value
- Experimental curve data

Then the script writes five text files:

- *tstrain.k*
- *linear.k*
- *power.k*
- *Material.k*
- *True_stress_strain_gauges_de_A*

The text files *tstrain.k*, *linear.k* and *power.k* are used at the material update stage of the w_shell_OPCOM optimization stage. The *Material.k* file generated by the *data_generation.m*

script is the template file that is also used at the material update stage of the w optimization. The *True_stress_strain_gauges_de_A* file has the experimental curve data and is used in all the optimization stages.

6.1.3.2. Rewrite process

The rewrite process automation consists in the update of the values of the scripts used at the methodology that depend of the inputs introduced at the excel file.

The *Inputs_rewrite.m* script extracts from the excel file the information about:

- Young modulus
- Thickness

Then the script loads the files to be updated and changes the values of the Young modulus and thickness. Then it overwrites the files with the new values stored. The files that are changed are:

- *properties.k* (change thickness)
- *w_shell_update_2_5mm.m* (change E value)
- *Card_transform_E_ini.m* (change E value)
- *Session_tensile_OPCOM_w_shell_local.ses* (change thickness)
- *Session_tensile_OPCOM_FADEXP_RegFactor_local_CM.ses* (change thickness)

The overwritten files are then transferred to the correspondent folder by the lsopt's function File transfer which move files from one stage to another after the stage has run.

6.1.3.3. E_ini_damage stage

The E_ini_damage_stage process automation consists in the linking between the w parameter optimization and the optimization of the factors for the Fadexp and the Regulation Factor. The linking consists of 2 steps: first the localization and copy of the optimal *Material*.k file of the w_shell_OPCOM stage to the working folder and then the addition to the *Material.k* file of the parts needed for the next optimizations (e.g. *MAT_ADD_EROSION).

First, the script *Card_transform_e_ini.m* navigates through the folders generated by LS_OPT to find the optimal one and copy the *Material.k* file from there to the current working folder. Then, the script loads the experimental curve data and calculates the true strain equivalent to the experimental strain that has the maximum experimental stress. This strain is used as a factor of one of the curves used at the *MAT_ADD_EROSION. Finally, the same script loads the *Material.k* file data and add the new lines corresponding to the *MAT_ADD_EROSION card of LS-DYNA and the curves used in it.

6.1.3.4. Results from mesh optimizations process

The results from mesh optimizations process automation consists of transferring the results from one mesh optimization to the next one i.e. copying the *Material.k* file of the optimal iteration to the next mesh optimization stage.

The *mesh_results_x.m* script copy searches for the "x" mesh optimization optimal folder and copies the *Material.k* file in there to the current working directory. Then using the "File transfer" function of ls-opt it is transferred to the next mesh optimization folder generated by LS-OPT. This way the optimal values of the parameters FADEXP and RegFactor obtained at one optimization step are transferred to the next optimization step. Therefore, when the 10mm mesh optimization ends, the *Material.k* file already has all the optimal values obtained during the whole process.

6.2. Strain-Rate model definition

The strain-rate model is a continuation of the quasi-static model. It needs the results obtained from the previous model to work. Once the quasi-static state is calibrated this model is used to make the material card strain-rate dependent. For each mesh the model calculate the optimal factor of the LCSRS curve of the MAT_ADD_EROSION card. In Figure 36, the stage structure defined at LS-OPT for the main file on the strain-rate methodology can be seen.

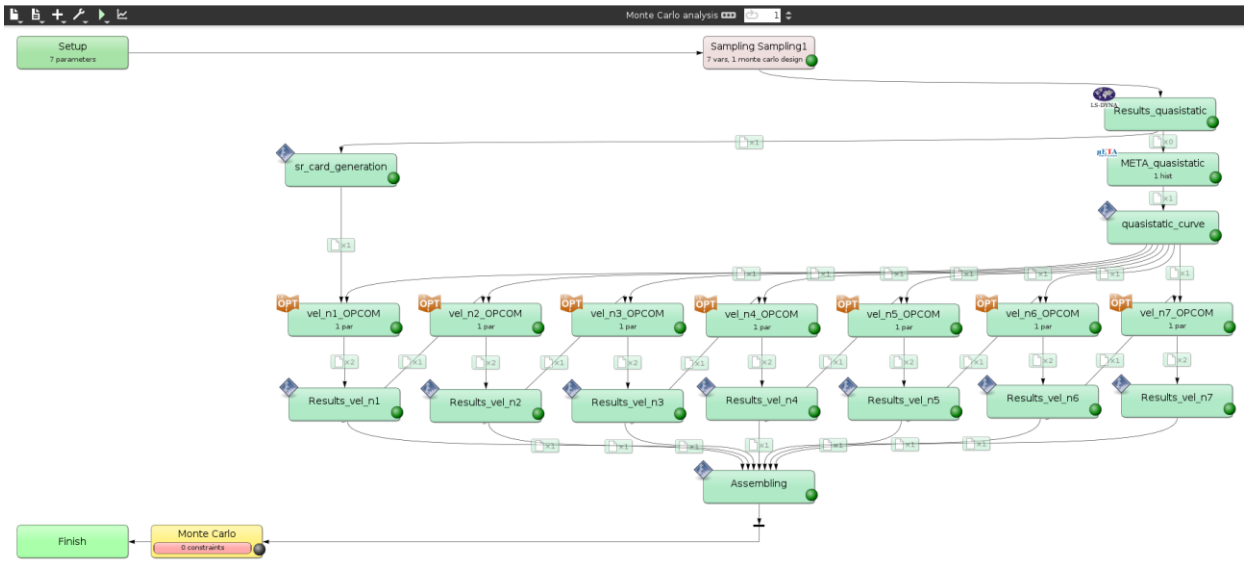

Figure 36 - LS-OPT Strain-Rate model. Source: Own

The main file of the strain-rate model is the *SR_MAT_7.lsopt*. The "7" refers to the number of velocities that will be considered. For different number of velocities there is the corresponding model already created.

For a new strain-rate characterization is necessary to have the results of applying the quasi-static model. Therefore, the quality of the final material card generated is highly dependent of the quasi-static calibration.

The Excel file of the methodology needs to be changed and is faster to use the modified one of the quasi-static model and add there the new parts needed. All the other files of the model are copied directly to a new working folder. While running there is a series of scripts that will generate new files or modify the existing ones.

6.2.1. Model structure

The model consists in a large quantity of files (scripts, LSOPT files, META sessions, LSDYNA files, etc...) and the main lsopt file calls other lsopt files which perform the different optimization steps. The whole model uses the 4mm mesh size specimen (FEM model) for the calibration of the strain-rate parameters. In Table 8 and Table 9 there is a brief summary of all the files involved in the model.

In Figure 37, the stage structure defined at LS-OPT for the main lsopt file *SR_MAT_7.lsopt* can be seen. A total of 20 stages are defined in the main model: 11 of them are user-defined stages that launch octave scripts, other 7 are lsopt stages that launch other lsopt files and there is 2 stages used to post-process the inputs from the quasi-static model. This means that in total 7 optimization process are done with this methodology (smaller models have been created for cases where less velocities are being calibrated).

In Table 10 there is a list of the files that are used as input for each stage and the Extra input files needed. There is also a column for the files that are transferred to each stage from stages above them. For the case of an lsopt stage to work, all the files that the inner level will use need to be added at the extra input files section of the stage.

Table 8 - List of files of the strain-rate model (7 velocities example)

Nº	File name	Type	Description
1	*SR_MAT_7_vel.lsopt*	LSOPT	Main lsopt file which is opened with LSOPT
2	*4_mm_SFO_vel_n1.lsopt*	LSOPT	Lsopt file that defines the optimization step for the 1st velocity
3	*4_mm_SFO_vel_n2.lsopt*	LSOPT	Lsopt file that defines the optimization step for the 2nd velocity
4	*4_mm_SFO_vel_n3.lsopt*	LSOPT	Lsopt file that defines the optimization step for the 3th velocity
5	*4_mm_SFO_vel_n4.lsopt*	LSOPT	Lsopt file that defines the optimization step for the 4th velocity
6	*4_mm_SFO_vel_n5.lsopt*	LSOPT	Lsopt file that defines the optimization step for the 5th velocity
7	*4_mm_SFO_vel_n6.lsopt*	LSOPT	Lsopt file that defines the optimization step for the 6th velocity
8	*4_mm_SFO_vel_n7.lsopt*	LSOPT	Lsopt file that defines the optimization step for the 7th velocity
9	*Tensile_Test_4.key*	LSDYNA	Main Ls-dyna file for the 4 mm mesh. Contains the heading, nodes, elements, sets, cross section and boundaries It has 2 includes: *Material.k* and *properties.k*
10	*Session_tensile_OPCOM_quasi-static_local.ses*	META	Main Meta session for the post process for the results of the quasi-static stage.
11	*OPCOM_quasi-static.ses*	META	Meta session with the Optimizer Setup of META configuration for the quasi-static stage. It calls the session *Session_tensile_OPCOM_quasi-static_local.ses* It defines 1 history named “Quasi-static_eng”
12	*OPCOM_quasi-static.ses.results*	META	Meta file with the format needed by the Optimizer Setup that will store the results configured at the file *OPCOM_quasi-static.ses*
13	*Session_tensile_OPCOM_SR_local.ses*	META	Main Meta session for the post process of the results for the velocity optimization stages. Includes the annotations that will be read by the Optimizer Setup
14	*OPCOM_SR_PD.ses*	META	Meta session with the Optimizer Setup of META configuration for the velocities optimization stages. It calls the session *Session_tensile_OPCOM_SR_local.ses* It defines 2 responses (from 2 annotations made on the post-process) named “integral_quasi-static” and “integral_sr”
15	*OPCOM_SR_PD.ses.results*	META	Meta file with the format needed by the Optimizer Setup that will store the results configured at the file *OPCOM_SR_PD.ses*

16	*Methodology_input_process_SR.xlsx*	EXCEL	Excel file with all the inputs (Defined by the user and generated by the AHSS methodology of IDIADA) used for some of the scripts to read there their inputs
17	*data_generation_SR.m*	OCTAVE	Octave script that loads the data from the *Methodology_input_process_SR.xlsx* file and generates the following files : *Material_sr.k, True_stress_strain_gauges_de_A, properties.k, mat_update_SR_vel_nx.m*, results_vel_nx.m** * It is automatized the creation of the scripts depending of the number of velocities defined at the excel file *Methodology_input_process_SR.xlsx*
18	*Inputs_rewrite_SR.m*	OCTAVE	Octave script that loads the data from the *Methodology_input_process_SR.xlsx* file and rewrites the thickness value at the files *Session_tensile_OPCOM_quasi-static_local.ses* and *Session_tensile_OPCOM_SR_local.ses*
19	*quasi-static_curve_generation.m*	OCTAVE	Octave script that loads the data from the results of the simulation of the quasi-static results stage, from the file *OPCOM_quasi-static.ses.results*, to generate the *quasi-static_curve* file which is a csv file with the quasi-static curve stored
20	*Results_assembling.m*	OCTAVE	Octave script that loads data from the *Methodology_input_process.xlsx* file and gathers the information of the Results_vel_nx* stages to generate the final material card *Material.k* that is stored at a new created folder named as <<date_material name>> * It is automatized the loading from the Results_vel_nx stages (x from 1 to the number of velocities) depending of the number of velocities defined at the excel file *Methodology_input_process_SR.xlsx*

Table 9 - List of files generated by scripts present at the strain-rate model (7 velocities example)

Nº	File name	Type	Description
1	*Material.k*	LSDYNA	Ls-dyna include that contains the material information which changes through the different stages being it modified by different scripts of the methodology generated by the script *data_generation_SR.m*
2	*properties.k*	LSDYNA	Ls-dyna include that contains the part and section shell of the elements (thickness of the shell is defined here) generated by the script *data_generation_SR.m*
3	*True_stress_strain_gauges_de_A*	CSV	Comma separated values file that contains the information of the experimental curve used as comparative in Results_quasi-static stage generated by the script *data_generation_SR.m*
4	*Quasi-static_curve*	CSV	Comma separated values file that contains the quasi-static simulation curve generated by the script *quasi-static_curve_generation.m*
5	*mat_update_SR_vel_n1.m*	OCTAVE	Octave script generated by by the script *data_generation_SR.m* that updates the SFO parameter of the curve with ID 1002 corresponding to the 1st velocity at the *Material.k* file
6	*mat_update_SR_vel_n2.m*	OCTAVE	Octave script generated by by the script *data_generation_SR.m* that updates the SFO parameter of the curve with ID 1003 corresponding to the 2nd velocity at the *Material.k* file
7	*mat_update_SR_vel_n3.m*	OCTAVE	Octave script generated by by the script *data_generation_SR.m* that updates the SFO parameter of the curve with ID 1004 corresponding to the 3th velocity at the *Material.k* file
8	*mat_update_SR_vel_n4.m*	OCTAVE	Octave script generated by by the script *data_generation_SR.m* that updates the SFO parameter of the curve with ID 1005 corresponding to the 4th velocity at the *Material.k* file
9	*mat_update_SR_vel_n5.m*	OCTAVE	Octave script generated by by the script *data_generation_SR.m* that updates the SFO parameter of the curve with ID 1006 corresponding to the 5th velocity at the *Material.k* file
10	*mat_update_SR_vel_n6.m*	OCTAVE	Octave script generated by by the script *data_generation_SR.m* that updates the SFO parameter of the curve with ID 1007 corresponding to the 6th velocity at the *Material.k* file

11	*mat_update_SR_vel_n7.m*	OCTAVE	Octave script generated by by the script *data_generation_SR.m* that updates the SFO parameter of the curve with ID 1008 corresponding to the 7th velocity at the *Material.k* file
12	*results_vel_n1.m*	OCTAVE	Octave script generated by by the script *data_generation_SR.m* that search at the vel_n1_OPCOM stage of the main file the optimal folder and copies 4 files: *Material.k*, *nodout*, *secforc*, *Session_tensile_OPCOM_SR_local.ses* to the folder where it's launched
13	*results_vel_n2.m*	OCTAVE	Octave script generated by by the script *data_generation_SR.m* that search at the vel_n2_OPCOM stage of the main file the optimal folder and copies 4 files: *Material.k*, *nodout*, *secforc*, *Session_tensile_OPCOM_SR_local.ses* to the folder where it's launched
14	*results_vel_n3.m*	OCTAVE	Octave script generated by by the script *data_generation_SR.m* that search at the vel_n3_OPCOM stage of the main file the optimal folder and copies 4 files: *Material.k*, *nodout*, *secforc*, *Session_tensile_OPCOM_SR_local.ses* to the folder where it's launched
15	*results_vel_n4.m*	OCTAVE	Octave script generated by by the script *data_generation_SR.m* that search at the vel_n4_OPCOM stage of the main file the optimal folder and copies 4 files: *Material.k*, *nodout*, *secforc*, *Session_tensile_OPCOM_SR_local.ses* to the folder where it's launched
16	*results_vel_n5.m*	OCTAVE	Octave script generated by by the script *data_generation_SR.m* that search at the vel_n5_OPCOM stage of the main file the optimal folder and copies 4 files: *Material.k*, *nodout*, *secforc*, *Session_tensile_OPCOM_SR_local.ses* to the folder where it's launched
17	*results_vel_n6.m*	OCTAVE	Octave script generated by by the script *data_generation_SR.m* that search at the vel_n6_OPCOM stage of the main file the optimal folder and copies 4 files: *Material.k*, *nodout*, *secforc*, *Session_tensile_OPCOM_SR_local.ses* to the folder where it's launched
18	*results_vel_n7.m*	OCTAVE	Octave script generated by by the script *data_generation_SR.m* that search at the vel_n7_OPCOM stage of the main file the optimal folder and copies 4 files: *Material.k*, *nodout*, *secforc*, *Session_tensile_OPCOM_SR_local.ses* to the folder where it's launched

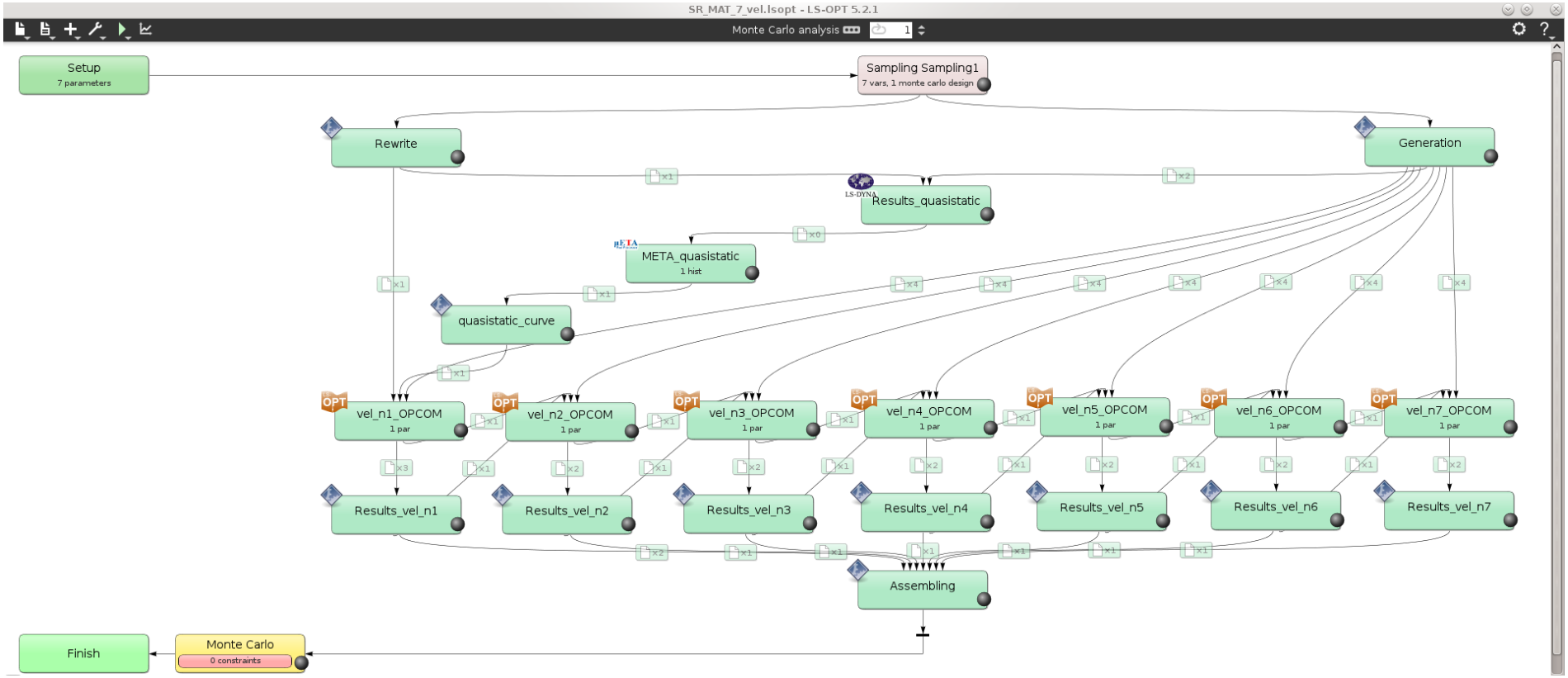

Figure 37 - Flowchart of LS-OPT main SR model. Source: Own

Table 10 - List of the inputs files, the files at the extra input files section and files from the File Transfer for each stage of the main strain-rate model

Nº	Stage	Input file	Extra input files	File transfer from stages above
1	Rewrite	*Inputs_rewrite_SR.m*	*Methodology_input_process_SR.xlsx* *Session_tensile_OPCOM_quasi-static_local.ses* *Session_tensile_OPCOM_SR_local.ses*	-
2	Generation	*data_generation_SR.m*	*Methodology_input_process_SR.xlsx* *Material.k*	-
3	Results_quasi-static	*Tensile_Test_4.key*	*Material.k*	*True_stress_strain_gauges_de_A properties.k* *Session_tensile_OPCOM_quasi-static_local.ses*
4	META_quasi-static	-	*OPCOM_quasi-static.ses* *OPCOM_quasi-static.ses.results*	-
5	quasi-static_curve	*quasi-static_curve_generation.m*	-	*OPCOM_quasi-static.ses.results*
6	vel_n1_OPCOM	*4_mm_SFO_vel_n1.lsopt*	*Tensile_Test_4.key* *OPCOM_SR_PD.ses* *OPCOM_SR_PD.ses.results*	*Session_tensile_OPCOM_SR_local.ses* *quasi-static_curve* *Material_sr.k* *properties.k* *mat_update_SR_vel_n1.m* *results_vel_n1.m*
7	Results_vel_n1	*results_vel_n1.m*	-	*quasi-static_curve* *Material_sr.k* *results_vel_n1.m*
8	vel_n2_OPCOM	*4_mm_SFO_vel_n2.lsopt*	*Tensile_Test_4.key* *OPCOM_SR_PD.ses* *OPCOM_SR_PD.ses.results*	*Session_tensile_OPCOM_SR_local.ses* *quasi-static_curve* *Material_sr.k* *properties.k* *mat_update_SR_vel_n2.m*

				results_vel_n2.m
9	Results_vel_n2	*results_vel_n2.m*	-	*quasi-static_curve* *results_vel_n2.m*
10	vel_n3_OPCOM	*4_mm_SFO_vel_n3.lsopt*	*Tensile_Test_4.key* *OPCOM_SR_PD.ses* *OPCOM_SR_PD.ses.results*	*Session_tensile_OPCOM_SR_local.ses* *quasi-static_curve* *Material_sr.k* *properties.k* *mat_update_SR_vel_n3.m* *results_vel_n3.m*
11	Results_vel_n3	*results_vel_n3.m*	-	*quasi-static_curve* *results_vel_n3.m*
12	vel_n4_OPCOM	*4_mm_SFO_vel_n4.lsopt*	*Tensile_Test_4.key* *OPCOM_SR_PD.ses* *OPCOM_SR_PD.ses.results*	*Session_tensile_OPCOM_SR_local.ses* *quasi-static_curve* *Material_sr.k* *properties.k* *mat_update_SR_vel_n4.m* *results_vel_n4.m*
13	Results_vel_n4	*results_vel_n4.m*	-	*quasi-static_curve* *results_vel_n4.m*
14	vel_n5_OPCOM	*4_mm_SFO_vel_n5.lsopt*	*Tensile_Test_4.key* *OPCOM_SR_PD.ses* *OPCOM_SR_PD.ses.results*	*Session_tensile_OPCOM_SR_local.ses* *quasi-static_curve* *Material_sr.k* *properties.k* *mat_update_SR_vel_n5.m* *results_vel_n5.m*
15	Results_vel_n5	*results_vel_n5.m*	-	*quasi-static_curve* *results_vel_n5.m*

16	vel_n6_OPCOM	*4_mm_SFO_vel_n6.lsopt*	*Tensile_Test_4.key* *OPCOM_SR_PD.ses* *OPCOM_SR_PD.ses.results*	*Session_tensile_OPCOM_SR_local.ses* *quasi-static_curve* *Material_sr.k* *properties.k* *mat_update_SR_vel_n6.m* *results_vel_n6.m*
17	Results_vel_n6	*results_vel_n6.m*	-	*quasi-static_curve* *results_vel_n6.m*
18	vel_n7_OPCOM	*4_mm_SFO_vel_n7.lsopt*	*Tensile_Test_4.key* *OPCOM_SR_PD.ses* *OPCOM_SR_PD.ses.results*	*Session_tensile_OPCOM_SR_local.ses* *quasi-static_curve* *Material_sr.k* *properties.k* *mat_update_SR_vel_n7.m* *results_vel_n7.m*
19	Results_vel_n7	*results_vel_n7.m*	-	*quasi-static_curve* *results_vel_n7.m*
20	Assembling	*Results_assembling.m*	*Methodology_input_process_SR.xlsx*	*Material_vel1.k* *Material_sr.k* *Material_vel2.k* *Material_vel3.k* *Material_vel4.k* *Material_vel5.k* *Material_vel6.k* *Material_vel7.k*

6.2.2. Optimization stages

There are 7 optimization stages (the lsopt type stages) which call other lsopt models when the main programme is running.

All the optimization stages have the same internal structure but the variables and the objective function changes between them. In Figure 38, one of the secondary lsopt models is shown.

Following sections explain the 4 main processes that happen at the optimization stages, same processes as for the quasi-static model. For all the optimizations, at the set up stage the variables of that optimization are defined. In all cases the same sampling method is used: A polynomial meta-model of linear order with D-Optimal as the point selection algorithm.

There is only one variable to optimize at every stage: the SFO parameter that is a factor of the strain-stress curve for that velocity.

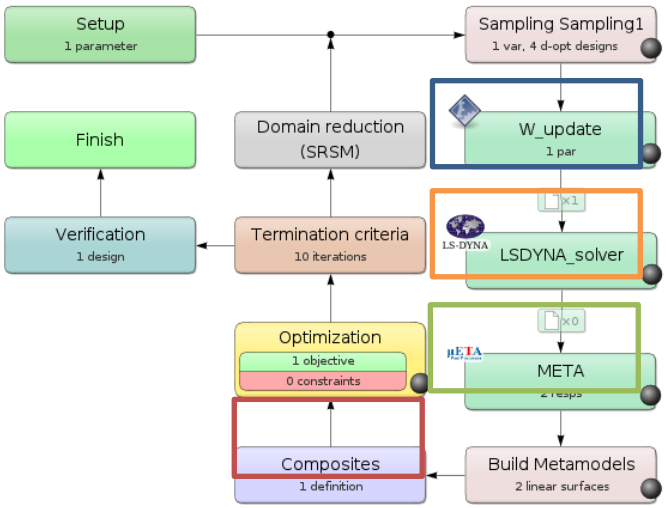

Figure 38 - In blue the Material update stage, in orange the Solver stage, in green the Post-Process stages and in red the composite stage for the strain-rate optimization for one velocity. Source: Own

The optimization algorithm used in both cases is the hybrid adaptive simulated annealing (Hybrid ASA) which starts with the ASA algorithm to find an approximate global optimum after which leap-frog optimizer (LFOP) is used to sharpen the solution. The parameters used for the algorithms are the default by LS-OPT.

6.2.2.1. Material update stage

The material update stages are User-Defined stage of LS-OPT that calls an Octave script that loads the parameter values generated by LS-OPT and rewrite the *Material_sr.k* file with the new values and save it with a new name: *Material.k*.

The *mat_update_SR_vel_nx.m* script loads the data of the *Material_sr.k* and changes the LCSS id curve to match it with the one corresponding to the velocity being optimized and updates the SFO parameter with the value loaded from the LS-OPT sampling. Then the script rewrites the *Material_sr.k* file and changes its name to *Material.k*. In Figure 39, the material update stage is shown.

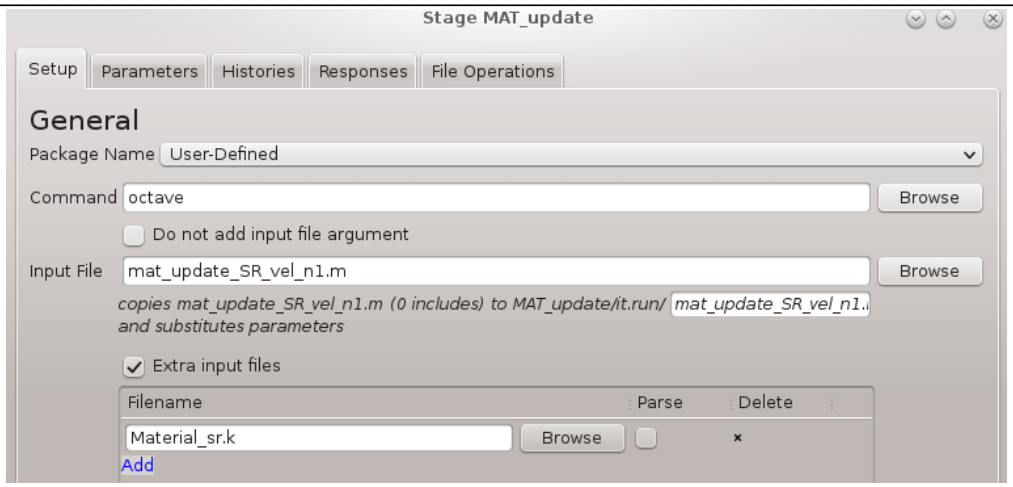

Figure 39 - Material update stage window used for the velocity optimizations (velocity nº 7 example). Source: Own

6.2.2.2. Solver stage

The solver stages are LS-DYNA stages of LS-OPT that run the input file of the LS-DYNA model. They also load in the working folder generated by LS-OPT the files needed by the META stage to perform the post-process there. In Figure 40, the solver stage is shown.

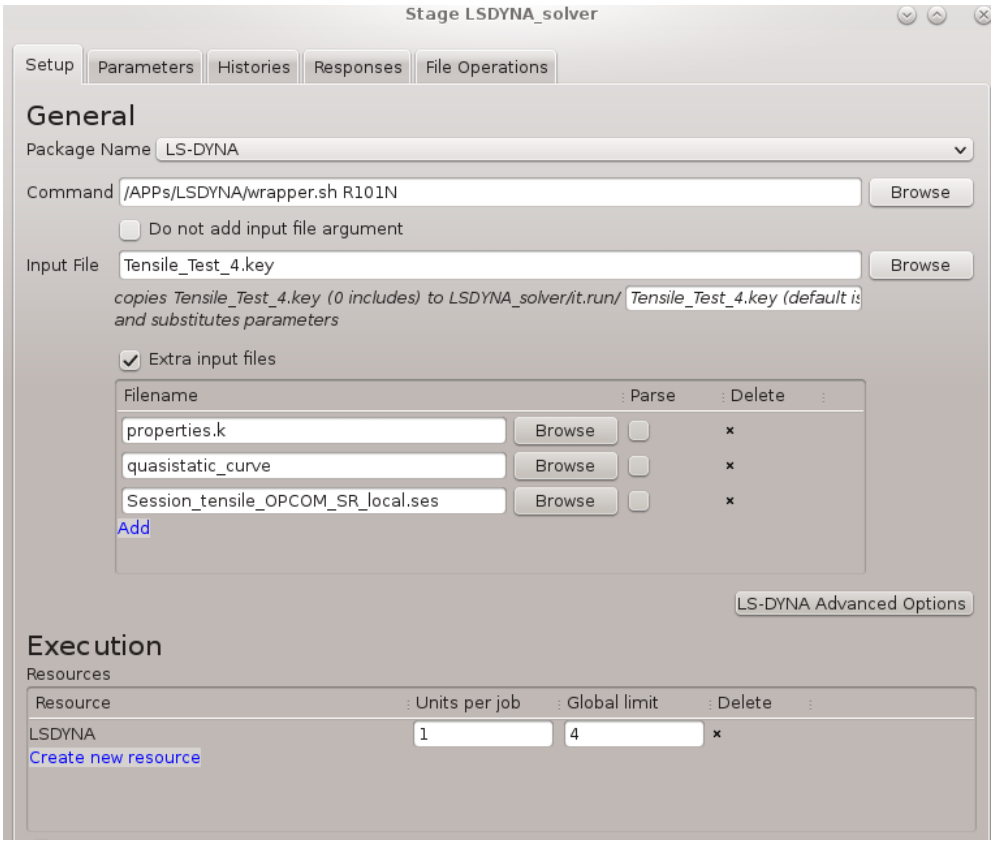

Figure 40 - Solver stage window used for the velocity optimizations (velocity nº 7 example). Source: Own

The calculations of LS-DYNA are made locally. The current version of the methodology uses the version R10.1 SMP (shared memory parallel) of LS-DYNA. With this version, all the sampling calculations for one iteration can be calculated simultaneously.

6.2.2.3. *Post-process stage*

One META stage of LS-OPT is used to call the *OPCOM_SR_PD.ses* session that is run at the solver stage folder generated by LS-OPT. This session calls at the same time the *Session_tensile_OPCOM_SR_local.ses* which creates 2 annotations (one for the quasi-static curve and another for the simulated curve) of the area of the curves represented in engineering strain-stress. These annotations are later used by the Composite stage to create the objective function of the optimization. In Figure 41, the post-process stage is shown.

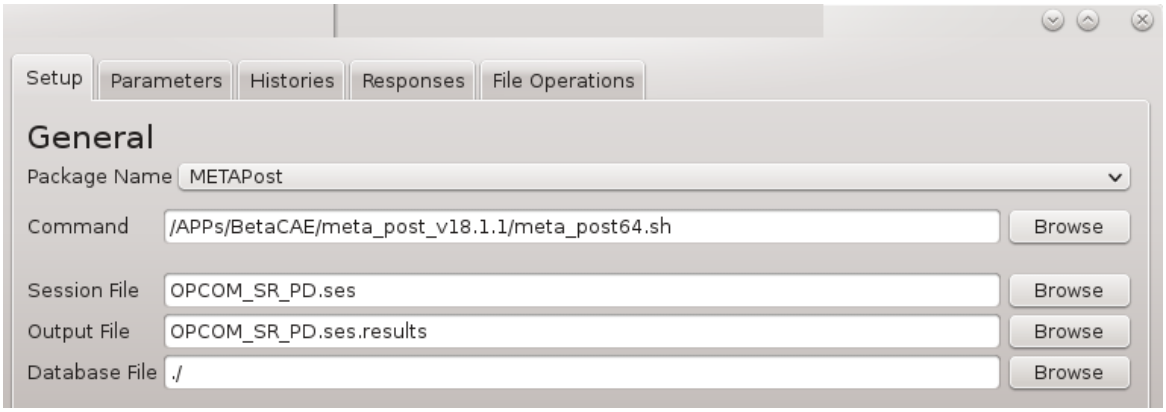

Figure 41 - Post-process stage window used for the velocity optimization (velocity nº 7 example). Source: Own

6.2.2.4. *Composite stage*

The composite stage of LS-OPT is used to create environmental variables from the already created environmental variables (responses, variables to optimize, etc…) or to operate histories with the curve matching techniques of LS-OPT.

An expression at the composite stage is used. The expression is the absolute value of the rest between the responses of the simulated curve and the quasi-static curve. Figure 42 shows the composite stage window for the strain-rate model.

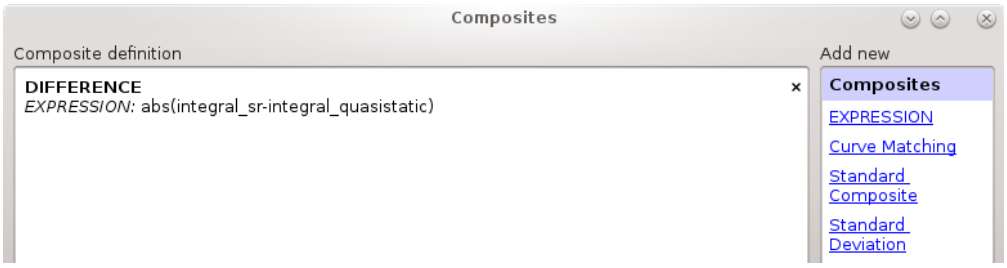

Figure 42 - Composite stage window for the velocity optimization. Source: Own

6.2.3. Automation of processes

In order to provide a methodology where the user needs to make as few changes as possible, 4 processes have been automatized by scripts in Octave. The user will change the excel file of the methodology introducing there all the inputs needed. The results from the quasi-static model are also used as inputs of the strain-rate model. Then the lsopt main file will be calling the scripts in the different stages to make the proper modifications and changes to link the different optimization stages of the whole model.

The following sections explain the processes automation to link the optimizations. First processes are the generation of new data used along the running of the main file of lsopt and the rewriting of the values in the scripts that depend on the material itself (thickness, Young modulus, etc…). Then the linking between the quasi-static model and the strain-rate model is done. Finally, the assembling of all the results obtained into one unique material card is done. Figure 43 shows the structure of the main model or the strain-rate optimization with the automations done highlighted.

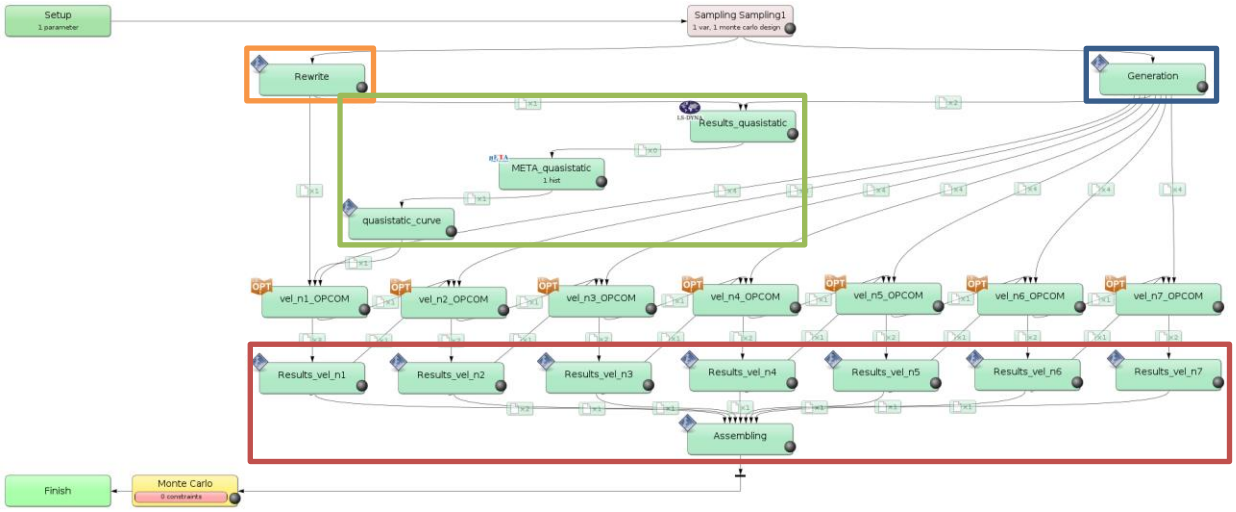

Figure 43 - In blue the Data generation process, in orange the rewrite process, in green the link between the quasi-static model and the strain-rate model process and in red the assembling of results process. Source: Own

6.2.3.1. Data generation process

The data generation process automation consists in the creation of the files used in the following stages that are dependant of the inputs. The inputs are all introduced in the excel file of the methodology and then read by the script *data_generation_SR.m*. This script creates different text files necessaries for the subsequent stages.

After preparing the excel file, the *data_generation_SR.m* script extracts from the excel file and from the *Material.k* file obtained at the quasi-static model the information about the:

- Young modulus
- Thickness
- Experimental curve data
- c and e0 parameters for the strain-rate calculation
- Velocities to be studied

Then the script writes 3 files:

- *properties.k* (LS-DYNA file)
- *Material_sr.k* (LS-DYNA file)
- *True_stress_strain_gauges_de_A* (text file)

Finally, the script creates the scripts needed for the updating material stage and for the results of the optimization stages, the 2 scripts for all the velocities studied *mat_update_SR_vel_x.m* and *results_vel_nx.m* (depending of the number of velocities present in the excel file the number of scripts generated changes accordingly).

The *Material_sr.k* file generated by the *data_generation_sr.m* script is the template file that is used at all the material update stages of the velocities optimizations. The *True_stress_strain_gauges_de_A* file has the experimental curve data and is used in the models linking process. The *properties.k* is used at all the LS-DYNA calculations done. The *mat_update_SR_vel_x.m* and *results_vel_nx.m* scripts are used at the corresponding optimization stage.

The generated files are then transferred to the correspondent folder by the lsopt's function File transfer which move files from one stage to another after the stage has run.

6.2.3.2. Rewrite process

The rewrite process automation consists in the update of the values of the scripts used in the methodology that depend of the inputs introduced in the excel file.

The *Inputs_rewrite_SR.m* script extracts from the excel file the information about:

- Thickness

Then the script loads the files to be updated and change the values of the thickness. Then it overwrites the files with the new values stored. The files that are changed are:

- *Session_tensile_OPCOM_quasi-static_local.ses*
- *Session_tensile_OPCOM_SR_local.ses*

The overwritten files are then transferred to the correspondent folder by the lsopt's function "File transfer" which move files from one stage to another after the stage has run.

6.2.3.3. Models linking process

The models linking process consists in the connexion between the quasi-static model, which must be launched before the strain-rate model, and the strain-rate model. The link is done by 3 stages: Results_quasi-static, META_quasi-static and quasi-static curve.

The Results_quasi-static stage is a LS-DYNA stage of LS-OPT that runs the input file of the LS-DYNA model of 4mm mesh size with the *Material.k* file obtained from the quasi-static model. In Figure 44, the Results_quaisstatic stage is shown.

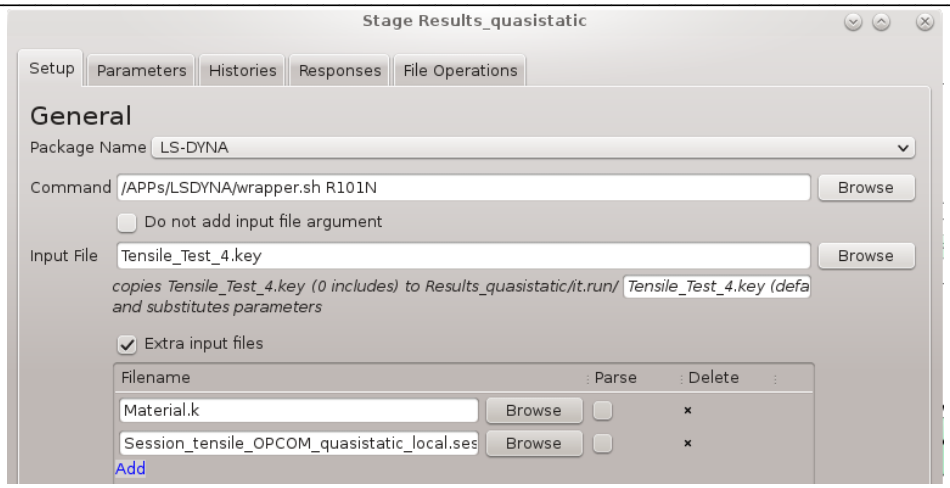

Figure 44 - Results_quasi-static stage window used at first step of the models linking process. Source: Own

The META_quasi-static stage is a META stage of LS-OPT that it is used to call the *OPCOM_quasi-static.ses* session that is run at the Results_quasi-static stage folder generated by LS-OPT. This session calls at the same time the *Session_tensile_OPCOM_quasi-static_local.ses* session that loads the results from the calculation of the 4mm mesh size with the optimal material card of the quasi-static model. The *OPCOM_quasi-static.ses* session generates a history of the simulation curve that is then used at the third stage of the models linking process. In Figure 45, the META_quasi-static stage is shown.

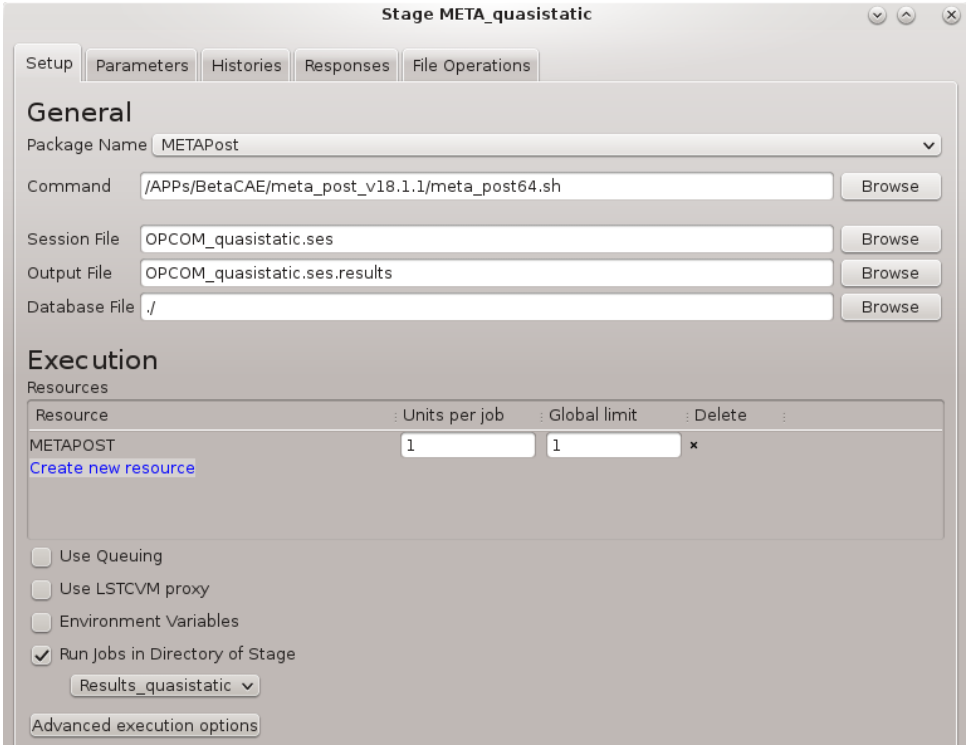

Figure 45 - META_quasi-static stage window used for the models linking process. Source: own

The quasi-static_curve stage is a User-Defined stage of LS-OPT that calls an Octave script that loads the history generated at the previous stage and saves it in the correct format by the name *quasi-static_curve*. (Same format as the one used for the experimental curve at the quasi-static model). This file is then used in all the optimization stages as the "experimental" curve. In Figure 46, the quasi-static_curve stage is shown.

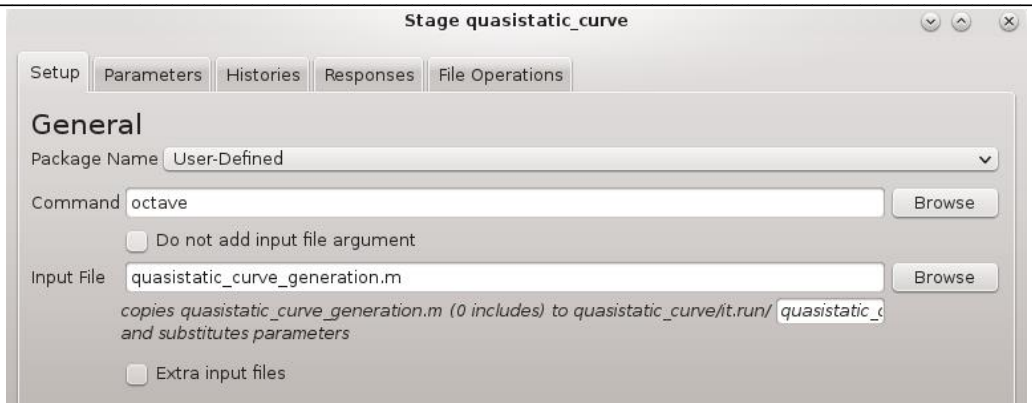

Figure 46 - Quasi-static_curve stage window used for the models linking process. Source: own

6.2.3.4. Assembling process

The assembling process consists of storing the results obtained in the velocity optimizations to join them all at the last stages in order to create a unique material card. Each *results_vel_nx.m* copies from the optimal folder of the velocity optimization the files: *Material.k*, *nodout*, *secforc* and *Session_tensile_OPCOM_SR_local.ses* to the working folder for the x velocity. Then using the lsopt's function "File Transfer" the *Material.k* file is moved to the folder generated by the Assembling stage changing its name to *Material_velx.k* where "x" is the number of the velocity being optimized.

As last step, the Assembling stage calls the *Results_assembling.m script*. This script reads from the excel file of the methodology the number of velocities and then creates the final *Material.k* file that has all the curves generated by the strain-rate model and the SFO factors for each curve.

7. Results

In this chapter, results obtained applying the improved methodology developed in this thesis are shown for a quasi-static correlation and for strain-rate. Finally, a time and cost comparison is shown between the old and new methodology.

Previously to the introduction of optimization techniques to the methodology, the strain rate was not being calculated manually for any material due to the large quantity of parameters to calibrate. Therefore, only for the quasi-static test there is previous material calibration data done with the old methodology status. The current IDIADA clients' requests for strain-rate dependent steel material cards are created using the tool developed in this thesis but there are no previous calibrations done.

In the following subchapters, the curves from both methodologies are compared for the quasi-static correlation, the results for the strain-rate dependent card are shown and, at the end, an economical and time comparison is done between both approaches.

7.1. Quasi-static correlation

The material being compared in the quasi-static correlation is a DP890 steel (Double Phase) which was used during the creation of the old methodology status at [55]. The results for the manual calibration refers to the results obtained using the old methodology at 2018 where most parameters in the material card where manually calibrated by an engineer.

For the previous methodology or manual material card calibration presented, the w parameter for extending the plastic curve after necking was obtained from a regression curve created with the experimental data of different grade steels available at that moment (year 2018). The material damage effects where introduced at that time changing the slope of the elasto-plastic curve after the necking point but always keeping the slope positive, i.e. as extreme case the slope for the plastic true strain true stress beyond necking was set almost horizontal, in order to ensure plastic convergence. The LS-DYNA model was set up using the results of a solid detailed simulation (0.5mm mesh in necking zone) with the extended elasto-plastic curve. This simulation was done for each new material to calibrate and the duration was more than 8h.

At Figure 47 and Figure 48 the results for the old methodology (with manual parameter calibration) and the LSOPT outputs are shown:

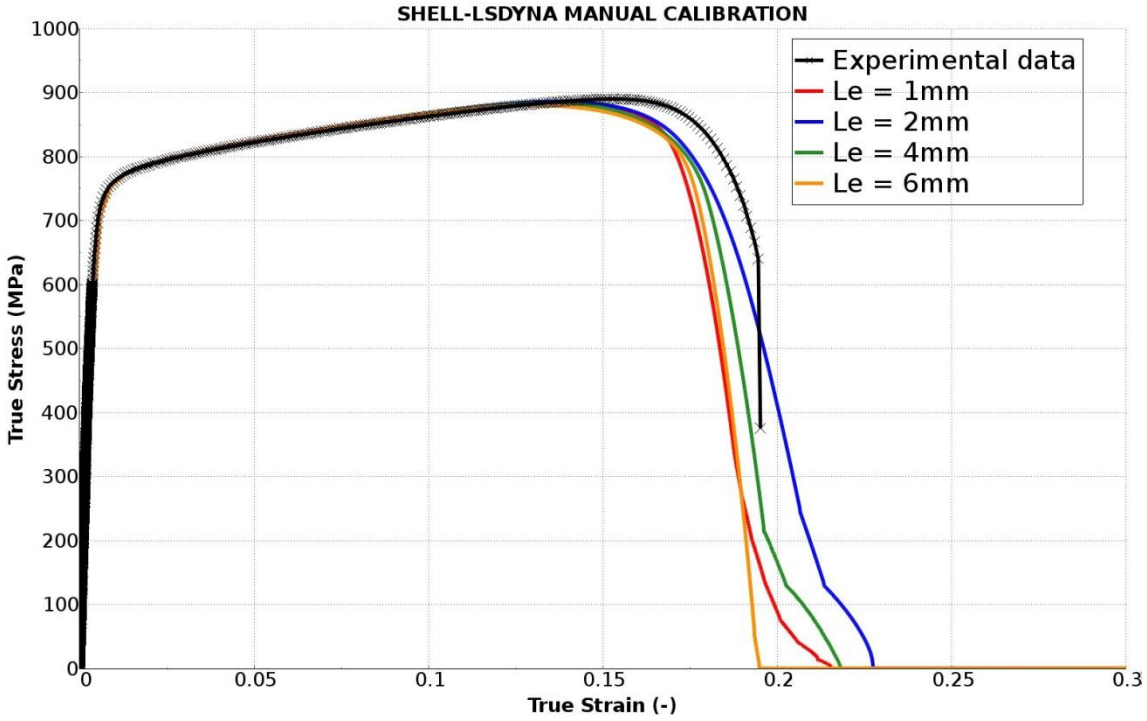

Figure 47 - Manual calibration curves for the element length range [1-6] mm. Source: Own

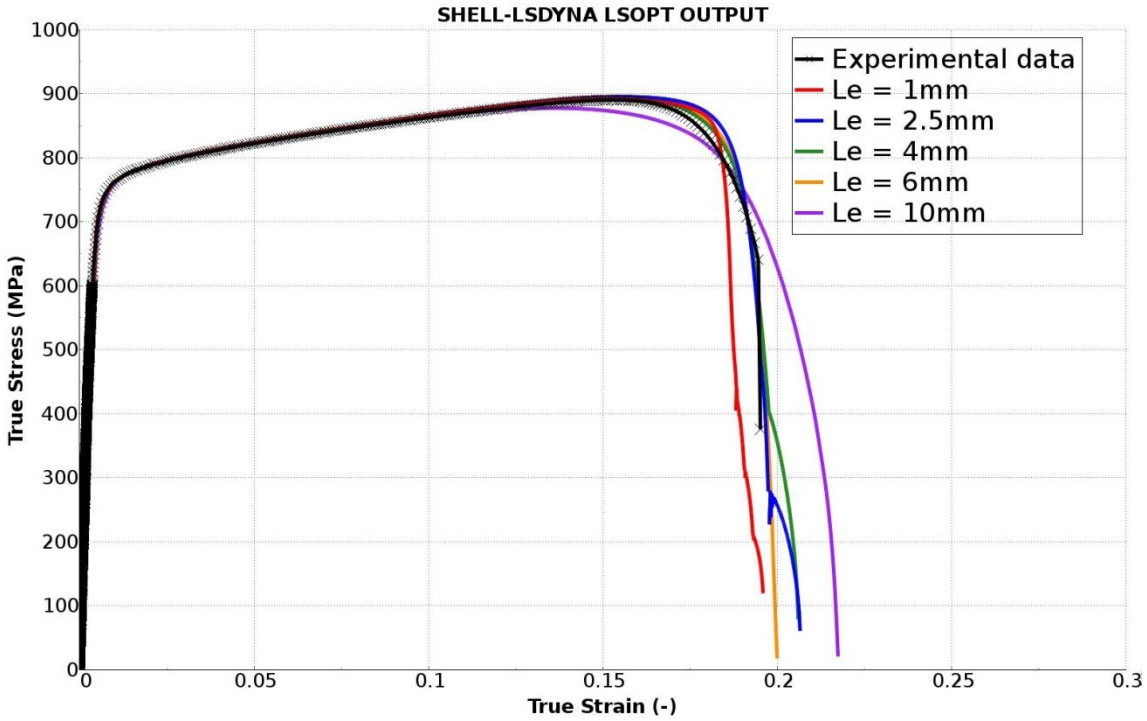

Figure 48 - LSOPT raw output curves for the element length range [1-10] mm. Source: Own

The status of the old methodology was unable to capture precisely the material degradation due to the damage effects. In addition, the calibration criterion used at that time was to have the failure in similar strains than the tensile test instead of capturing better the shape of the experimental test but having the ductile failure at higher strains (conservative approach).

For the LSOPT raw outputs, the behaviour for the element lengths of 2.5, 4 and 6mm is much better. The 1mm and 10mm curves have a different curvature but still the 1mm behaviour is improved comparing to the old methodology. If the simulation is compared to the experimental data, there is a small overestimation after the experimental true stress maximum. This degree of deviation respect to the experimental data does not have significant effects on a quasi-static or crash component or full-vehicle simulation where other factors induce more noise.

For the current status of the LSOPT tool developed in this thesis, the outputs obtained from the software can be further improved manually for a better calibration. The effect of the FADEXP and RegFactor is coupled which leads to different pairs of values for this variables that gives as output, curves that pass near the experimental point before catastrophic failure but have different curvatures. Moreover, the point selection algorithm, the optimization algorithm and the curve matching technique used in the current tool status are defined using the defaults by LS-OPT. A more efficient definition for these techniques could lead to more precise direct output curves. But, the study of their influence in the methodology was out of the scope of this project. In Chapter 9, the improvements on these topics are commented at the Future work section to increase the robustness of the tool.

For the current default options defined, a local minimum locking has been observed. Part of this issue is due to the huge range defined for all the variables in the first optimization run. Hybrid ASA may change from the ASA algorithm to the leap-frog optimizer (LFOP) near a local optimum instead the global optimum. The huge range allowed to the variables and the coupling between the FADEXP and RegFactor provides an environment where to find local minimum locking is common.

However, the output from LS-OPT gives us one pair of acceptable values for FADEXP and RegFactor. Manually studying the effect of changing the FADEXP and RegFactor one can find a different pair that has similar behaviour but the curvature fits better.

To maintain a similar behaviour but with different curvature, increasing the RegFactor should be compensated reducing the FADEXP value and vice versa. Doing a quick scope for the 1mm mesh and then the others is possible to define a narrower range for the variables to optimize. Running again the LSOPT model with these smaller new ranges gives as output the curves from Figure 49.

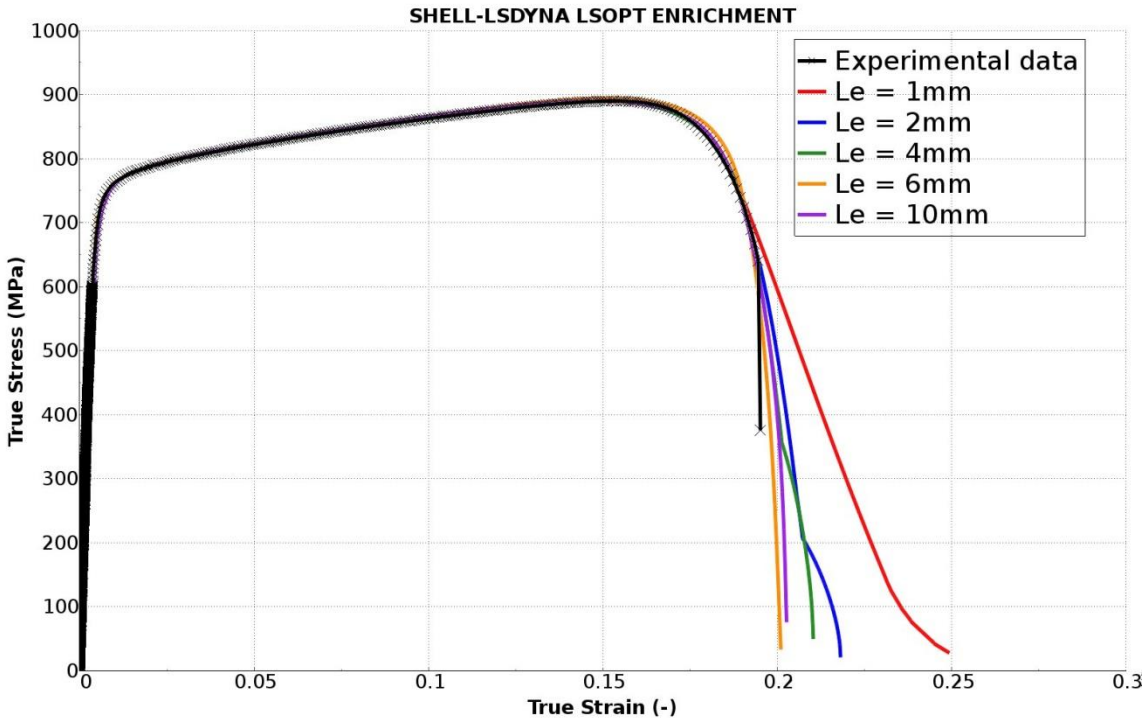

Figure 49 - LSOPT output enriched curves for the element length range [1-10] mm. Source: Own

Now the curve fitting is even better than the first LSOPT run which already was better than the old methodology approach.

7.2. Strain-Rate tests

The current strain rate approach is based in using the Jonhson Cook model parameters as base to scale the elasto-plastic curve for the strain rate and simulate a uniaxial tensile test where the strain rate is uniformly distributed during all the duration of the test. The real behaviour of the test is more complex than this, because for the strain rate test of 1 s^{-1} when the necking starts, the strain rate in the necking zone increase, due to the non-uniform behaviour of the necking zone, while outside the necking zone is still 1 s^{-1}.

The LS-OPT model calibrate the parameters in an scenario of uniformly distribution of strain-rate in the tensile test specimen (the strain-rate dependency is still not defined during the calibration) for each velocity and then with the final material card that assembles all the parameters it should be able to represent the real behaviour in simulation.

While this thesis was developed, the strain-date data obtained from the experimental facilities were highly noise and only the Johnson Cook parameters were used. Validation of this approach was unable to be done during the thesis time duration for lack of time and clean test data. At that time, there were not models already created to simulate the strain rate test.

The validation of the strain rate methodology is one of the future steps to be done. However, the material cards with the strain-rate definition have been already applied in some projects involving dynamic simulation (see chapter 8).

Despite this inability to simulate the real strain rate test curve correlation, the LSOPT's optimization stages for the strain rate model are plotted at Figure 50. The material studied is a Transformation-induced plasticity aided banitic ferrite (TBF), a third generation AHSS steels (see Figure 5). More specifically it is a TBF1000.

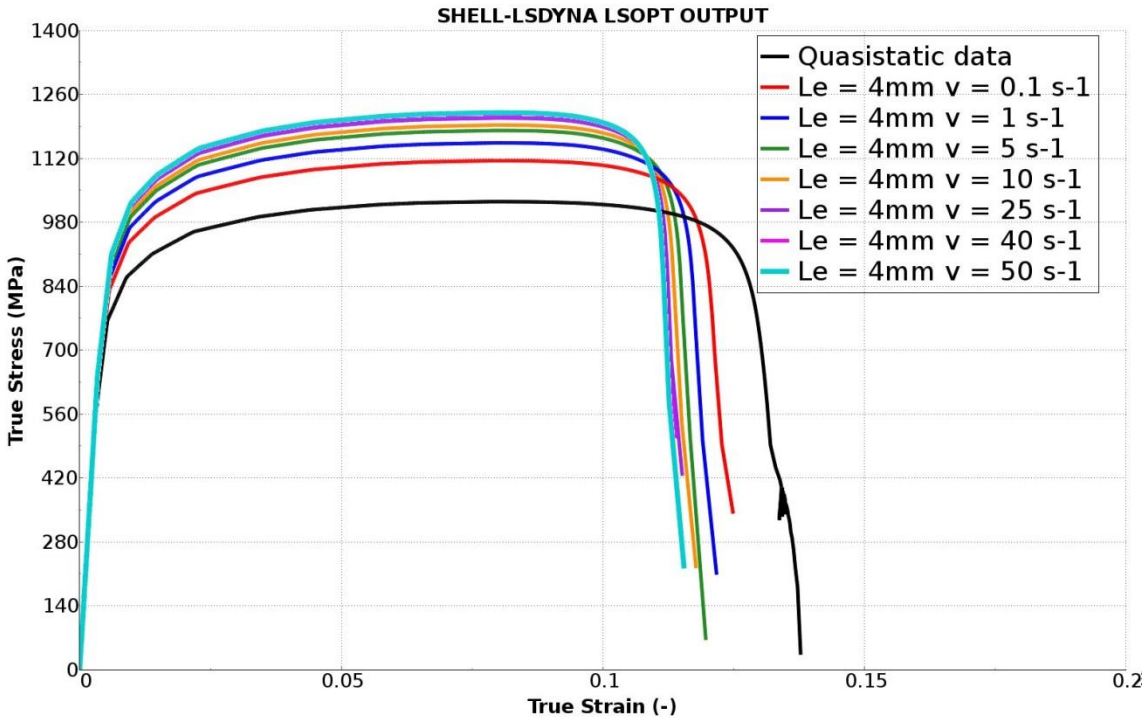

Figure 50 – LSOPT output for a strain –rate correlation of 7 different velocities. Source: Own

The curves plotted represent the behaviour that would have a tensile strain rate test if the strain rate was uniformly distributed along the whole specimen during all the duration of the test. The stiffer response expected with the velocity increasing is seen.

With this approach, using the assembled material card with the entire elasto-plastic curve scaled for the different strain-rates and with the parameters calibrated the behaviour of simulating the strain rate test should be captured by this material card.

7.3. Cost comparison

The objectives of this thesis were aimed to increase efficiency the previous investigation in AHSS done by IDIADA, in order to apply it in productive projects. Therefore, time needed to create the material card and costs of it are of crucial importance for this matter.

At Figure 51 the comparison in time is shown between the old methodology and the proposed approach applying the LSOPT tool developed in this thesis. The comparison is done in working days, i.e. the days since the work is started that will be need to deliver the generated material card. The data corresponds to real projects where the old and new methodologies have been applied.

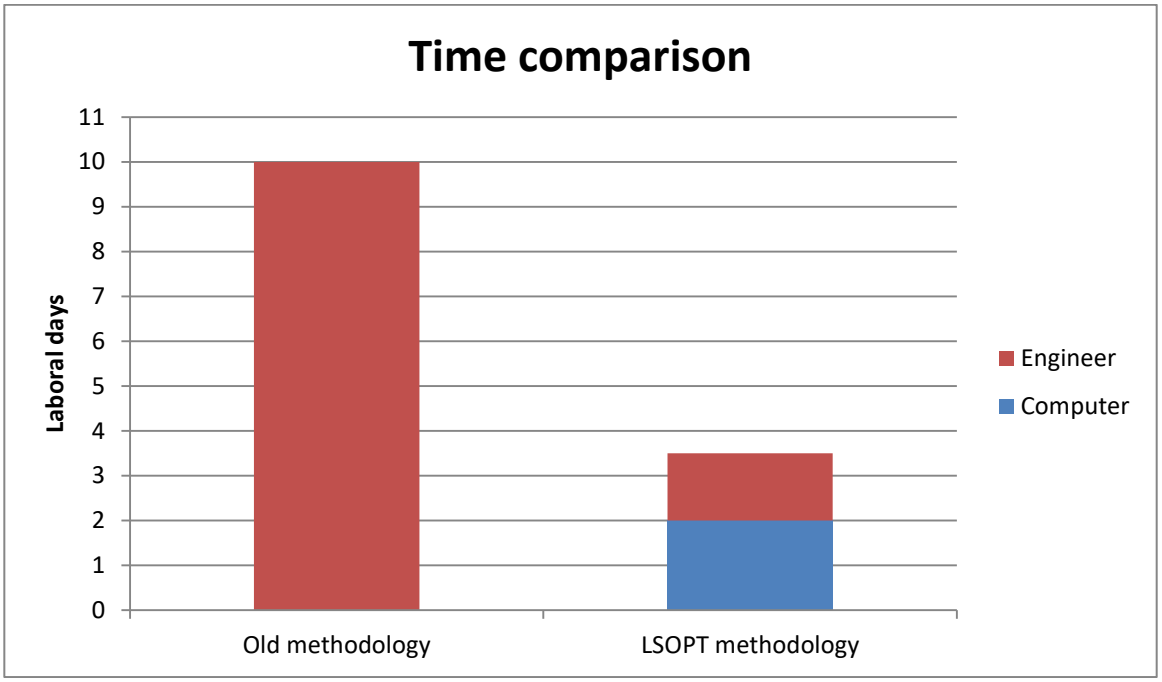

Figure 51 – Time comparison between both methodologies with data from already done projects. Source: Own

The old methodology needs the engineer to work on it during all the duration. The time every simulation last is not big enough to free the engineer for some hours in order to work in other tasks. Therefore, during 10 days, the engineer only works in the creation of the material card.

Meanwhile, the new LSOPT tool allows that the engineer, once the model is set up and running, to work in other projects until the finalization of the first run. Then it is need to manually search for the narrower ranges of the variables. After these new ranges are introduced to the LSOPT model it will free again the engineer to work in other tasks. Therefore, during the 3 days and half that now is needed to create the material card 2 of them the engineer can be working in parallel in other projects.

The time needed to create a new steel material card, mesh independent, including damage and strain-rate dependency has been reduced approximately 2/3 of the initial time duration. Also, letting the LSOPT calculations run during non-labour hours maximize the efficiency of the tool.

In Table 11 there is broken down the list of sub-activities during the tensile test calibration with a risk value assigned. More risk means that is more possible to encounter problems or to need extra time than planned. The time assigned to each activity was the needed to calibrate the material used for the creation of the methodology (DP890).

In Table 12 there is listed the workflow that the methodology follows with a risk value also assigned that shows the steps with more risk for the creation of the material car in the time planned.

Table 11 – List of activities and sub-activities broken down for the current status methodology feedback at applied projects with risk assigned

List of activities	Card parameter calibration	Description	Tool	Risk (1-5)	Why	Time cost (h)
TESILE TEST CALIBRATION	Elasto-plastic curve	IDIADA approach to define the Young modulus, the yield stress and the fitting of the experimental curve to 30 points	Excel	1	IT describing the steps and no calculations are done	0.5
	Elasto-plastic extended curve	IDIADA analytical approach to obtain elasto-plastic extended curve from the tensile test 50mm Gaugue measurements (optimization w parameter)	LSOPT	1	Only needs to be run 1 time	1.75
	FADEXP and RegFactor for 1mm element length	Calibration of GISSMO (Fadexp & RegFactor) parameters for the element length of 1mm	LSOPT	3	Methodology gets trapped in local minimum. High time cost	1.25
	FADEXP and RegFactor for 2.5mm element length	Calibration of GISSMO (Fadexp & RegFactor) parameters for the element length of 2.5mm	LSOPT	2	Methodology gets trapped in local minimum. ,Medium time cost	0.33
	FADEXP and RegFactor for 4mm element length	Calibration of GISSMO (Fadexp & RegFactor) parameters for the element length of 4mm	LSOPT	2	Methodology gets trapped in local minimum. Medium time cost	0.5
	FADEXP and RegFactor for 6mm element length	Calibration of GISSMO (Fadexp & RegFactor) parameters for the element length of 6mm	LSOPT	2	Methodology gets trapped in local minimum. Medium time cost	0.5
	FADEXP and RegFactor for 10mm element length	Calibration of GISSMO (Fadexp & RegFactor) parameters for the element length of 10mm	LSOPT	2	Methodology gets trapped in local minimum. Very low time cost	0.5

Table 12 – Methodology work flow with detailed time description for engineer and CPU hours with risk assigned

Methodology procedure	Description	Work	Risk (1-5)	Why	Engineer time (h)	PC time (h)
Excel preparation	Fill the excel with the experimental data	Engineer	1	Defined steps	0.5	
Tensile test calibration with w optimization	Set up the model and run it	PC	3	Is expected not the best correlation	0.5	5
Manual sensitivity analysis	Change manually and run simulations	Engineer	4	Can consume a lot of hours	5	
Tensile test calibration without w and with narrower variable ranges	Set up the new ranges en run it	PC	2	Once the ranges are well defined usually works at 1st attempt	0.1	3.25
				Total	6.1	8.25

8. Application on productive projects

Since the LSOPT tool developed in this thesis was finished it has been applied in several productive projects, other on-going developments and it was presented in the CAE Grand Challenge 2019 [47]. In this chapter, three cases of success where the methodology have been used are presented. The material cards obtained from this thesis methodology were used as fundamental inputs in the three cases.

The cases presented are a 3 Point Bending Test (3PBT), a dynamic bending and an axial crushing. For the 3PBT only the quasi-static material card is needed. For the dynamic bending and axial crushing the material card include the strain-rate definition. In all cases the material card is generated only from the experimental Tensile Tests.

8.1. 3 Point Bending Test (3PBT)

This project objective was to predict the behaviour of a cold-formed steel tube (as the ones shown in Figure 52) in a quasi-static 3PBT. For this, the card generated with this thesis methodology was used. In addition, another IDIADA methodology was implemented, in order to predict the change in properties at the corners due to the cold-forming process [55]. The influences of the manufacturing processes over the material properties are predicted also from the Quasi-Static Tensile Test and the simulation of the cold-forming process (no additional experimental data is required).

Figure 52 – Two AHSS steel cold-formed tubes. Source: Stalatube

Classically, the properties in the corner of a cold-formed tube can be roughly estimated by a theoretical approach which usually leads to a poor estimation of the Failure envelope. IDIADA

approach allows predicting more precisely the corner properties and thus, a more precise failure envelope for the affected zones, since the simulation of the manufacturing process is introduced.

In Figure 53, the results obtained in the 3PBT are shown. The 3PBT test is standardized by the ISO 12135:2016 norm [31]. The 3PBT are conducted by placing the component on two supporting pins in a distance which must be long enough to allow the formation of the whole plastic hinge due to bending behaviour. The central point of the specimen is pushed down, until material failure. During test, force and displacement of the force applicator are recorded.

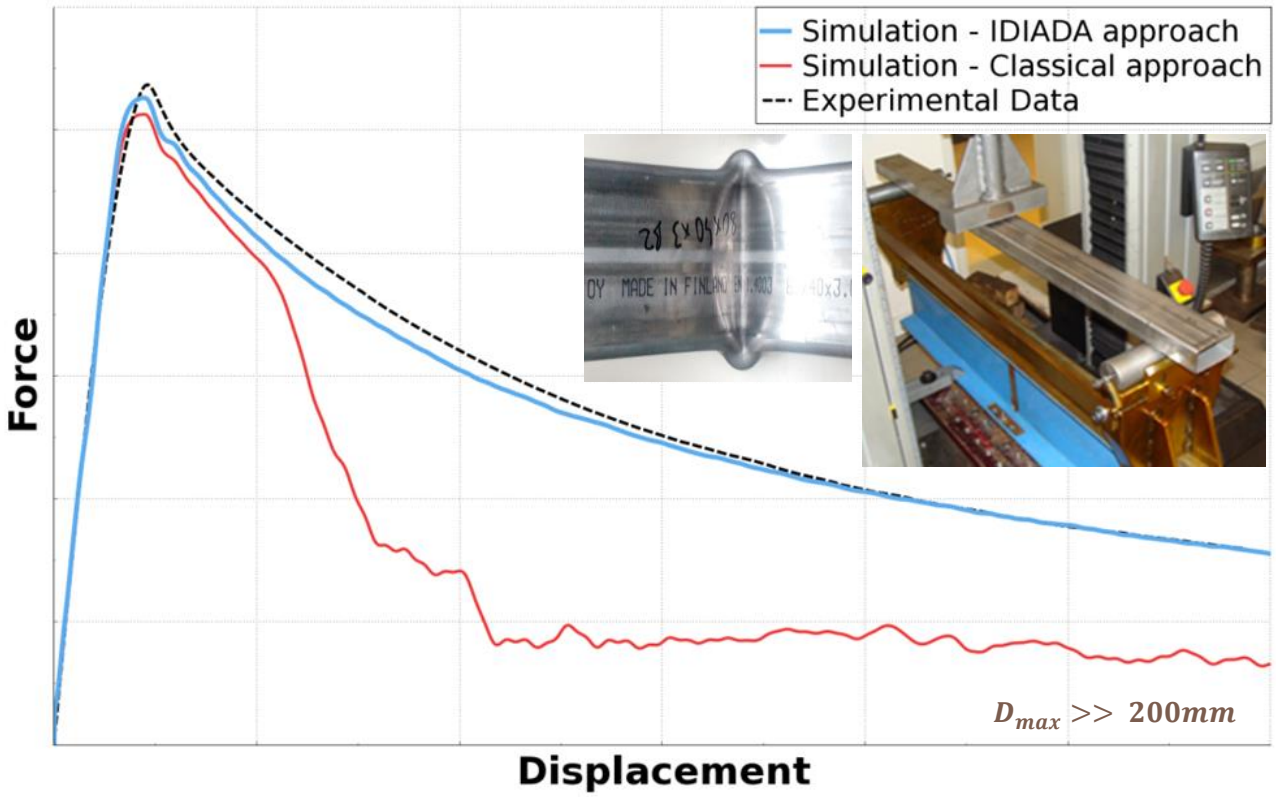

Figure 53 – 3PBT correlation by means of IDIADA approach. Source: IDIADA

In this case, the classical methodology was performed with a Von Mises definition, for the failure envelope. This kind of failure envelope is especially critical in this loading case, since in the folding of the material, damage is over predicted. As can be seen, the simulation by means of classical methods, show brittle-trending failure, and catastrophic failure.

By the application of the proposed tool, due to the Johnson-Cook based envelope, the catastrophic failure avoided. The level of prediction of the IDIADA approach is very precise compared with the classical approach, even for large displacements.

8.2. Dynamic bending

This project objective was to predict the behaviour of a dynamic bending test. For this, the card generated with this thesis methodology was used. In this case all the properties have been predicted only from the experimental Tensile Quasi-static and Strain-rate Tests. A new feature

compared with 3PBT presented in last chapter is implemented: a more precise modelling of the spot-weld and the heat affected zone (HAZ) behaviour.

The HAZ is a region near to the welds that shows poor toughness, because of the reheating caused during the welding process. There are some microstructure changes in the high heated, even for areas that are not melted. Figure 54 shows a schematic representation of the HAZ.

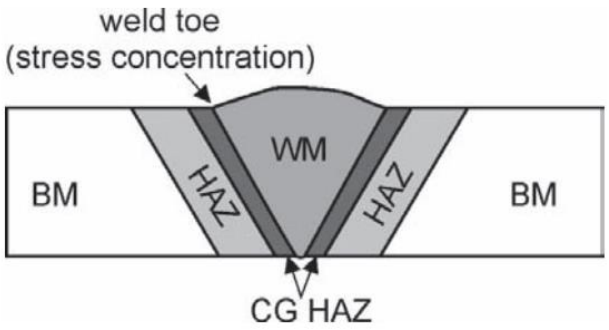

Figure 54 – Weld joint scheme with base material (BM), weld material (WM), heat affected zone (HAZ) and coarse grain affected zone (CG HAZ). Source: [67]

Many studies have shown the importance of the HAZ zone in fracture [24], [25], [37], [38]. Basically, the fracture typically occurs in the weld metal or in the HAZ rather than in the base material.

In Figure 55, the results obtained in the dynamic bending test are shown. The IDIADA approach predicts better the force level after the peak force. Both models include strain rate and HAZ definitions, changing between them only the steel-related material card.

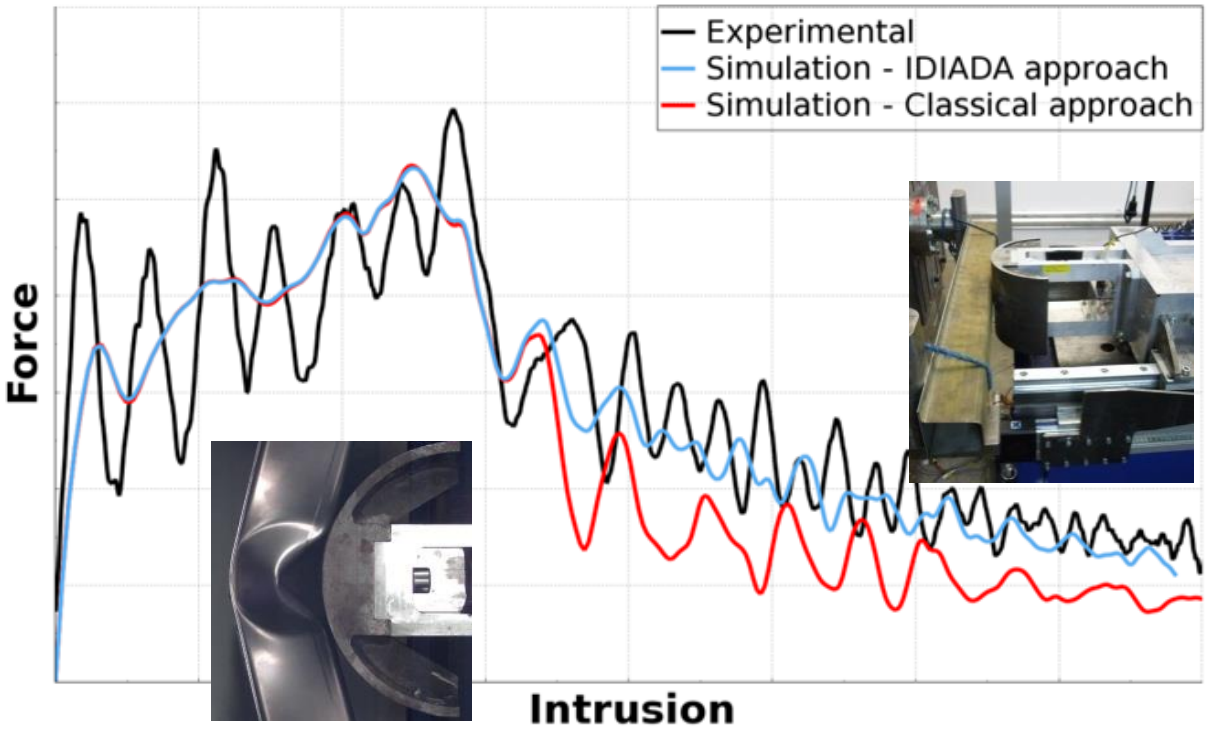

Figure 55 – Dynamic bending correlation by means of IDIADA approach. Source: IDIADA

8.3. Axial crushing

This task was part of the same project than the results used in last section. Models in this section, then, use the same material cards and modelling techniques as the dynamic bending above, in order to predict the axial crushing behaviour. This work was done as a validation of the IDIADA approach in their methodology for the spotweld and HAZ modelling.

In Figure 56Figure 55, the results obtained in the axial crushing simulations are shown. As occurred in the 3PBT test, damage by means of the classical definition was over predicted, leading to an underestimation of the load returned by the specimen after the first peak in the Force-displacement diagram. The IDIADA approach shows a better correlation for the force returned after the first peak compared to the classical approach.

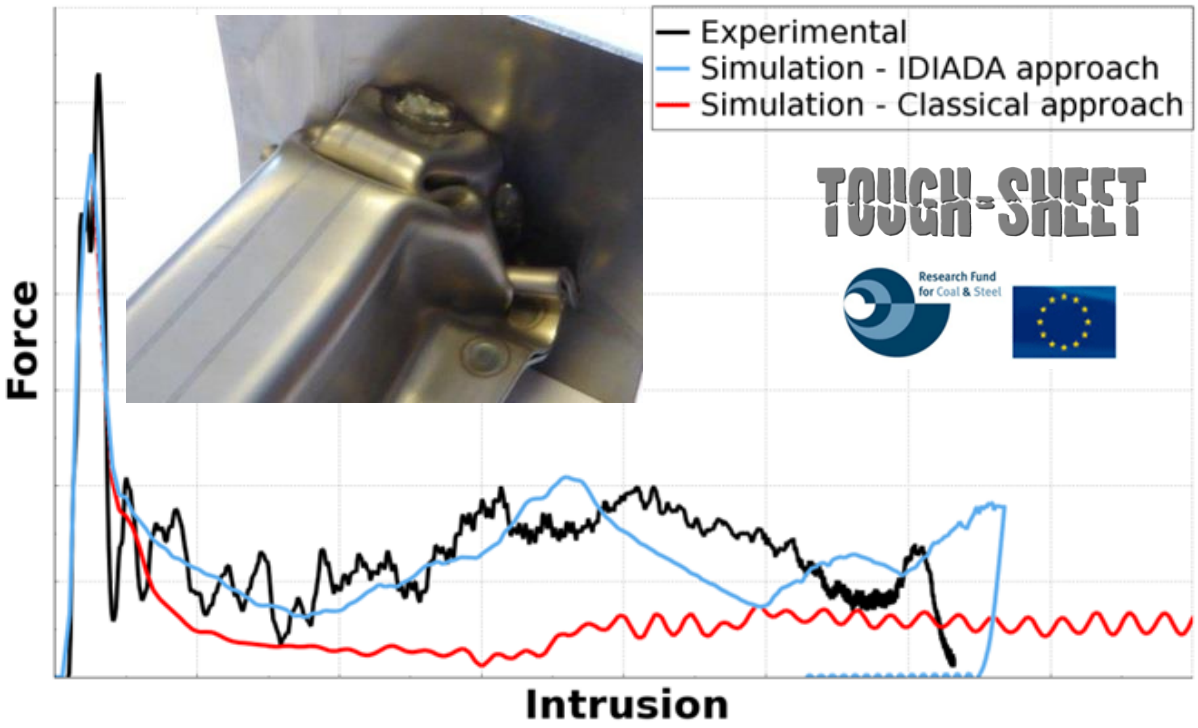

Figure 56 – Axial crushing correlation by means of IDIADA approach. Source: IDIADA

Currently, IDIADA is making further investigations on the spot-weld and HAZ modelling in order to improve the quality of the prediction of the post-peak behaviour in the last part of the axial folding when spot welds are involved.

9. Conclusions and further lines of work

In this chapter, the conclusions of the present thesis are exposed and future lines of work in order to improve the methodology created are proposed.

9.1. Conclusions

The growing use of AHSS steels in substitution of conventional steels is nowadays a constant in the development process for new vehicles and components, in order to enhance the passenger safety and reduce vehicle weight. On the other hand, the use of numerical methods in the design phases of a vehicle by means of passive safety and crash simulations makes possible to constantly evolve safety, performance and durability standards. In these sense, a proper modelling of the AHSS including damage definitions is fundamental to keep increasing the capabilities of the numerical methods in assist the CAE engineers to develop more efficient designs.

The principal objective of this work was the development of an automatized methodology that increases the correlation of the previous analytical approach applied in Applus+ IDIADA, to efficiently create material cards for the LSDYNA software. Generated material cards should include the consideration of damage onset and evolution, as strain-rate related effects. The data necessary for the generation of the material cards for AHSS materials is mean to be extracted from simple tensile test, in order to maintain low experimental costs. To make this possible, LSOPT software has been used as linking method between the different steps involved in the workflow of the proposed methodology.

After a brief introduction to steels, to AHSS grades and to the experimental campaign employed and an overview of the Finite Element Method, the elasto-plastic and damage constitutive models were introduced along with the characterizations approaches present in the industry. Then, the material model used in LSDYNA was presented and the two main models, developed in the methodology, for quasi-static and strain-rate consideration, were described and broken down, in order to point out the introduced automations and optimization techniques present in the methodology.

Finally, a comparison for the quasi-static calibration between the old and new methodologies including time and cost is done: great reduction on the time required for the generation of the material card is observed, especially in the hours related to manual work. In addition, higher level of correlation is obtained by the application of the new approach: the optimization procedures allow finding in a faster way more appropriate values than the manual-related methodology. At the end, some validations at component level are shown, were the present methodology was used to provide the material card required for performance design of components in productive projects

carried on by conventional designers in the Body Development department. Correlation levels were improved from the previously used manual generation of the material cards.

The methodology developed in this thesis has proven to reduce the time duration for the creation of steel (including AHSS) material cards for LSDYNA allowing the engineer being able to work in parallel with other tasks and also has improved the level of correlation of the generated material card. This way, IDIADA has increased the value of their product and it is obtained more efficiently, reducing costs.

Even a direct validation of the strain-rate methodology has not been done in this work, it has been performed indirectly in the application at component level of dynamic tests, with great levels of correlation. These new tool has developed an initial status for an autonomous steel material card generator, making possible a more efficient design for design-related tasks of conventional CAE engineers (i.e. not requiring a great knowledge or experience in the material mechanics framework).

9.2. Future lines of work

Although the current methodology allows characterizing AHSS steels with greater precision and in faster time than the previous methodology, there is still much room for improvement in the framework of improving simulations for AHSS related developments. There exist a series of lines of work to be followed in the future in order to enhance and enrich the methodology and make it more robust and faster:

- The effects of the point selection algorithm, the optimization algorithm, the curve matching technique and the meta-models used at LSOPT in order to avoid local minimum locking and to reduce the number of iterations needed, decreasing the duration time.

- Higher automation can be achieved by using more powerful scripting languages as Python to change directly the lsopt files itself, for example, rewriting the range of the variables and the initial value of the optimization depending of the type of steel. Also the range for the FADEXP and Regulation Factor could be changed while the program is running adapting the range value in consonance with the already optimal values calculated for previous meshes.

- At the moment the failure envelope curve introduced in the GISSMO model is obtained empirically from different AHSS steels from IDIADA database as an average Johnson-Cook curve and normalized for the plastic strain. The failure locus could be calibrated by means of extra experiments as shear and notch specimens in order to predict accurately the failure for all the different load cases.

- Direct validation of the strain-rate material card generated by simulation of the strain-rate tests in order to check the behaviour is as expected.

- Inclusion of a procedure for material characterization from Nakajima / Marciniak test for very detailed material card with failure integrated when the client desires higher prediction of crack propagation.

- Expanding the methodology to fully integrated element formulation.

References

[1] **Anderson, T.**, (2005). *Fracture mechanics: fundamentals and applications*. CRC Press.

[2] **Argon, A., Im, J., Safoglu, R.**, (1975). *Cavity formation from inclusions in ductile fracture*. Metallurgical Transactions A, 6(4):825-837.

[3] **Askeland, D., Fulay, P., Wright, W.**, (2010). *The science and engineering of materials. 6th edition*. CL Engineering.

[4] **ASTM E8 / E8M-16a**, (2016). *Standard Test Methods for Testing of Metallic Materials.* ASTM International, West Conshohocken, PA. Web: www.astm.org.

[5] **Atanackovic, T., Guran, A.**, (2000). *Theory of Elasticity for Scientists and Engineers*. Birkhäuser.

[6] **Bai, Y., Teng, X., Wierzbicki, T.**, (2009). *On the application of stress triaxiality formula for plane strain fracture testing*. Journal of Engineering Materials and Technology, 131(2):021002.

[7] **Baluch, N., Udin, Z., Abdullah, C.**, (2014). *Advanced High Strength Steel in Auto Industry: An Overview.* Engineering, Technology & Applied Science Research, 4(4):686-689

[8] **Bao, Y.**, (2003). *Prediction of ductile track formation in uncracked bodies*. Ph.D. thesis, Massachusetts Institute of Technology.

[9] **Bao, Y., Wierzbicki, T.**, (2004). *On fracture locus in the equivalent strain and stress triaxiality space*. International Journal of Mechanical Sciences, 46(1):81-98.

[10] **Barbu, L., Martinez, X., Oller, S., Barbat, A.**, (2015). *Validation on large scale tests of a new hardening–softening law for the Barcelona plastic damage model*. International journal of fatigue 81:213-226.

[11] **Barbu, L., Martínez, J., Oller, S., Barbat, A.**, (2015). *Large scale validation of a new isotropic hardening law for the barcelona plastic damage model under ultra low cycle fatigue conditions*. COMPLAS XIII: proceedings of the XIII International Conference on Computational Plasticity: fundamentals and applications, 248-259.

[12] **BETA CAE Systems SA.**, (2015). *ANSA User's guide*.

[13] **BETA CAE Systems SA.**, (2015). *META User's guide*.

[14] **Bower, A.**, (2009). *Applied Mechanics of Solids. 1st edition*. CRC Press.

[15] **Bridgman, P.** (1952). *Studies in large plastic flow and fracture: With special emphasis on the effects of hydrostatic pressure*. Harvard University Press.

[16] **Callister, W.**, (2007). *Materials Science and Engineering: An introduction. 7th ed.* John Wiley & Sons, Inc. Wiley, New York.

[17] **Choung, J., Cho, S.**, (2008). *Study on true stress correction from tensile tests*. Journal of Mechanical Science and Technology, 22(6):1039-1051.

[18] **Chiumenti, M., Cervera, M.**, (2018). *Continuum damage model*. Slides from "Numerical models for the civil and structural engineering" of the Master degree of Civil engineering at the Universitat Politècnica de Catalunya (UPC). Spain.

[19] **Chiumenti, M., Cervera, M.**, (2018). *Elasto-Plasticity*. Slides from "Numerical models for the civil and structural engineering" of the Master degree of Civil engineering at the Universitat Politècnica de Catalunya (UPC). Spain.

[20] **Clear Science**, (2010). *Steel: An iron-carbide alloy*. Retrieved 08/2019 from http://clearscience.tumblr.com/post/628686089/steel-is-not-an-element-rather-it-is-the.

[21] **Cottrell, A.**, (1959). *Theoretical aspects of fracture*. International Conference on Fracture (ICF0), Swampscott-MA (USA).

[22] **Effelsberg, J., Haufe, A., Feucht, M., Neukamm, F., DuBois, P.**, (2012). *On parameter identification for the gissmo damage model*. In 12th International LS-DYNA Users Conference, Dearborn, MI, USA.

[23] **Elliotis, M.**, (2013). *A Finite Element Approach for the Elastic-Plastic Behavior of a Steel Pipe Used to Transport Natural Gas*. Conference Papers in Energy, vol. 2013, Article ID 267095.

[24] **Gaudet, M., Poole, W.**, (2012). *Tensile and Fracture Properties of X80 Steel Microstructures Relevant to the HAZ*. Proceedings of the 2012 9th International Pipeline Conference. Volume 3: Materials and Joining: 491-499.

[25] **Guzman, J., Martinez-Gonzalez, C., Baltazar, V., Basak, S., Panda, S., Razmpoosh, M., Gerlich, A. and Zhou, Y.**, (2018). *Influence of SC-HAZ microstructure on the mechanical behavior of Si-TRIP steel welds*. Materials Science and Engineering: A, 718:216-217.

[26] **Hancock, J., Mackenzie, A.**, (1976). *On the mechanisms of ductile failure in high-strength steels subjected to multiaxial stress-states*. Journal of the Mechanics and Physics of Solids, 24(2-3):147-160.

[27] **Haufe, A., DuBois, P., Neukamm, F., Feucht, M.**, (2011). *Gissmo-material modeling with a sophisticated failure criteria*. LS-Dyna Developer Forum 2011, Stuttgart.

[28] **Hencky, H.**, (1924). *Zur Theorie plastischer Deformationen und der hierdurch im Material hervorgerufenen Nachspannngen* (in german). Z. Angew. Math. Mech. 4:323–334.

[29] **Henry, B., Luxmoore, A.**, (1997). *The stress triaxiality constraint and the Q-value as a ductile fracture parameter*. Engineering Fracture Mechanics, 57(4):375-390.

[30] **Instron Corportation**, (2016). *Reference Manual – Equipment: Instron Series 5500 Load Frames Including series 5540, 5560, 5580*.

[31] **ISO 15135:2016**, (2016). *Metallic materials – Unified method of test for the determination of quasi-static fracture toughness*.

[32] **ISO 6892-1:2016**, (2016). *Metallic materials - Tensile testing - Part 1: Method of test at room temperature*.

[33] **Johnson, G., Cook, W.**, (1983). *A constitutive model and data for metals subjected to large strains, high strain rates, and high temperatures*. Proceedings of the 7th International Symposium on Ballistics, 541-547.

[34] **Johnson, G., Cook, W.**, (1985). *Fracture characteristics of three metals subjected to various strains, strain rates, temperatures and pressures*. Engineering Fracture Mechanics, 21(1):31-48.

[35] **Kachanov, L.**, (1958). *On time to rupture in creep conditions* (in russian). Izviestia Akademii Nauk SSSR, Otdelenie Tekhnicheskikh Nauk, 8:26-31

[36] **Khaira, H.**, (2013). *Time-temperature-transformation diagram*. Professor slides. Manit, Bhopal.

[37] **Kim, J., Oh, Y., Hwang, I., Kim, D., Kim, J.**, (2001). *Fracture behavior of heat-affected zone in low alloy steels*. Journal of Nuclear Materials, 299(2):132-139.

[38] **Kumar, A., Kumar, S. and Kumar, R.**, (2015). *Some studies on Heat-Affected Zone (HAZ) Toughness behavior of API 5L X52 steel*. Indian Welding Journal, 48(2):68-75.

[39] **La Rosa, G., Mirone, G., Risitano, A.**, (2001). *Effect of stress triaxiality corrected plastic flow on ductile damage evolution in the framework of continuum damage mechanics*. Engineering Fracture Mechanics, 68(4):417-434.

[40] **Laboratori de Càlcul Numèric (LaCàN)**, (2018). *Discretization Methods; FEM*. Slides from "Computational engineering for design and operation" of the Master degree of Civil engineering at the Universitat Politecnica de Catalunya (UPC). Spain.

[41] **Le Roy, G., Embury, J., Edwards, G., Ashby, M.**, (1981). *A model of ductile fracture based on the nucleation and growth of voids*. Acta Metallurgica, 29(8):1509-1522.

[42] **Lemaitre J., Chaboche J.**, (1978). *Aspect phénoménologique de la rupture par endommagement.* Journal de Mécanique appliquée, 2:317-365.

[43] **Lemaitre, J., Chaboche, J.**, (1994). *Mechanics of solid materials*. Cambridge University Press.

[44] **Livermore Software Technology Corporation**, (2015). *LS-OPT® Uuser's Manual. A design optimization and probabilistic analysis tool for the engineering analyst*. Livermore, California.

[45] **Livermore Software Technology Corporation (LSTC)**, (2018). *LS-DYNA® Keyword User's Manual Volume I, II and III*, Version R10.0.

[46] **McClintock, F.**, (1968*). A Criterion of Ductile Fracture by the Growth of Holes*, J. Appl. Mech., 35:362–371.

[47] **Martin-Santos, E. and Dominguez, A.**, (2019). *Reducing testing activities for High-Strength Steel Material Characterization devoted to Crash related design*. Presentation in Material: Material and failure models for metals at the CAE Grand Challenge 2019, Hanau.

[48] **Martinez, X., Oller, S., Barbu, L., Barbat, A., De Jesus, A.**, (2015). *Analysis of Ultra Low Cycle Fatigue problems with the Barcelona plastic damage model and a new isotropic hardening law*. International Journal of Fatigue 73:132-142.

[49] **Neto, E., Peric, D., Owen, D.**, (2008) *Computational Methods for Plasticity: Theory and Applications*. Chapter 3. John Wiley & Sons.

[50] **Neukamm, F., Feucht, M., Haufe, A.**, (2009). *Considering damage history in crashworthiness simulations*. 7th European LS-DYNA Conference. Salzburg, Austria.

[51] **Nguyen, P., Lee, J., Yim, H., Lee, S., Heo, S.**, (2015). *Analysis of vehicle structural performance during small-overlap frontal impact*. International Journal of Automotive Technology, 16(16):799-805.

[52] **Oden, J., Reddy, J.**, (1983). *Variational Methods in Theoretical Mechanics, 2nd ed.* Springer-Verlag, New York.

[53] **Paul, S., Roy, S., Sivaprasad, S., Bar, H., Tarafder, S.**, (2018). *Identification of Post-necking Tensile Stress–Strain Behavior of Steel Sheet: An Experimental Investigation Using Digital Image Correlation Technique*. Journal of Materials Engineering and Performance, 27: 5736.

[54] **Pollack, H.**, (1988). *Materials Science and Metallurgy*, *4th ed*. Prentice-Hall.

[55] **Ramos, P.**, (2018). *Estudio del comportamiento plástico hasta rotura de aceros de alta Resistencia mediante el desarrollo de modelos detallados de elementos finitos*. Bachelor thesis at the Universitat Politècnica de Catalunya (UPC), Barcelona, Spain.

[56] **Reddy, J. N.** (2005). *An Introduction to the Finite Element Method. 3th ed.* McGraw-Hill International Enterprise LLC, UK Branch.

[57] **Rice, J., Tracey, D.**, (1969). *On the ductile enlargement of voids in triaxial stress fields.* Journal of the Mechanics and Physics of Solids, 17(3):201-217.

[58] **Sandberg, H., Rydholm, O.**, (2016). *Evaluation of Material Models to Predict Material Failure in LS-DYNA*. Master thesis at the Lund University, Lund, Sweden.

[59] **Salas, A.**, (2017). *Damage and modelling of composite materials for the automotive industry*. Master thesis at the Universitat Politècnica de Catalunya, Barcelona, Spain.

[60] **Shaw, J., Zuidema, B.**, (2001). *New High Strength Steels Help Automakers Reach Future Goals for Safety, Affordability, Fuel Efficiency and Environmental Responsibility*. SAE Paper 2001-01-3041.

[61] **Steel Market Development Institute Automotive Market Program**. Visited 06/2019: www.autosteel.org.

[62] **Sun, J., Deng, Z., & Tu, M.**, (1991). *Effect of stress triaxiality levels in crack tip regions on the characteristics of void growth and fracture criteria*. Engineering Fracture Mechanics, 39(6):1051-1060.

[63] **Taylor, G.** (1934). *The mechanism of plastic deformation of crystals. Part I.—Theoretical*. Proceedings of the Royal Society A, 145(855).

[64] **Tamarelli C. M.,** (2011). *AHSS 101 The evolving use of advanced high-strength steels for automotive applications*. Steel Market Development Institute. Southfield, Michigan. Web: www.autosteel.org

[65] **Thomason, P.**, (1998). *A view of ductile-fracture modelling*. Fatigue & Fracture of Engineering Materials & Structures, 21(9):1105-1122.

[66] **von Mises, R.** (1913). *Mechanik der festen Körper im plastisch-deformablen Zustand* (in german). Nachrichten von der Gesellschaft der Wissenschaften zu Göttingen. Mathematisch-Physikalische Klasse. 1913(1):582–592.

[67] **Vuherer, T., Maruschak, P. and Samardžić, I.**, (2012). *Behaviour of Coarse Grain Heat Affected Zone (HAZ) during Cycle Loading*. Journal Metalurgija, 51:301-304.

[68] **Wang, K.**, (2016). *Calibration of the Johnson-cook failure parameters as the chip separation criterion in the modelling of the orthogonal metal cutting process*. Master thesis at the McMaster University, Hamilton, Ontario.

[69] **Wierzbicki, T., Werner, H.**, (1998). Cockroft and Latham Revisited - Impact and Crashworthiness Laboratory. Report(16), MIT.

[70] **Witowski, K., Feucht, M., Stander, N.**, (2011). *An effective curve matching metric for parameter identification using partial mapping*. 8th European LS-DYNA Users Conference, Strasbourg, pp. 1–12.

[71] **WorldAutoSteels**, *Evolving AHSS Types*. Retrieved 06/2019 from: http://www.worldautosteel.org/steel-basics/steel-types/evolving-ahss-types/

[72] **Xue, L.**, (2007). *Damage accumulation and fracture initiation in uncracked ductile solids subject to triaxial loading*. International Journal of Solids and Structures, 44(16):5163–5181.